CITY UNIVERSITY
LONDON

Optimization of Silicon Photonic Devices for Polarization Diversity Applications

Sasan Soudi

A thesis submitted to the City University in fulfilment of the requirement for the Degree of Doctor of Philosophy

City University London

Photonic Research Group
School of Mathematics, Computer Science and Engineering
Northampton Square, London EC1V 0HB, UK

January 2016

To My Father & Mother,

With Love

List of Figures

Acknowledgments

In the name of God, the Most Gracious and the Most Merciful

First and foremost, I would like to acknowledge sincerely and gratitude to his supervisor: Professor B. M. Azizur Rahman, for his advice and guidance throughout this research work. He has been very helpful and so kind as to provide valuable discussions, at any time and on every matter.

I would like to express my deepest gratitude and sincere appreciation to Dr. Yadollah Rajaei chancellor of Zanjan Islamic Azad University (IAU) for his generous help and continuous support before and during the education.

The author is also pleased to acknowledge to all the secretarial staff in the School of Engineering and Mathematics.

I would like to thank Ms. Chatelain, Postgraduate Research Courses Officer of the school who has been kind enough to advise and help in her respective roles.

The author is also pleased to acknowledge the support from the Islamic Azad University (IAU) for this research work.

My special thanks goes to my colleagues who created a pleasant and unforgettable atmosphere in the laboratory during the years of working with the Photonics Modelling Research Group, City University London.

In particular, I am grateful to Dr. Bamdad Partovi and Dr. Tahmasebian, Mr. Tavasol. P and Dr. P. Afshar, for their invaluable assistance during my staying in the U.K.

Finally, I am forever indebted to my father, mother, brother, and sister for their love, endless patience and encouragement without whom I would never have got this far.

Declaration

I grant powers of discretion to the University Librarian to allow this thesis to be copied in whole or in part without further reference to the author. This permission covers only single copies made for study purpose, subject to normal conditions of acknowledgments.

Abstract:

This thesis discusses two important designs, analysis and optimization of polarization-based devices such as polarization rotator and splitter. Many optical sub-systems integrate with guided wave photonic devices with two-dimensional confinement and high contrast between the core and cladding. The modes present in such waveguides are not purely of the TE or TM type. They are hybrid in nature, where all six components of the magnetic and electric fields are present. This causes the system fully to be polarization dependent. Currently, the polarization issue is a major topic to be dealt with during the design of high efficiency optoelectronic subsystems for further enhancement of their performances. To characterize the device polarization properties a vectrorial approach is needed. In this work, the numerical analysis has been carried out by using the powerful and versatile full vectorial **H**-field based finite element method (FEM). This method has been proved to be one of the most accurate numerical methods to date for calculating the modal hybridness, birefringence and consequently to calculate the device length, which is an important parameter when designing devices concerning the polarization issues. Polarization devices may be fabricated by combining several butt-coupled uniform waveguide sections. The Least Squares Boundary Residual (LSBR) method is used to obtain transmission and reflection coefficients of all the polarized modes by considering both the guided and the radiated modes. On the other hand, finite element method cannot calculate the power transfer efficiency directly, hence the LSBR method is used along with the FEM for this purpose. The LSBR method is rigorously convergent, satisfying the boundary conditions in the least square sense over the discontinuity interface. Using this method, the power transfer from the input to the coupler section and at the output ports can be evaluated. When designing polarization rotators, it is necessary to calculate the modal hybridness of a mode. In this research, it is identified that when the symmetric waveguides are broken, the modal hybridity is enhanced, and thereby a high polarization conversion is expected. This work is devoted to the study of design optimization of a compact silicon nanowire polarization device. An interesting and useful comparison is made on their operating properties such as the crosstalk, device length, polarization dependence, and fabrication tolerances of the polarization in directional coupler based devices. In this study initially the **H**-field modal field profile for a high index contrast silicon nanowire waveguide is shown. The effects of waveguide's width on the effective indices, hybridness, power confinement in the core, and the cladding have been investigated. The modal birefringence of such silicon nanowire waveguides also is shown. It is presented here that for a silicon nanowire waveguide with height of 220 nm, fundamental and second modes exist in the region of the width being 150 – 300 nm, and 500 – 600 nm, respectively. A compact 52.8 μm long passive polarization rotator (PR) using simple silicon nanowire waveguides is designed with a power transfer of 99 % from input TE to output TM power mode, with cross-talk better than – 20 dB and loss value lower than 0.1 dB. Furthermore, an extensive study of fabrication tolerances of a compact (PR) is undertaken. The design of an ultra-compact polarization splitter (PS) based on silicon-on-insulator (SOI) platform is presented. It is shown here that a low loss, 17.90 μm long compact PS, and wide bandwidth over the entire C-band can be achieved.

Symbols and abbreviations:

PIC	Photonic Integrated Circuit
MMI	Multimode Interference Coupler
LS-PICs	Large-Scale Photonic Integrated Circuits
CMOS	Complementary metal-oxide-semiconductor
AWG	Arrayed Waveguide Gratings
PRs	Polarization Rotators
PBSs	Polarization Beam Splitters
SOI	Silicon-On-Insulator
SRA	Stimulated Raman Scattering
SPM	Self-Phase modulation
SBS	Simulated Brillouin Scattering
TPA	Two Photon Absorption
XPM	Crossphase Modulation
FWM	Four-Wave-Mixing
TE	Transverse Electric
TM	Transverse Magnetic
PLCs	Planar Light-wave Circuits
PMD	Polarization Mode Dispersion
PDL	Polarization Dependent Loss
PDλ	Polarization Dependent Wavelength
RIE	Reactive Ion Etching
EB	E-beam Lithography
SSC	Spot Size Converters
$LiNbO_3$	Lithium Niobate
SiO_2	Silica
Si	Silicon
InP	Indium Phosphide
GaAs	Gallium Arsenide
InGaAsP	Indium Gallium Arsenide Phosphide
LSBR	Least Square Boundary Residual
BPM	Beam Propagation Method
FEM	Finite Element Method
PML	Perfectly Matched Layer
TBC	Transparent Boundary Condition
FDTD	Finite Difference Time Domain

VFEM	Vectorial H-Field Finite Element Metho
n_{eff}	Effective index
A_{eff}	Effective area
Γ_{Si}	Power confinement in silicon
Γ_{SiO2}	Power confinement in silica
L_{π}	Half-beat length
λ	Wavelength
β	Propagation constant
ε	Permittivity
μ	Permeability
μ_r	Relative Permeability
k	Wavenumber
ω	Angular frequency
c	Velocity of light in vacuum
OEIC	Optical Electronics Integrated Circuit
WRM	Weighted Residual Method
MMM	Mode Matching Method
PMM	Point Matching Method
BEM	Boundary Element Method

Introduction:

1.0 Telecommunications:

It has been a while since human beings are able to transmit information by the application of light. Fire and smoke signals were used by Greeks in 800 BC to send information. This technique was used in situations such as victory in a war, alerting against the enemy, call for help, etc. Needless to say, mostly only one type of signal was conveyed. During the second century B.C. signalling lamps were used to encode optical signals. As a result, they were able to send any message they wanted. No development in optical communication was achieved till the end of the 18th century. The following factors limited the speed of the optical communication link: the human eye as the receiver, the requirement of line of sight transmission paths, and unreliable nature of transmission paths which is influenced by atmospheric effects. It should be mentioned that fog and rain are regarded as the above said effects. Semaphore was developed by Chappe in 1791 to telecommunicate on land which was also with limited information transfer.

Telegraph was invented by Samuel Morse the end a new era called electrical communications was started all over the world. The application of wire cables for transmitting Morse coded [1] signal was implemented in 1844. It was in 1872 when the photo phone was proposed by Alexander Graham Bell with a diaphragm giving speech transmission over a distance of 200 m. But in a matter of four years, he changed the photo phone into telephone which used electrical current for speech signals transmission.

It was in1878 when the first telephone exchange was installed at New Haven. Meanwhile, radio waves were discovered by Hertz in 1887. Radio communication with no wires was presented by Marconi in 1895. Radio waves and microwaves used as the carrier transmitted the signals over a long distance using modulation techniques. During the middle of the twentieth century, it was understood that if optical waves were used as the carrier, an increase of several orders of magnitude of bit rate distance product would be possible [1]. According to Shannon-Hartley theorem invented in 1948, channel bandwidth, signal power and the noise can limit the transmission capacity.

In the old optical communication system, there was an enormous transmission loss (10^5 to 10^7 dB/km). As a result, the bit rate distance product is only about 1 (bit/s)-km. Meanwhile, the information carrying capacity of telegraphy is about hundred times smaller than a telephony. Even though the high-speed coaxial systems were evaluated during 1975, they had smaller repeater spacing. It should be mentioned that microwaves are used in modern communication systems with the increased bit rate distance product. However, laser regarded as one of the coherent optical carriers will have more information carrying capacity.

Consequently, the communication engineers were into optical communication that uses lasers in an effective manner from 1960 onwards. Laser was invented by Maiman in 1960 and

a new era in optical communication was started. Compared to radio waves and microwaves, the light waves coming from the laser, a coherent source of light waves with high directionality, high intensity and high monochromaticity with less divergence, are used as carrier waves which are capable of carrying large amount of information. CO_2 laser was fabricated and designed and by an Indian electrical engineer, H. M Patel, and also demonstration of semiconductor LASER in the early 60's by Maiman paved the way to develop a transmission medium capable for transmitting and processing large bandwidth of signals reliably.

1.1 Fibre Optic

Initially metallic and non-metallic waveguides were fabricated in order to guide light in a waveguide. They were not suitable for telecommunication since they had enormous losses. Tyndall discovered that the phenomenon of total internal reflection can transmit light through optical fibres. During 1950s, the optical fibres were used in endoscopes to see the inner parts of the human body. It should be added that such fibres had large diameters of about 1 or 2 millimetre and could provide a much more reliable and versatile optical channel than the atmosphere.

In 1966, a paper was published by Kao and Hockham which was about the optical fibres communication system [2]. However, the fibres of that time suffer from an enormous loss of 1000 dB/km which was larger than a few dB/km losses in the atmosphere. Immediately Kao and his fellow workers figured out that the impurities existed in the fibre material were the causes of such high losses.

It was in 1970 when Kapron, Keck and Maurer could reduce the losses to 20 dB/km by the development of a pure silica fibre. At this attenuation loss, repeater spacing for optical fibres links become comparable to those of copper cable systems and as a result, the optical fibre communication system became an engineering reality.

Earlier multimode fibres were used to transmit light with sources operating at wavelength near 800 nm. In these systems, the fibre employed has attenuation of 3dB/km and much better than the coaxial cable which has attenuation of 10-20 dB/Km. The fibres employed in the optical purpose suffers chromatic and modal dispersion.

Maurer's team made further development on the fibre. With the single mode fibre, it would eliminate the modal dispersion. Single mode fibres operated at 1310 nm wavelength are designed to carry higher capacity for the long distances with low intrinsic loss and zero modal dispersion.

A laser operating at the 1550 nm band was developed afterwards and when signals were transmitted down the fibre, it was found that the attenuation of the fibre was at its minimum. However such 1550 nm laser was less effective than the 1330 nm laser for reducing dispersions in fibre. Nevertheless, with these developments and other advancement, liked dispersion compensating techniques and development in hardware, liked integrated circuit

(IC) or optical electronics integrated circuits (OEIC), fibre optics telecommunications were now widely deployed.

1.2 Photonic integrated circuit (PIC) – Deeply etched Waveguides:

A broad class of electronic functionalities can be synthesised from a small set of elementary components and it is the power of micro-electronic integration technology. Transistors, resistors and capacitors are the examples of the above said elementary components. A technology supporting the integration of these elementary components can be used for a broad class of applications. Furthermore, a large market can pay back the investments made in its development. In spite of the fact that photonic integration has lots in common with micro-electronic integration, a major difference is the variety of devices and device – principles in photonics. We do have couplers, multiplexers, filters, lasers, detectors, switches, modulators, to mentions just a few devices, and a wide range of different operations and principles and materials has been reported for each of these devices. Developing a monolithic technology capable of realising even a modest subset of all such devices is impossible. As a result, reduction of the board variety is the key for the success of integration in photonics.

A strong transverse confinement of light can be caused by deep etching process. Deep etched waveguides can be narrower and, most importantly, they have much lower bending loss compared to shallow etched waveguides. Because of the very small radius (< 10 μm), they can be used for low-loss interconnection. It allows for a strong reduction of the size of interconnection circuits. In addition, deep etched MMI-couplers and deep etched AWG's, which are considered as the key components in Photonic Integrated Circuits (PIC), can be made much smaller than shallow etched ones. It seems that deep etching is the key to reduce the device dimensions.

1.3 Large-Scale Photonic Integrated Circuits on Silicon:

Large-scale photonic integrated circuits (LS-PICs) are very promising for many applications [3], [4] such as wavelength division multiplexed systems, optical interconnects, next-generation optical networks, coherent transceivers, lab-on-chip, etc. Because LS-PIC provide different advantages, including higher performance, lower component-to-component coupling losses, reduced device footprint, lower package costs and lower power consumption.

However, some factors make the progress on LS-PICs limited; one of which is that the material system for photonics is much more complex than electronics. Currently, the focus is on silicon and InP substrate technologies [5] which is a good platform for LS-PICs since it enables both passive and active components in the same substrate [6].

Silicon-based PICs [7], [8], [9], [10], [11], [12], [13], [14] have also become very popular, because of the following reasons: their compatibility with mature CMOS (complementary metal–oxide–semiconductor) technologies with excellent processing control, low cost and high volume processing. In addition, silicon-on-insulator (SOI) nanowires enable ultra-sharp bends (e.g., 1-2 μm) which is because of their ultra-high refractive index contrast [13]. As a consequence, various ultrasmall SOI nanowire-based devices such as arrayed-waveguide

gratings (AWG) [8], [9], [10] and Microrings [12] can be realized. However, as silicon is not a direct band gap semiconductor material, because it is not a good option for active PICs with lasers, as well as photodetectors. Fortunately, some technologies are available to solve the issue. As an example, the hybrid III–V/Si platform provides a very promising solution for realizing integrated active photonic devices on silicon [4], [14]. As a result, it is feasible to realize LS-PICs on a silicon substrate. However, we should remember that there are still several essential issues when regarding the realization of silicon LS-PICs.

It is well known that SOI nanowire PICs are usually severely polarization-sensitive, because of the huge structural birefringence [9]. Although it is often possible to use specific approaches and diminish the polarization dependence for some components [15], a general solution for the polarization issue is the application of a polarization diversity system consisting of polarization beam splitters (PBSs) and polarization rotators (PRs) [7], [11]. Polarization diversity is also very important for many other applications, including coherent receivers, as well as polarization multiplexing technologies [16] for polarization-multiplexed transmission systems. In the section on 'Polarization handling', a review will be presented for our work on polarization handling, such as PBSs and PRs.

1.4 Silicon-On-Insulator (SOI) waveguides:

A Silicon wire waveguide based on the silicon-on-insulator (SOI) structure is regarded as a promising platform for highly integrated, ultrasmall optical circuits or microphotonics devices required for future optical network systems [17], [18], [19]. Si/SiO_2 waveguides achieve strong light confinement as a result of the large refractive-index difference between Si and SiO_2 ($\Delta n = 2$). The large difference makes possible core sizes of less than a micrometer providing a single-mode propagation at a wavelength of 1.5 μm. Furthermore, its strong confinement allows sharp bends with radii of just a couple of micrometers. As a result, Si wire waveguides should enable us to make optical circuits which are significantly smaller and have a higher integration density than would be otherwise possible. Also it is possible to integrate Si wire waveguides with Si electronic circuits because both can be made on an SOI substrate leading to the new functional optical devices controlled electronically.

Another feature of Si wire waveguides is their high power density which is because of the strong confinement. Even a 50-mW laser diode can yield a power density of 100 MW / cm^3. Si wires might become a platform for nonlinear optical devices. In addition, the matured fabrication technologies and high-quality substrates for Si microelectronic devices can be used in order to make Si wire systems which are great advantage in the development of the Si wire waveguide system.

Several components based on Si wire waveguides have already been demonstrated such as ring resonators, rotators, splitters, and arrayed waveguide gratings [20], [21] and [9]. However, there are a number of big problems in the practical use of Si wire waveguides. When they are connected to an optical fibre, the coupling loss is quite large which is due to the fact that the mode field sizes are very different.

In addition, because of the high refractive-index contrast, the scattering loss at the sidewalls can govern the propagation loss. One approach to reduce such losses is the application of a spot-size converter to efficiently couple the waveguide to a fibre and to improve the fabrication process for optical waveguides in which the sidewalls have to be extremely smooth. Recently, different types of spot-size converters that can reduce the coupling loss have been proposed [22]. The propagation loss can be reduced to a great extent by improving the fabrication process [23]. The reduced losses mean that it has become possible to use Si wire waveguides in the practical optical devices.

The core size of a Si wire WGs is less than a micrometer for single mode propagation and because of this small core, the power density of a Si wire is higher by a factor of about 1000 than that of conventional single-mode fibre. As a consequence, it is expected that nonlinear optical effects will occur when using a low input power equivalent to that in optical communications. A wide range of nonlinear phenomena [24] can be produced by light propagation with such a high power density, including stimulated Raman scattering (SRS), self-phase modulation (SPM), stimulated Brillouin scattering (SBS), two-photon absorption (TPA), cross-phase modulation (XPM) and four-wave mixing (FWM). During the past few years, all-Si active optical devices have been extensively studied in connection with the above said nonlinear effects. A variety of different applications such as amplifier, laser [25], modulator [26] and wavelength converter [28] have been investigated.

1.4.1 Waveguide Modal Analysis:

The Maxwell equations are able to govern light propagation in waveguides. The optical modes of the waveguide are the Eigen solutions to the Maxwell equations, subject to the appropriate boundary conditions which are imposed by the waveguide geometry.

In the slab waveguide system, two orthogonally polarized modes can be supported: the transverse electric (TE) mode defined as electric field perpendicular to the propagation direction and lying in the plane of the core layer, and the transverse magnetic (TM) mode referring to the field distribution with the magnetic field perpendicular to the propagation direction and in the plane of the core layer (i.e., the electric field is normal to the core layer). It should be notified that in a waveguide, light is confined two-dimensionally in both the x- and y-directions and is guided along the propagation z-direction.

The requirement for the field components defined for the slab waveguides, either $E_y = E_z = H_x = 0$ for TE or $H_z = H_y = 0$, $H = H_x$ for TM, is not valid any more since the propagation light must satisfy the boundary conditions which are imposed by the waveguide in both the Y- and X-directions. The existence of pure TE and TM modes is only possible in planar slab waveguide with 1-dimensional confinement. However, when practical optical waveguide is with 2-dimensional confinement, the modes are classified as quasi-TE and quasi-TM modes containing all the six components of the ***E*** and ***H*** fields. Furthermore, in the high index contrast silicon nanowires, the modal hybridness is much higher. In order to find all the 3 components of the **H**-field and the evolution of fully hybrid quasi-TE and quasi-TM modes along a guides-wave device all the methods used must be fully vectorial in nature.

These modes can be denoted as H^{y}_{pq} and H^{x}_{pq}, respectively, where p and q are the number of the extremal field (maximum and minimum) in the x- and y-direction. For H^{y}_{pq} modes, H^{y}_{11} field is dominant and these can also be identified as quasi-TE modes. Similarly H^{x}_{pq} modes with dominant H^{x}_{11} field are also known as quasi-TM modes. These modes can also be classified as E^{x}_{pq} and E^{y}_{pq} modes [29].

1.4.2 Single mode condition:

Optical devices based on planar light-wave circuits (PLCs) are attractive which is because of their excellent performance and compact size. An optical waveguide is usually required to be single mode in order to avoid the influence from higher-order modes. It should be notified that in most of the sensors and telecommunication applications, waveguides are required to support a single mode, which means only the fundamental mode is allowed to propagate in the waveguide. As a result, it is important to determine the single-mode condition before the (PLCs) is designed. To satisfy the single-mode condition, the SOI rib waveguide is etched shallowly giving a weak confinement and in which case a high integration density is impossible. The great difference between the refractive indices of Si and SiO_2 (or air) has attracted and the size of the Si waveguide will be reduced to several hundred nanometers. Such kind of Si waveguide is usually called a nano-Si rectangular waveguide. The scattering loss (per unit length) for a nano-Si rectangular waveguide is much larger [30], [31] than that for a conventional waveguide of micrometer dimensions which is due to the sidewall roughness. On the other hand, the total size of the (PLCs) devices based on nanowire waveguides are reduced significantly compensating for the large scattering loss per unit length. As a result, the total loss in a PLC device based on nanowire waveguides can be sufficiently low for practical use.

1.5 Waveguide Birefringence:

A high index-contrast between the silicon core and the cladding (SiO_2 or air) is that SOI waveguides generally have a considerable birefringence [32]. Consequently, considerable drawbacks that limit device performance and compromise its operation are resulted following polarization mode dispersion (PMD), polarization dependent loss (PDL), and polarization dependent wavelength (PDλ) [33]. In addition, a very strict fabrication tolerance is imposed on silicon photonic devices through the dependence of polarization. For example, by considering a photonic filter based on a 10 μm radius ring resonator with 300 nm wide silicon waveguide, a difference of the resonant wavelengths between TE and TM modes larger than 100 GHz is induced by the fluctuation of the core width of only 1 nm (i.e., 300 ± 1 nm) [34]. Therefore, a suitable approach to minimize the dependence of microphotonic silicon device performance on the polarization of the incoming light is achieved due to the accuracy of improvement of technological process, such as electron-beam (e-beam) lithography and reactive ion etching (RIE), as well as the design of silicon photonic devices characterized by zero birefringence [35]. Other proposed solutions can be the use of high birefringent silicon nitride (Si_3N_4) bent waveguides on SOI platforms [36], the control of SOI waveguide birefringence by inducing silicon core [37] and the depositing of thin doped top layer onto silicon wafer [38].

For large SOI ridge waveguides (with a ridge height of 1-5 μm), the birefringence is on the order of 10^{-3}-10^{-5}, while the birefringence of SOI nanowires can be several orders of magnitude higher [9]. Accordingly it is possible to achieve a nonbirefringent SOI optical waveguide by optimizing the waveguide dimension [39,40,41,42,43,44]. But this is only in theory and only for the case with large SOI ridge waveguides, because fabrication inaccuracies cause the typical dimensional variations which generate an acceptable birefringence [44]. The polarization-independent is almost possible for the case of the demonstrated AWG demultiplexer made of 5-μm thick SOI ridge waveguides by simply optimizing the waveguide dimension. For the case of using thinner SOI ridge waveguides, the birefringence can also be minimised by controlling the stress generated from an oxide cladding [45].

In comparison with the case of large SOI ridge waveguides, it is much harder to achieve a desired nonbirefringent SOI nanowire experimentally by controlling the waveguide dimensions because of the stringent fabrication tolerance. The results of experiments show that large structural birefringence of SOI nanowires [46] usually causes significant polarization dependence in the photonic integrated devices [9]. Moreover, the polarization-dependent properties can vary significantly compared to those devices based on the micrometer optical waveguides. For example, for a SOI-nanowire AWG device, both the channel wavelength and the channel spacing are polarization sensitive. This makes conventional polarization-compensation approaches ineffective, so new solutions are demanded. However, it should be taken into account that and other specific technological solutions such as the subnanometer accuracy are not always suitable for large scale integration and low cost fabrication.

In [47], [48], [49], directional coupler, multimode interference (MMI) couplers and microring resonators are proposed as special approaches to reduce the polarization sensitivity of SOI-nanowires-based photonic integrated devices.

1.6 Polarization Diversity:

It is not always suitable for large scale integration and low cost fabrication to make use of Sub-nanometer accuracy and other specific technological solution such as the use of stressed or doped layer.

The scheme of polarization diversity is generally adopted as an optimal approach to solve the problem of the polarization dependence which is affecting high refractive index contrast SOI photonic devices [7], [11], [50], [51], [52], [53]. The schematic proposed in Figure 1.1 indicates that an analysis of the principle of operation of a polarization diversity circuit can help to achieve this purpose. The basic architecture of a polarization diversity circuit consisting of polarization splitters (PSs) and rotators (PRs) [54], [55] are represented in the configuration sketched in Fig.1.1. In particular, by using a polarization splitter (i.e., PS1) the orthogonal polarization components of the input light are split into two different waveguides at the input section. Consequently, in order to obtain a 90° rotation, a polarization rotator (i.e., PR1) is employed in one of the waveguides.

In this way, a single polarization is obtained and the two paths will probably be operated in parallel with identical structures. In this case, only TE polarized optical signals are used in operation of the functional device.

For instance, a polarization sensitive microring resonator could be employed for optical signal processing like filtering or add-drop multiplexing. At the output section, a symmetrical configuration, including one polarization splitter (i.e., PS2) and one polarization rotator (i.e., PR2) will be implemented to combine both polarizations without any interference. In conclusion, it is also possible to use spot size converters (SSC) at both output and input sections for coupling the optical signal from the input fibre to the circuit and vice versa. Finally, the schematic in Figure.1.1 represents that it is possible to design a reciprocal configuration in which the functional device operates with only TM polarized optical signals.

These polarization diverse components are also very useful for various applications such as coherent optical communications, which attract a lot of attention for long-haul optical fibre communications. The reason is that it improves the spectral efficiency in a great deal [16]. Similar coherent technology can be also very efficient in the future network-on-chip for optical interconnects. In this case, it is better to implement the polarization diversity components which are very small. Recently the polarization-handling technology also plays an important role for realizing integrated photonic quantum circuits [56]. Furthermore, the polarization-diversity technology is considered as a general solution to eliminate the polarization-sensitivity of photonic integrated devices based on SOI nanowires and at the end enables polarization transparent silicon nano-PICs [7], [57], which play an important role in the fibre-fed cases. There are usually numerous elements integrated monolithically for these applications, and consequently obtaining ultrasmall elements consisting of polarization diversity components is desired, which can be realized by using the giant birefringence of SOI nanowires.

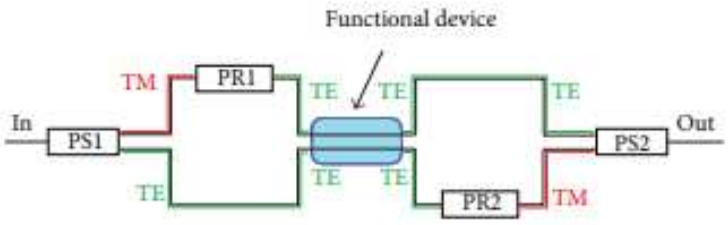

Figure 1.1 Schematic of a polarization diversity photonic circuits [55].

1.7 Aim and Objective Thesis:

The discussion given so far provides an insight of the potential work on ultra-compact polarization diversity components for the future silicon nanophotonic integrated circuits. The primary aims and objectives of this research work can be summarized as follows:

1. A rigours, accurate and efficient finite element method based on vector **H**-field variational formulation has been implemented for the analysis of optical waveguide.
2. To implement the least squares boundary residual (LSBR) method together with the exploitation of the accurate modal solutions obtained from the finite element method in order to achieve an accurate waveguide junction analysis and to account for power transfer phenomenon.

3. To study in depth of the silicon strip waveguide by the use of vector **H**-field finite element method. The characteristics of the modal **H**-field profiles, will be studied in detail, in doing so the critical size of such waveguides can be determined.

4. To design and characterise a novel compact silicon nano-wire waveguide polarization rotator device by implementing the finite element method and least squares boundary residual method to show that such device can achieve almost 100% polarization conversion with very short device lengths.

5. To apply the full vectorial numerical techniques consist of finite element method and least squares boundary residual method in order to study the characteristics of passive polarization splitter based on silicon-on-insulator (SOI) technology. To design an efficient device which splits transverse electric (TE) and transverse magnetic (TM) polarizations into two separate ports, which can be fabricated by using a compact silicon nano-wire waveguides technology.

The Finite Element Method

2.0 Introduction:

The natural starting point for analysing how wave propagate in passive devices is the set of wave propagation equations first formulated by James Clark Maxwell. Various numerical methods for passive devices solve these equation by using the Galerkin and moment methods [58],[59], transfer matrix method [60], finite-element-based methods [61], [62], and finite-difference-based methods [63].

The numerical methods available for modelling of photonic devices are immensely varied to suit the needs of users. These methods have origins in mathematics, physics and engineering which many of them have been applied successfully in various disciplines. Closed-form solutions and analytical methods were historically used for modelling phenomena/devices to a large extent. The more complicated devices became progressively, the more limited the applicability of analytical became leading to variation numerical methods. This caused a rapid growth in low-cost computing power, which brought about the computerizing or automation of numerical algorithms. Therefore, in recent years it has been possible to have accurate simulations of highly complex devices through the use of computerized codes based on different numerical methods.

This chapter introduces numerical modelling in photonics, discussing the extent to which each method is applicable and examining the limitation of each. It also explains some of the basic assumptions and simplifications made to Maxwell's equations and what follows from them. These physical insights accompany the mathematical treatment. We discuss criteria for choosing a modelling method, and assess the finite element method against them. We also examine the theoretical background to the ***H***- field Finite Element Method (FEM) as a method of analysing waveguides, as well as the method of suppressing spurious solutions by including a penalty factor. Finally, the Least Squares Boundary Residual (LSBR) method used in the discontinuity analyses when butt coupling uniform guided-wave section are also presented.

2.1 General Equation:

2.1.1 Maxwell's Equation:

The evolution of electromagnetic fields is described by Maxwell's first-order differential equations which describe the intimate coupling between the electric and magnetic fields. The equations relates spatial variation of one field with the time varying of other. They combine with four electromagnetic field vectors, using one discipline that govern electromagnetic wave phenomena.

The four vectors are: the electric field intensity ***E*** (Volts/meter). Magnetic field intensity ***H*** (Amperes/meter), the electric flux density ***D*** (Coulomb/meter^2) and the magnetic flux density ***B*** (Tesla). The boundary-value problem with the FEM is defined by differential forms.

Differential equation forms of Maxwell's equations in a homogenous, lossless dielectric medium is:

$$\nabla \times \boldsymbol{E} + \frac{\partial \boldsymbol{B}}{\partial t} = 0 \tag{2.1}$$

$$\nabla \times \boldsymbol{H} - \frac{\partial \boldsymbol{D}}{\partial t} = \boldsymbol{J} \tag{2.2}$$

$$\nabla \cdot \boldsymbol{D} = \rho \tag{2.3}$$

$$\nabla \cdot \boldsymbol{B} = 0 \tag{2.4}$$

Where ρ, is the dielectric charge density (coulomb/metre^3); **J**, is the electric current density (Ampere/metre^2). The conservation of charge or the continuity of current can be expressed (holds for **J** and the charge density**,** ρ) as:

$$\nabla . \boldsymbol{J} = -\frac{\partial \rho}{\partial t} \tag{2.5}$$

The associated constitutive equations for the medium can be written as:

$$\boldsymbol{D} = \hat{\varepsilon}\boldsymbol{E} \tag{2.6}$$

$$\boldsymbol{B} = \hat{\mu}\boldsymbol{H} \tag{2.7}$$

Where $\hat{\varepsilon}$ and $\hat{\mu}$ represent the permittivity and permeability of the medium, respectively. They can be tensors, but for simplicity they are written here merely as ε, and μ.

In photonics, the interest in solving Maxwell's equations is not free space or in one continuous medium, but it is consider for a different devices such as optical fibres, Bragg gratings, slot waveguides and many other devices.

The ε is the permittivity and μ is the permeability of the medium which can be defined by:

$$\varepsilon = \varepsilon_o \varepsilon_r \tag{2.7}$$

$$\mu = \mu_o \mu_r \tag{2.8}$$

Where ε_o, ε_r, μ_o and μ_r are the permittivity of the vacuum (8.854 x 10^{-12} Farad/meter), the relative permittivity of the medium, the permeability of the vacuum (4π x 10^{-7} Henry/meter) and the relative permeability of the medium, respectively.

Photonic devices contain more than one material medium, with several boundaries between the different medium. Therefore, it is necessary to take into account of boundary conditions, when considering the continuity of the electric and magnetic fields inside these components.

2.1.2 Boundary Conditions:

For a waveguide with arbitrary dielectric distribution, the satisfying of the boundary conditions at these interfaces is necessary. They must be met at the boundary surface when two different media 1 and 2 come in contact. If the unit normal vector $\boldsymbol{n}$, is directed from medium 1 to medium 2 as shown in Fig. 2.1 in the absence of any surface currents (J = 0) and surface charges (ρ = 0), the following boundary conditions apply:

1. The tangential components of the electric field must be continuous.

$$\boldsymbol{n}\times(\boldsymbol{E}_1-\boldsymbol{E}_2)=0 \tag{2.9}$$

$$\therefore \quad E_{t1}=E_{t2}$$

2. The tangential components of the magnetic field must be continuous.

$$\boldsymbol{n}\times(\boldsymbol{H}_1-\boldsymbol{H}_2)=0 \tag{2.10}$$

$$\therefore \quad H_{t1}=H_{t2}$$

3. The normal components of the electric flux density must be continuous.

$$\boldsymbol{n}\cdot(\boldsymbol{D}_1-\boldsymbol{D}_2)=0 \tag{2.11}$$

$$\therefore \quad D_{n1}=D_{n2}$$

$$\therefore \quad \varepsilon_1 E_{n1}=\varepsilon_2 E_{n2} \Rightarrow \ \therefore \quad E_{n1}\neq E_{n2} \tag{2.12}$$

Where ε_1 and ε_2 are the permittivity in medium 1 and 2, respectively and, also at the interface, $\varepsilon_1 \neq \varepsilon_1$. It is mention that, the relative permittivity and refractive index are related by $\varepsilon_r = n^2$.

4. The normal components of the 12btains12 flux density must be continuous.

$$\boldsymbol{n}\cdot(\boldsymbol{B}_1-\boldsymbol{B}_2)=0$$

(2.13)

$$\therefore \quad B_{n1}=B_{n2}$$

$$\therefore \quad \mu_1 H_{n1}=\mu_2 H_{n1}$$

Where μ_1 and μ_2 are the relative permeability in medium 1 and medium 2, respectively and for most nonmagnetic media, $\mu_1 = \mu_2 = 1$.

$$\therefore \quad H_{n1}=H_{n2} \tag{2.14}$$

The above boundary condition will ensure the continuity of the normal component of the magnetic field at the boundary.

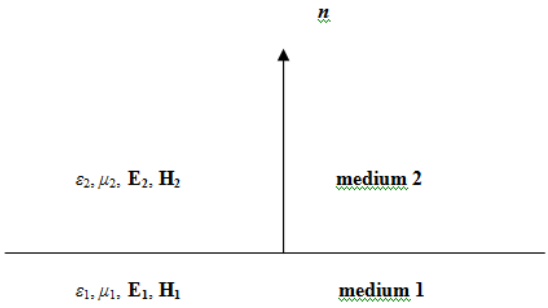

Fig. 2.1 Boundary between two media of refractive indices n_1 and n_2 where n, is the unit vector normal to the interface.

Two more boundary conditions include; a perfect electric conductor or a perfect magnetic conductor which are encountered in practical waveguide problems.

When one of the two media becomes a perfect electric conductor (PEC), the necessary boundary condition on any electric conducting boundaries is:

$$n \times \boldsymbol{E} = 0 \qquad n \cdot \boldsymbol{H} = 0 \tag{2.15}$$

For the lack of surface currents, the boundary condition requires certain magnetic field vector components which must be vanish. That is $\boldsymbol{H}_n = 0$, in the absence of surface currents $\boldsymbol{J} = 0$ and $\boldsymbol{H}_t = 0$.

When one of the two media becomes a perfect magnetic conductor (PMC), a magnetic wall (MW) boundary condition, an useful approach to improve modal field symmetry a magnetic wall boundary condition is imposed as:

$$n \times \boldsymbol{H} = 0 \qquad n \cdot \boldsymbol{E} = 0 \tag{2.16}$$

The above boundary condition with vanishes of $\boldsymbol{E}$ will ensure the continuity of the normal component of the magnetic field, $\boldsymbol{H}$, at the boundary.

Solutions of Maxwell's equations adequately comply with both the constitutive relations and the boundary conditions, and mark out the electromagnetic fields inside any photonic devices. According to these conditions a unique solution for the problem is obtained.

It is mention that, how boundary conditions are classified depends on their mathematical representation and the condition imposed. These natural boundary conditions for a given formulation can be same as the actual boundary condition, for this case, they can be left free.

In some other cases they can be forced, in order to take advantage of the symmetry of the waveguide, to reduce the number of elements in FEM and also decreasing the order of the matrices to impose complementary symmetry for the waveguides. The above boundary conditions can be classified as follows:

$\Phi = 0$ Homogenous Dirichlet (2.17)

$\Phi = k$ Inhomogenous Dirichlet (2.18)

$\frac{\partial \Phi}{\partial \boldsymbol{n}} = 0$ Homogenous Neumann (2.19)

Where Φ is a specific component of the vector electric or magnetic field and k is presented as a constant value and $\boldsymbol{n}$ is the unit vector normal to the surface.

The rate of change of the field is represented by the Neumann boundary conditions when it is directed out of the surface.

2.1.3 Formularization of Domains:

So far, it has been evident that boundaries separate a device into regions divided with electromagnetic properties, or they impose natural or force boundary conditions. However, boundaries may also be considered to exist at infinity. By this it is meant that the device has a finite extent in the x, y, and z directions even though the surrounding space extends to infinity. Therefore the boundaries between the outer domain of the device and its surrounding space needs special care, if the fields and the physical quantities such as power and energy are interested and they must well defined, and also a unique solution to provide for them.

Where artificial boundaries are set in order to limit the computational domain as a finite size, optical fields travelling toward these boundaries in the simulation are reflected back into the computational region. Thus, these boundaries have to be assigned an absorbing properties to avoid the computational error of this unphysical reflection minimize, which is a purely numerical feature.

A number of absorbing methods have been devised and they include the transparent boundary conditions (TBC) [64], perfectly matched layer boundary conditions (PML) [65] and other [66]. The wave equations have to be modified accordingly. For maintenance the simplicity, mathematical considerations imposed by these boundary conditions are not treated here. How these conditions are implemented in the FEM will be 14btains14e, later.

To obtain the behaviour of the fields inside the device described by the solution to Maxwell's equations, (2.1)-(2.4) can be recast into an appropriate form that reflects physical considerations as well as practical ones related to the mathematical solution techniques and approximation required.

2.1.4 Time Harmonic and Time-Dependent Solutions:

In their coupled differential equation format, Maxwell's equations describe electric and magnetic field propagation in spatial and temporal terms. Thus, the equations in this format are appropriate study for dependent of time phenomena, such as pulse propagation, reflections, radar, or antennae.

They also describe the evolution of the fields in exotic system such as metamaterials, through inclusion of the required equations consist of the permittivity (ε) and permeability (μ).

In many practical applications, the steady state equation form in optical field as a function of the physical coordinates are interested. In the discipline of time harmonic fields, continuous wave (CW) operation at a single frequency is a favourable, where time evolution is not of interest, and can be removed from the analysis. The field can be written in phasor representation:

$$\begin{bmatrix} \boldsymbol{E}(x,y,z,t) \\ \boldsymbol{D}(x,y,z,t) \\ \boldsymbol{H}(x,y,z,t) \\ \boldsymbol{B}(x,y,z,t) \end{bmatrix} = \begin{bmatrix} \boldsymbol{E}(\mathrm{x},\mathrm{y},\mathrm{z}) \\ \boldsymbol{D}(\mathrm{x},\mathrm{y},\mathrm{z}) \\ \boldsymbol{H}(\mathrm{x},\mathrm{y},\mathrm{z}) \\ \boldsymbol{B}(\mathrm{x},\mathrm{y},\mathrm{z}) \end{bmatrix} e^{j\omega t} \tag{2.20}$$

This notation allows replacement of the time derivatives in (2.1) and (2.2) by the term jω (after suppressing $e^{j\omega t}$ on both sides of the equation) since:

$$\frac{\partial e^{j\omega t}}{\partial t} = \mathrm{j}\omega e^{j\omega t}$$

Thus, (2.1)-(2.4) can be written in the form:

$$\nabla \times \boldsymbol{E} = -j\omega \boldsymbol{B} \tag{2.21}$$

$$\nabla \times \boldsymbol{H} = j\omega \boldsymbol{D} + \boldsymbol{J} \tag{2.22}$$

$$\nabla . \boldsymbol{D} = \rho \tag{2.23}$$

$$\nabla . \boldsymbol{B} = 0 \tag{2.24}$$

The continuity equation becomes:

$$\nabla . \boldsymbol{J} = -j\omega\rho \tag{2.25}$$

2.1.5 Wave Equations:

It is not always an easy task to find the solution of a system for the coupled differential equations with boundary conditions. Further, in computational solutions for a six component to the electric and magnetic fields must be stored at every point in the device's physical domain. This may not be reasonable for devices of practical size. To deal with this, one approach is to decouple the first-order Maxwellian curl equations, (2.1)-(2.4) and obtain second-order differential equations for only one field, called the wave equations. We eliminate $\boldsymbol{H}$ from (2.1) by use of the constitutive relations [(2.6)].

$$\nabla \times (\nabla \times \boldsymbol{E}) = \omega^2 \varepsilon \mu \boldsymbol{E} \tag{2.26}$$

A similar approach is followed to eliminate *E* and obtained:

$$\nabla \times \frac{1}{\varepsilon}(\nabla \times \boldsymbol{H}) = \omega^2 \mu \varepsilon \boldsymbol{H} \tag{2.27}$$

Further, using the vector identity $\nabla \times (\nabla \times \boldsymbol{A}) = -\nabla(\nabla . \boldsymbol{A}) - \nabla^2 \boldsymbol{A}$ and rewriting $\nabla(\nabla . \boldsymbol{E}) = -\nabla(\ln \varepsilon) . \boldsymbol{E}$ yields the vector wave equation:

$$\nabla^2 \boldsymbol{E} + \omega^2 \varepsilon \mu \boldsymbol{E} = -\nabla(\ln \varepsilon) . \boldsymbol{E} \tag{2.28}$$

$$\nabla^2 \boldsymbol{H} + \omega^2 \varepsilon \mu \boldsymbol{H} = -\nabla(\ln \varepsilon) \times \nabla \times \boldsymbol{H} \tag{2.29}$$

2.1.6 General Scalar and Vector Equations:

The electric and magnetic fields in Eqs. (2.28) and (2.29) are vectors. The magnitude and spatial dependence play a part in the nature of the field and its mathematical explanation. The vector field which is also known as the hybrid field, contains both longitudinal component in the direction of the field propagation and also transverse component that are perpendicular to the direction of the propagation and these components are coupled. The terms on the right hand side (RHS) of the vector equations in Eqs. (2.28) and (2.29) describe the coupling of the components. In homogeneous media, $\nabla . \varepsilon = 0$ and due to RHS vanishes, leading to decoupling of the transverse and longitudinal field components. However, inhomogeneous media, the term on the RHS can be neglected in comparison to the other terms in the equations, called the scalar or weakly guiding approximation. In this case $\frac{\nabla \varepsilon}{\varepsilon}$, $\frac{\nabla \mu}{\mu}$ are small compared with the length scale over which **E** and **H** solve in space, and it is also leads to decoupling of the transverse and longitudinal components:

$$\nabla^2 E = \omega^2 \varepsilon \mu E \tag{2.30}$$

$$\nabla^2 H = \omega^2 \varepsilon \mu H \tag{2.31}$$

Equations (2.30) and (2.31) are homogeneous and represents the scalar wave equations for the electric and magnetic fields, respectively. The field components in the solution of these equations are independent from each other and both are transverse, but the longitudinal components are negligible.

2.2 Modal Solutions in Waveguides:

For structures where the refractive index is almost homogeneous in one direction and considered in *z* direction of propagation and only varies in the transverse directions, modes of the structure, which can be obtained by solving Eqs. (2.28) – (2.31). Modes of a system represent the eigenfunctions or eigenstates of the system. For a simple photonic device such as a waveguide, modes are the steady state, discrete solutions to the wave equation that

satisfy the boundary conditions for obtaining refractive index distribution, $n(x,y)$. When light is coupled into the waveguide, modes show the equilibrium superposition of the waves. On coupling light into the device, it will be guides in the form of one or more of the modes of that device. Each guided mode has characteristics such as an effective index and field distribution that are unique and do not change with time or even for different power of the incident light. Modal analysis imply the process of finding the propagation constant and the field profiles of all modes that a waveguide can support and also to be able to determine the nature and behaviour of the electric and magnetic field inside the device under CW operation.

Several methods for finding the modes in waveguides exist. These methods can be considered into three groups, namely the analytical, semi-analytical and the numerical solutions. An analytical solution can be obtained for stepped 2-D optical slab waveguides and stepped optical fibre. However, in all practical optical waveguide with 2-dimentional confinement, analytical techniques are not possible and some other methods have to be considered. Among the semi-analytical approaches are methods such as the effective index method [67], Marcatili's method [68] and its improvement with perturbation techniques [69] and the coupled-mode analysis [70].

Semi-analytical approach, works well for uniform waveguides or coupled waveguides carrying few modes. However, when the refractive index distribution is too complex, then numerical methods have to be used. There are several numerical methods in photonics, some of them are scalar and a few others treat with both vector and scalar problems. Numerical solutions can also be grouped into two categories and these are the domain solution and the boundary solution. Some of the example of the domain solutions include the finite element method (FEM), Finite Difference Method (FDM), Variational Method (VM) and Multilayer Approximation Method (MAM). The boundary solutions include the Boundary Element Method (BEM), Point Matching Method (PMM) and Mode Matching Method (MMM).

A brief description of the most commonly used analytical and numerical solution techniques for modelling in opto-electronics will be presented in subsequent sections.

2.2.1 Marcatili's Method:

Marcatili's Method (MM) was one of the first semi-analytical approximation methods to be developed for the analysis of buried waveguides and couplers [68]. The method was developed for guiding structures with large dimensions and a small birefringence (less than 5%). The field is assumed to exist in the rectangular waveguide core region and also in the four neighbouring cladding regions which are obtained by extending the width and the height of the waveguide to infinity.

The field is also assumed to vary sinusoidally in the core region and exponentially in the four cladding regions, thus the field is approximated to the field in two slab waveguides; one vertical and the other horizontal. Two transcendental or eigenvalue equations for each slab waveguide are solved simultaneously to give the axial propagation constant. Marcatili's method works well in the regions far from cut-off but does not provide a satisfactory solution close to cut-off region [71].

2.2.2 Effective Index Method:

The Effective-Index (EI) method was first proposed by Knox and Toulios in 1970 [72] with a view to improving Marcatili's earlier approach [68] for the fundamental mode of a simple rectangular core waveguide. This resulted in the effective index method becoming one of the most popular methods in the 1970s for the analysis of optical waveguides whereby the rectangular structure is replaced by an equivalent slab with an effective refractive index obtained from another slab. The rectangular dielectric waveguide is divided into two slab waveguides in each transverse direction. The initial step solves the transcendental equation for a vertical slab waveguide by applying the appropriate boundary conditions. The effective index calculated in this step is then used as the refractive index of the horizontal slab waveguide and by solving the eigenvalue equation gives a good approximation to the effective index of the original waveguide structure. This method is significantly more efficient than those methods that solve the rectangular structure directly since only the solutions for slab waveguides are required. The advantage of the effective index method is that it can be applied to a wide variety of structures including channel waveguides, strip waveguides and arrays of such waveguides [73] and also for various types of optical fibre devices [74], [75]. The disadvantage of this method is that it does not give good results when the structure operates near cut-off region. However, the simplicity and speed of the method have encouraged many engineers to search for different approaches that will improve the accuracy of the effective index method which subsequently lead to many different variants of the effective index method to be developed including the effective index method based on linear combination of solutions [76], [77] or the effective index method with perturbation correction [73].

2.2.3 Numerical Methods:

As a rapid growth in the integrated photonic circuits have included the use of arbitrary shaped dielectric waveguides, which include many arbitrary inhomogeneous and also anisotropic, which do not treat themselves with analytical solutions. Therefore, to deal with them, it is needed to expanding the numerical method for analysing such waveguides. These methods can be used to finding accurate characterisation of most of devices. Since the advent of computers with large memories, considerable attention has been paid to methods of obtaining numerical solutions of the boundary and initial value problems. These methods are usually evaluated in terms of their generality, accuracy, efficiency and complexity.

For an appropriate modelling method for a given structure, some factors with regard to the selection of numerical methods for analysing optical waveguide problems are given as follow:

- The modelling need of a structure depends on the shape of the cross-section area, whether it is convex or concave or also it is uniform or non-uniform.
- Whether the modelling of a structure requires the fundamental or higher order modes.
- Whether the method requires near cut-off frequency or modal field distribution.
- Whether the method is employed with more than two homogenous media.
- The requirement of accuracy needed for eignvalues and perhaps eigenfunctions.

- The accuracy of the technique in modelling the dielectric boundaries and regions.
- Whether the method has a mechanism of generating spurious numerical solutions and if so whether the method can identify and/or eliminate them.
- The computational efficiency of the method, including its computer storage requirements.
- Whether the method should be programmable specifically for each region of the structure separately.
- Whether a computer program requiring human intervention or some exploratory work with the computer is needed.
- The assumptions and limitations of the numerical approach, for specific cases.

The commonly used numerical solution methods will be briefly discussed in the following subsections.

2.2.3.1 Boundary Element Method:

The Boundary Element Method (BEM) is interpreted as a combination technique of the conventional boundary integral equation method and discretisation techniques [78]. The BEM is a boundary solution method and therefore the fields would be required only at the nodes which are on the boundaries of the region. The derivation of the integral equations with respect to the unknown fields at boundaries is obtained by the method of weighted residuals or the Green's formula. These integral equations are then discretised to a set of linear equations to be solved for the numerical solutions. The BEM can be used for the analysis of arbitrary shaped discontinuities as is with the finite element method, but the boundary element method can be performed using far fewer nodes than by finite element method. Moreover, the BEM can handle unbounded field problems easily and therefore has the possibility of modelling domains extending to infinity without an infinite element analysis which is often performed in the finite element method. However, the BEM can only be applied to homogenous structures [79] and also it has been known that the matrices involved are dense matrices unlike those used with the finite element method which are spares. Therefore, the finite element method can be treated as more numerically efficient than the boundary element method.

2.2.3.2 The Point Matching Method:

The Point Matching Method (PMM) is one of the oldest and simplest 'boundary solution' technique for the analysis of isotropic homogenous dielectric waveguides. Its application was first reported by J. E. Goell [80] to investigate the propagation characteristics in rectangular cross section dielectric waveguides. The numerical analysis used in the technique by Goell is based on expressing the internal and external fields in term of circular harmonics. The field inside the dielectric and outside the dielectric are expressed by a sum of Bessel functions and modified Bessel functions multiplied by trigonometric functions, respectively and their derivatives. By matching the tangential fields at optimally selected points around the boundary called 'matching points', a system of linear equations is obtained. By applying the condition of nontrivial solution, a characteristic equation including the propagation constant

is obtained and solved for each mode eigenfunction by standard matrix techniques. The point matching method is capable of analysing dielectric waveguides with arbitrary cross sections and composite structure and also computing coupling coefficients between two rectangular rods. Improved results for the point matching method were reported [81] by rotating the grid of equiangularly spaced matching points in order to place a matching point at the corner of rectangular dielectric waveguide. However, the point matching is not suitable for the analysis of a 3-D waveguides structures with inhomogenous index distribution such as graded index fibres.

2.2.3.3 Mode Matching Method:

The Mode Matching Method (MMM) which is also known as the Equivalent Network Method is an approximate solution method for the analysis of open dielectric waveguides [82]. In this approach the structure is artificially bounded and the waveguide cross section is vied in terms of constituent parts of building blocks, which are usually portions of uniform dielectric layered structures interfaced by the dielectric step discontinuities. Then each constituent is analysed separately and all the parts are put together to compromise the final structure of interest.

A transverse equivalent network for the structure is obtained by representing the uniform dielectric regions as uniform transmission lines and by characterising the step discontinuities as transformers. From this, the dispersion relation can be derived to obtain the waveguide propagation characteristics. In the earlier analysis of the mode matching method due to the artificial bounding of the structure, the continuous spectrum [82] and TE and TM coupling at the sides of the waveguide are neglected. Dagli and Fonstad [83] reported a modified approach, which take into account the continuous spectra. Rather than artificially bounding the structure to discretise the continuous modal spectrum, here, they are discredited by converting integrals into summations using suitable basis function expansions. In [84] and [85] reported a vectorial wave analysis of rectangular optical waveguide using equivalent network method by taking the TE-TM coupling and the discrete continuous spectrum coupling into account.

2.2.3.4 Spectral Index Method:

The Spectral Index (SI) method may be used to find quickly and easily the guided modes and propagation constants of semiconductor rib waveguides [86] and [87]. Here the true open structure is replaced by slightly larger, partially closed one, which is simpler to analyse, in order to model penetration of the optical into the cladding. The spectral index method can be expressed using steps in the region below the rib. First of all, the Fourier transform is applied in order to reduce the dimensionality of the problem to a one-dimensional structure and the field is expressed in spectral space using Fourier transform.

Next, in the rib region the wave equation is exactly expressed using Fourier series in terms of cosine and sine functions then two solutions are linked by employing a transfer relationship and consequently, giving a transcendental equation which can be solved for the propagation constant of the original rib structure. The presence of the strong discontinuities at

the dielectric interfaces is dealt with by using an effective rib width and an effective outer slab depth. The spectral index method has been extended to include rib coupler problems [88], [89] cases with loss and gain [90] and also it has been used to analyse multiple rib waveguides [91].

2.2.3.5 Beam propagation Method:

The beam propagation method was first applied to optoelectronics in 1980 [92] and the solutions for the optical waveguides can be made to generate mode-related properties such as propagation constants, relative mode powers and group delays with high precision and considerable flexibility.

The Beam propagation Method (BPM) describe the evolution of the total field propagation along a waveguide and it is the most widely used tool in the study of light propagation in longitudinally varying waveguides such as tapers, Y-junction, bends and gratings.

For employing the beam propagation method, it is necessary to use the mathematical model solutions. In this case, the wave equation can be expressed as:

$$\frac{\partial^2}{\partial_z^2}\psi = \mathrm{H}\psi \tag{2.32}$$

where ψ, $\boldsymbol{H}$ shows the electric or magnetic field and the operator consist of the transverse spatial derivate and also the refractive index variation, respectively. Through the solution of (2.32) the optical field in BPM algorithms is followed to be travelling primarily of its z direction, which is discretized into small intervals so that the field at the beginning of the step is given its natural form. The device input where the field is launched may be considered as a laser.

The BPM algorithm then propagates the field through the interval in its default direction, which in final process of the propagation is employed as the source for the next field propagation step and so on. The total length along the z axial is product the number of propagation steps, n, and as well as path of each step, Δz. A few popular methods related to BPM methods are considered as a follow:

The initial BPM is based on the Fast Fourier Transform (FFT) and only solves the scalar wave equations under paraxial approximation. Therefore the FFT-BPM was only developed for the case of weakly guiding structures, neglecting the vectorial properties of the field. Several numerical algorithm to treat the vectorial wave propagation (vector BPM) using the finite difference method, have been reported [93], [94], [95]. The VBPMs are capable of simulating polarized or even hybrid wave propagation in strongly guiding structures. Recently, the finite element method has been utilised to develop BPM approaches.

A unified finite element beam propagation method has been reported [96] for both TE and TM waves propagation in strongly guiding longitudinally varying optical waveguide. In [97] has reported a full-vectorial BPM algorithm based on the finite element method to characterise 3-D optical guided wave devices.

Beam propagation methods are explained in type of vector or scalar, which its equation from the (2.32) can be extracted in the scalar form:

$$\frac{\partial^2 \psi}{\partial z^2} = \nabla_t^2 \psi + k_0^2 n^2(x,y,z)\psi(x,y,z) \tag{2.33}$$

where $\nabla_t^2 = \frac{\partial^2}{\partial x^2} + \frac{\partial^2}{\partial y^2}$ in Cartesian coordinates and shows the transverse spatial derivate operator.

The scalar BPM algorithms treat with the total field and all the guided and radiation modes in the structure is exist. It is noted that the specific form of (2.33), explains the moving of the waves in both directions as the forward and the backward. In generally (2.33) deal with the reflections. BPM algorithms that solve (2.33) are termed as bi-directional methods and are very iterative in nature. More detail of bi-directional methods will be described in 2.2.3.5.1.

2.2.3.5.1 Bi-Directional in Beam propagation Method:

Using from (2.33) in a quadratic equation to express of two components, one representing the forward and the other one backward propagation elements. The reflected field is assumed to be known at the input of the structure, then a BPM-based transfer matrix approach is applied to relate the forward and backward fields at the output to those at the input. Based upon this relation and the boundary conditions, the reflected field is found in an iterative manner. This approach is simple to program and has the advantage that only one pair of fields must be stored [98].

An iterative bi-directional BPM approach, which deals with problems involving an arbitrary number of dielectric interfaces and/or high index contrast. This approach has significantly reduced time and memory requirements compared to other multi-interface techniques.

2.2.3.5.2 Imaginary axis-distance in Beam propagation Method:

Although the BPM has been seen to be useful to study the wave evolution along longitudinally varying structures, but the imaginary distance beam propagation method (ID-BPM) also has shown its usefulness as a mode solver of optical waveguides [99], [100]. By propagating an arbitrary starting field along, in general, a complex axis, and with the appropriate selection of the step size, different modes can be sequentially extracted from the starting field. The main advantages of using the ID-BPM are that the matrices of the BPM are in general complex, so lossy waveguides can be treated as conventionally as those that are lossless, without any additional numerical effort. Also, the incorporation of an absorbing boundary condition into the BPM algorithm makes it capable of dealing not only with guided modes but also with leaky modes as well.

2.2.3.6 Finite Difference Method:

The Finite Difference Method (FDM) is one of the oldest and perhaps the most commonly used numerical techniques in analysing dielectric waveguide problems. Its application to the

modelling of optical waveguides dates from the early eighties, originally evolving from previous finite difference models for metal waveguides [101]. The finite difference method discretises the cross section of the device that is being analysed and it is therefore suitable for modelling inhomogeneous media and complicated boundaries. In FDM, it is necessary to define the a finite cross section by enclosing the dielectric guide in a rectangular box with the side walls as either electric or magnetic walls and the field at these boundaries are assumed to be very small. The enclosed cross section is divided into a rectangular mesh allowing for the material discontinuities only along mesh lines [102]. The nodes are placed on mesh points so that each node can be associated to maximum of four differential vector, semi-polarized or scalar wave equation can be approximated in terms of the fields at the neighbouring nodes of the mesh. Taking into account the continuity and discontinuity conditions of the electric and magnetic components at the field interfaces an eigenvalue problem is generated which can be solved in order to obtain the modal propagation constants and their modal field profiles. The accuracy of the method depends on the mesh size, the assumed nature of the electromagnetic field (scalar, polarized or vector) and the order of the finite difference scheme used. When the device operates near cut-off the size of the box has to be sufficiently large to allow substantial penetration of the field into the substrate. If a uniform mesh used then it can result in a very large number of nodes and large matrices and therefore the disadvantages like long run times and high memory requirements may become apparent.

2.2.3.7 Finite Element Method:

The Finite Element Method (FEM) is well-established numerical method for the solution of a wide range of guided wave problems. It can be very easily applied not only to optical waveguides of any shape but also to optical waveguides with any refractive index distribution an to those with any anisotropic materials or nonlinear materials. This method is based upon dividing the problem region into non-overlapping patchwork of polygons, usually triangular elements. The field over each element is then expressed in terms of polynomials weighted by the fields over each element.

By applying the variational principle to the system functional and thereby differentiating the functional with respect to each nodal value, the problem reduces to a standard eigenvalue matrix equation. This is solved using iterative techniques to obtain the propagation constants and field profiles [103], [104].

The accuracy of the finite element method can be increased by using finer mesh. A number of formulations have been reported, however, the full vectorial **H**-field formulation is the most commonly used and versatile method in modelling optical waveguides due to much easier treatment of the boundary conditions. This method can accurately solve the open type waveguide problems near cut-off region and much better results were obtained by introducing infinite elements to extend the region of explicit field representation to infinity [105].

One drawback associated with this powerful vector formulation is the appearance of spurious or non-physical solutions. Suppression of these spurious solutions can be achieved by introducing a penalty term into the variational expression [106]. In order to eliminate the spurious solutions completely, another approach is employed using the edge elements [104],

[107]. In modelling more complex structures, the finite element method is considered to be more flexible than the finite difference method due to the ability of employing irregular mesh. Since this method is used in this work, a more detailed description of the finite element method will be presented next.

2.3 Elementary aspect of the Finite Element Method:

The Finite Element Method (FEM) has emerged as one of the most successful numerical methods for the analysis of waveguides from low frequency to microwave to optical region. It is needed capable of solving waveguides arbitrary refractive index distribution. In this thesis a full-vectroial **H**-field based FEM has been used to characterise waveguide operating at optical frequencies.

Basic idea about the FEM is that it is breaking up a complex domain into smaller elements and finding reasonable equation for them. The unknown field, Ψ, is approximated by a functional equation which usually describe as a polynomial to be solved (such as (2.27)). This interpolation function reads the value of Ψ at the element nodes and is used to obtain values of the unknown field at any point inside the element. Each small element has its own independent interpolation function. Therefore for each element, e, field express the unknown field as:

$$\Psi^{e} = \sum_{i=0}^{n} N_i \Psi_i \qquad (2.34)$$

Where n is the total number of nodes in a given element and N_i is the interpolation function. Generally, higher degrees of the polynomial solutions closer to the actual field. As the function is required to be continuous everywhere inside the element, the solution yields the explicit functional form, which can be computed the value of Ψ at any point in the element, including those points that do not fall on vertices/nodes. Further, because the field is an interpolation of values at the vertices, if two element share vertices due to common boundary, the field will be continuous across the boundary (Figure 2.2).

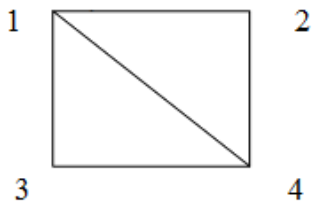

Figure 2.2 Two triangular elements with a common boundary.

In the FEM, instead of differential equations for the system investigation, corresponding functional to which a variational principle [108], [109] is applied are set up, where the region of interest is divided into the so called, elements, an equivalent discretized model for each element is constructed, and then all the element contributions to the system are assembled.

In other words, the finite-element method can be considered a subclass of the Ritz-Galerkin [110] method, in which piecewise defined polynomial functions are used for trial functions and infinite degrees of freedom of the system are discretized or replaced by a finite number of unknown parameters.

In classic analytical procedures without subdivision processes, the system is modelled using analytical functions defined over the whole region of interest, and therefore these procedures are applicable only to simple geometry and materials. Of the various forms of discretization possible, one of the simplest is the finite-difference method, and its original versions use a regular mesh, i.e. a rectangular grid with nodes at the intersections of orthogonal straight lines. However, a regular grid is not suitable for curved boundaries or interfaces, because they intersect gridlines obliquely at points other than the nodes. Moreover, a regular grid is not suitable for problems with very steep variations of fields.

The FEM is somewhat similar to the finite difference method, however in the FEM, the field region is divided into elements; that is, into subregions. Elements can have various shapes and sizes, such as triangles and rectangles, allowing the use of an irregular grid.

Therefore, the FEM is suitable for problem with sharp variations of fields. Furthermore, this approach can be easily adapted to inhomogeneous and isotropic problems, and it is possible to systematically increase the accuracy of solutions obtained as necessary. Furthermore, the FEM scheme can be stabilished not only by the variational method but by the Galerkin method, which is a weighted residual method. Therefore, the FEM may be applicable to problems where a variational principle does not exist.

2.4 Installing the FEM approach:

FEM or any numerical method would be a tool to simulate the behaviour of electromagnetic fields in a photonic device. Initially, some physical parameters such as a modal effective index, resonant frequency, and power or loss in the device are interested and it is necessary to understand how these physical quantities are connected to the way in the FEM setting up. The FEM can be governed by way of two approximate which one of them the variational method [109] and another one the Galerkin formulation [110]. Both approaches lead to expressions that can be discretized with the FEM methodology and reduced to eigenvalue matrix equations, the starting point for each is different. Each method study in the following subsections.

2.4.1 Variational formulation:

The variational method requires minimizing an expression (functional) set up in terms of variables such as the fields, potentials in the system, with respect to a small variation in these variables, which can be defined as:

Parameter = SV {Expression/functional involving fields, potentials} (2.35)

Where SV is stationary value, allows expressing the physical quantity of interest as a parameter to be determined by minimizing the functional.

Establishing a variational principle is the main task, and often a good starting point is energy type expressions such as stored electromagnetic energy or power flow. Minimizing the expression that would normally contain Hermitian or quadratic form of the fields involved yields the associated Euler-Lagrange equations. The use of a variational approach in the formulation of a finite element analysis, has the advantage that is allows a particular analysis and also programming the computer, to be generalised to solve any problem of the same mathematical nature. The latter approach is the Rayleigh-Ritz method [111]. The difference in the variational method and FEM approaches is that the former minimizes the functional over the entire domain, while in the latter a global functional obtained from contributions in every element is minimized. In the following, the vector ***H*** field formulation by the variational route by using the wave equation (2.26) will be expressed. This equation can be written as a generalized eigenvalue equation:

$$\mathrm{LH} - \lambda \mathrm{MH} = 0 \tag{2.36}$$

Where the vector operators L and M are defined as:

$$\mathrm{L} = \nabla \times \varepsilon^{-1} \nabla \times \tag{2.37}$$

$$M = \mu \tag{2.38}$$

And the eigenvalue:

$$\lambda = \omega^2 \tag{2.39}$$

It can be shown that minimizing the functional [108]:

$$\mathrm{F(H)} = \frac{1}{2} < LH, H > - \frac{\lambda}{2} < MH, H > \tag{2.40}$$

Is equivalent to writing the variational expression in the form:

$$\lambda = S.V. \frac{< LH, H >}{< MH, H >} \tag{2.41}$$

Where S.V stands for stationary value of, when the operator L in (2.34) is self –adjoint, that is,

$$< L\phi, \psi > = < \phi, L\psi > \tag{2.42}$$

And positive definite:

$$< L\Phi, \Phi > = \begin{cases} > 0 & \Phi \neq 0 \\ = 0 & \Phi = 0 \end{cases} \tag{2.43}$$

The self-adjoint property leads to symmetric matrices. H is a trial function and the symbol < > represents the inner product. For vector fields the inner product can be defined as:

$$< f, g >= \int g^* . f dV \tag{2.44}$$

Given the components of one function in the direction of the others, while the asterisk denotes complex conjugation. Substituting *L, M,* and λ in (2.41) and using (2.44) it obtains:

$$\omega^2 = S.V. \frac{\iint (\nabla \times \mathrm{H})^* . \varepsilon^{-1} (\nabla \times H) dV}{\iint H^* . \mu H dV} \tag{2.45}$$

Equation (2.45) is the full vectorial ***H*** field functional that is obtained by the variational method.

Minimization of this expression gives the frequency of guided modes in optical structures. Minimization of (2.41) or finding the stainory value of the expression given by (2.45) yields a matrix equation of the form:

$$[A]\{\Phi\} = \lambda [B]\{\Phi\} \tag{2.46}$$

This particular formulation yields ω for a given β or wavelength and is described in (2.6.2).

2.4.2 The Galerkin Method:

The Galerkin method is a form of the weighted residual method (WRM) [112]. Given a deterministic problem expressed mathematically in the form:

$$L_1 u = v \tag{2.47}$$

Where L_1 is a linear operator, for example, a double or single differential, u is the unknown function and υ represents the source or excitation, it is possible to seek a solution in terms of an expansion of some known basis functions, u_i with unknown coefficient, b_i:

$$u = \sum_{i=1}^{N} u_i b_i \tag{2.48}$$

The basis functions, u_i, are a complete set, and appropriate choice of the coefficients, b_i, minimizes the error residual defined as:

$$R(s) = L_1 u - v = L_1 \sum_{i=1}^{N} u_i \, b_i(s) - v(s) \tag{2.49}$$

The error residual can only be zero when the expansion in (2.48) represents the exact solution. In any other situation the error is nonzero, and our effort is to minimize it by choosing a set of weight function, w_i, such that the error residual, *R(s)* is orthogonal to each of the w_i that also form a complete set:

$$< \{L_1 \sum_{i=1}^{N} u_i b_i (s) - v(s)\}, \{w_j(s)\} >= 0 \quad \text{for j = 1,2,...N} \tag{2.48}$$

Where (2.48) leads to matrix form

$$[L_1][u] = [v] \tag{2.49}$$

In our case, the unknown function, u, is the magnetic field, ***H***, and the operator L_1 is defined as $L_1 = \nabla \times \varepsilon^{-1} \nabla \times -\omega^2 \mu$ and the source, $[v] = 0$.

The above procedure is known as the generalized Galerkin method, or the method of moments. The orthogonality of the weight functions to the error residual is implemented as an inner product defined in (2.50). The formulation obtained via the Galerkin method is equivalent to that the variational method. An important point to note is that the inner product in (2.50) requires integration of a function of the form $\int\{L_1 \sum_{i=1}^{N} u_i \; b_i(s) - v(s)\}.\{w_j(s)\}dV$. When the operator L_1 contains terms like $\frac{\partial^2}{x^2}$, it becomes necessary to choose weight functions (and shape functions for the Galerkin method) that are double differentiable (the strong form of the WRM). However, when the integral is simplified by integrating by parts ($\int u\, dV = uv - \int v\, du$), we can reduce the burden to first-order differentiability and obtain the weak form of the WRM.

The Galerkin formulation therefore directly solves the governing differential equation (2.47) for the boundary value problem and discretises it in smaller domains, the contributions from which summed up, and uses the the basis and weight functions to arrive at the matrix equation, (2.51). The two equations, (2.46) and (2.50) are similar in nature.

2.5 Scalar and Vector form in Variational approach:

In section 2.1.6 how to make the weakly guiding approximation with low index contrast described and due to use the scalar wave equation. In the following section finite element form for both scalar and vector forms will be described.

2.5.1 Scalar form:

Scalar form can be applied in situations where the field can be described as predominantly TE or TM mode. In this case the magnitude of the longitudinal components is very small. Therefore, it is sufficient to follow the variations of any one of the transverse components, that satisfy (2.30) or (2.31), respectively, and to express the fields as quasi-transverse electric (TE) or quasi-transverse magnetic TM modes.

In planar (infinite slab) waveguides, mode can be purely TE or TM. However, in optical waveguides with 2-dimensional confinement, the modes are never purely TE or TM and are denoted by quasi-TE or quasi-TM modes. The scalar formulation is preferred due to the less complex equation that has to be solved. It has been applied to the analysis of wave propagation in homogeneous isotropic media [113], open boundary problem [114], and even for the analysis of anisotropic waveguides [115]. For quasi-TE modes in the domain Ω, where the domain field components is E_x, the formulation can be expressed as [116]:

$$L = \iint_{\Omega}\left[\left(\frac{\partial E_x}{\partial x}\right)^2 + \left(\frac{\partial E_x}{\partial y}\right)^2 - k_o n^2 E_x^2 + \beta^2 E_x^2\right] d\Omega \tag{2.52}$$

Where β is the propagation constant and n is the refractive index and k_0 is the free-space wavenumber. An FEM program based on the above mentioned functional yields β^2 are the eigenvalue of the matrix equation for given k_0. For quasi-TM modes, H_x is the dominant field component; the formulation may be given as follows:

$$L = \iint_{\Omega} \frac{1}{n^2}\left[\left(\frac{\partial H_x}{\partial x}\right)^2 + \frac{1}{n^2}\left(\frac{\partial H_x}{\partial y}\right)^2 - k_o H_x^2 + \frac{1}{n^2}\beta^2 H_x^2\right] d\Omega \tag{2.53}$$

Where β, n, and k_0 have their usual meaning defined above. A FEM program based on this functional yields k_0^2 as the eigenvalue of the matrix equation for a given propagation constant β. The scalar functional defined in (2.52) has the continuity of $\frac{\partial E_x}{\partial \hat{n}}$ as the natural boundary condition, and the functional in (2.53) has the continuity $\left(\frac{1}{n^2}\right)\left(\frac{\partial H_x}{\partial \hat{n}}\right)$ as the natural boundary condition, where $\hat{n}$ is the outward normal unit vector.

The scalar explanation for the quasi-TE and quasi-TM modes and using the Ritz variational method in order to minimize the functional (2.52) and (2.53) and obtain the FE solution is considered. Details of how to the interpolation functions are chosen and the nodes/vertices are created are discussed in 2.6.3.

2.5.2 The Vector Formulation:

Vector formulations of the Maxwell equations manage a means for solving wave propagation problems where all six electromagnetic field components are present. The scalar formulation is inadequate for the hybrid modes of anisotropic or inhomogeneous waveguide problems. Therefore, for the guided modes of a three dimensional which modes are hybrid in nature, using the vector wave analysis is required for a precise evaluation of their propagation characteristics.

They also provide better solution convergence for some modal types as compared to corresponding scalar formulations. There are many types of finite element methods for such vector analysis, depending on which electromagnetic field component is used for formulation. They include:

- The longitudinal electromagnetic ($\boldsymbol{E}_z$ and $\boldsymbol{H}_z$) field components;
- The transverse electromagnetic field components; ($\boldsymbol{H}_t$+$\boldsymbol{E}_t$)
- The transverse electric field components; $\boldsymbol{E}_t$
- The transverse magnetic field components; $\boldsymbol{H}_t$
- The three electric field components; $\boldsymbol{E}$
- The three magnetic field components; $\boldsymbol{H}$
- The six electromagnetic field components (three each of the $\boldsymbol{E}$ and $\boldsymbol{H}$ fields).($\boldsymbol{E}$+$\boldsymbol{H}$)

Of all these formulations, those that minimize the number of components to store (by considering, for example, only E and H fields) are computationally more efficient. The accuracy they yield is important along with the ease with which boundary conditions can be implemented. Some of the more popular formulations will be discussed next.

The vector *E*-field approach was first applied in English and Young [117]. This formulation is suitable for generally anisotropic and lossless problems. The natural boundary condition in this formulation corresponds to a magnetic wall; therefore it becomes essential to force the electric wall boundary condition ($n \times E = 0$). Such a condition is quite difficult to impose

for an irregular structure. It requires an additional integral to insure continuity of the fields at the dielectric interfaces. The most advantageous formulation is the vector ***H***-field formulation [105], [106], [118] in terms of all three components of the magnetic fields. It is valid for general anisotropic problems with a nondiagonal permittivity tensor. The natural boundary condition for this formulation is that of the electric field ($\boldsymbol{n}\times\mathbf{E} = 0$, $\mathbf{n}.\mathbf{H} = 0$); therefore for arbitrary conducting guide walls, the boundary can be left free. In dielectric waveguides, the permeability, μ, is always assumed to be that free space.

Therefore, each component of ***H*** is continuous in the entire region and arbitrary variation of the refractive index in the waveguide cross section does not necessitate imposition of interface boundary conditions. Total vector formulations that involve both the ***E*** and ***H*** fields [119] have also been proposed. However, these do not have much advantage over the vector ***H*** field formulation due to computational burden associated with storing and calculating all the six components needed.

2.5.2.1 The Vector H-field Formulation:

The vector ***H***- field formulation is more suitable for dielectric waveguide problems because the magnetic field is continuous everywhere and the natural boundary conditions correspond to those of the electrical wall therefore no forced boundary conditions at the boundaries are required. This functional for the vector formulation is given by (2.45).

$$\omega^2 = \frac{\int (\nabla \times \boldsymbol{H})^* \cdot \hat{\varepsilon}^{-1} \cdot (\nabla \times \boldsymbol{H}) d\Omega}{\int \boldsymbol{H}^* \cdot \hat{\mu} \cdot \boldsymbol{H} d\Omega} \tag{2.54}$$

Where ω, is the angular frequency, Ω is the waveguide cross-section $\hat{\varepsilon}$ and $\hat{\mu}$ are the permittivity and permeability tensors respectively.

To obtain the stationary solutions of the formulation (2.54) this is minimised with respect to each of the variables, which are the unknown nodal field components H_x, H_y and H_z. This minimisation leads to a matrix eigenvalue equation as stated in equation (2.46), where [*A*] is a complex Hermitian matrix and [*B*] is a real symmetric and positive-definite matrix. Because of the general 90^0 phase difference between the axial and transverse components of the ***H***-field [120], the Hermitian matrix [*A*] can be transformed to a real symmetric matrix for a loss-less problem. In general, the matrices [*A*] and [*B*] are quite sparse.

The eigenvectors {Φ} represents the unknown field components at the nodal points for different modes with λ as their corresponding eigenvalues and also λ is proportional to ω^2. In order to obtain a solution for a given wavelength, the propagation constant, β value has to be changed iteratively until the output eigenvalue corresponds to that wavelength. By varying β over the range of interest, it is possible to calculate the dispersion characteristics for the various modes. However, the above formulation (as well as the ***E***-field) yields spurious solutions because the divergence condition, $\nabla \cdot \boldsymbol{H} = 0$ is not satisfied automatically, therefore alternative approach, such as the penalty coefficient method [105], [118] have been proposed to eliminate those non-physical solutions. This method will be discussed in follow.

2.5.2.2 Spurious Solution:

The vector variational formulations suffer from the form of spurious or non-physical modes, which mixed up with the physical and accurate solutions during the computations. There are various methods exploited to detect these non-physical solutions from the physical method. The characteristic of spurious solutions is the inconsistency and the random fashion of the field varied. The explanation to the cause of these solutions could be due to the enforcement of the boundary conditions or nonzero divergence of the trial fields [64], [105]. In electromagnetic waveguide problems the spurious modes do not arise if the trial field precisely satisfies the condition $\nabla . B = 0$. Spurious modes occur in a full vector formulation where the divergence-free condition is neither implied nor forced and are distinctive in giving particularly high values of $\nabla . B$.

To eliminate these spurious modes, it is necessary to differentiate between the physical and the non-physical solutions. For a physical mode, mathematically, its eigenvector satisfies the condition $\nabla . H = 0$. So it is possible to identify the spurious solutions from the physical ones by calculating the $\nabla . H = 0$ for each solution over the waveguide cross section. The solution with low values of $\nabla . H = 0$ are the real modes whilst those with high values are the spurious modes. Based on this phenomenon, Rahman and Davies [106] developed the so called penalty function method. It is a useful way of imposing certain constraints on solution variables. The method has been used in structural engineering problems to impose specific boundary conditions. This method was used to successfully eliminate these spurious solutions in problems of microwave or optical waveguide and improving the quality of the field. In this approach, an additional integral is added to the variational formulation equation (2.52), which satisfies the condition $\nabla . H = 0$. The penalty term can be written as [49].

$$\omega^2 = \frac{\int (\nabla \times \boldsymbol{H})^* \frac{1}{\varepsilon} \cdot (\nabla \times \boldsymbol{H}) d\Omega + \frac{p}{\varepsilon_o} \int (\nabla \cdot \boldsymbol{H})^* (\nabla \cdot \boldsymbol{H}) d\Omega}{\int (\boldsymbol{H}^* \cdot \mu \boldsymbol{H}) d\Omega} \tag{2.55}$$

Where p is the dimensionless penalty factor. The value of p is often taken to be around $1/\varepsilon_n$, where ε_n is the dielectric constant of the core of the waveguide. In this method the divergence free constraint is imposed in a least-squares sense and the larger the penalty factor the more heavily the constraint is implemented giving a further reduction of the spurious modes from the spectrum. The penalty function also improves the quality of the eigenvectors without increasing the order of the matrix in the eigenvalue problem.

2.6 FEM Formulation in Mathematical Aspect:

The differential operator equations which describe the physical problem are replaced by an appropriate extermum functional J, which is the variational for the desired quantity. The problem can be regarded as obtaining the solution **H** over a specific region in the transverse plane so that the boundary conditions and also the extermum requirement are satisfied. The axial dependence is assumed the form $e^{-j\beta z}$ and the transverse plane is used for discretisation.

2.6.1 Discretisation of the Domain:

The discretisation of the domain into sub-regions (finite element) is the initial stage in the finite element method. The shape, size, number and configurations of the elements have to be chosen carefully such that the original body or domain is simulated as closely as possible without increasing the computational effort needed for the solution. Each element is essentially a simple unit within which the unknown can be described in a simpler manner. There are various types of elements available as a one, two and three dimensional elements for using in finite element formulations. When the geometry and material components can be considered in terms of two independent spatial coordinates, the two-dimensional elements as shown in Fig.2.2 can be used. The elementary and popular element for analysing an arbitrary waveguide structure in two-dimensional is the triangular element. Selection of the element size, dictates the accuracy in the final solution. By dividing the waveguide cross section into triangular elements, the unknown **H** is also considered as to be discretised into corresponding sub-regions. These elements are easier to analyse rather than analysing the distribution over the whole cross section. As shown in Fig 2.3, the transverse plane is covered with a grid of discrete nodes which are the vertices of each triangular element. The values of **H** at these nodal points are the basic unknowns. The intersections of the sides of the triangular elements are called nodal lines.

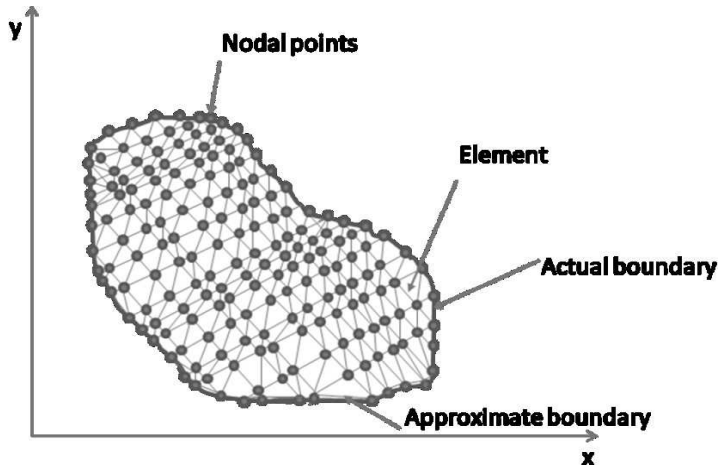

Fig. 2.3 Finite element discretisation of a waveguide with triangular elements.

2.6.2 Shape Functions:

For the approximation of the field over each element, it is important to consider a continuous function that is allowed to vary in a linear way over the element region. The function varying is bounded by the fact that at the nodal points, which should takes values equal to the nodal values in terms of ϕ_1, ϕ_2 and ϕ_3. In this case, the functions have to be expressed in regarding to its nodal values. These functions are referred to the shape functions.

The continuous field function $\phi(x, y)$ in the problem domain can be replaced by a set of discrete values (ϕ_i, i = 1,2,3,.....,m), where m is the total number of nodes. Across the adjacent

triangles this function will be continuous. For these functions to be acceptable which they must satisfy some conditions between the elements; usually the continuity of the field across the boundaries is preferred. For each first order triangle element ϕ is interpolated continuously, this shown in Fig. 2.3 which can be performed by representing the nodal shape function (interpolation function) as N_i (x,y). Thus, using the interpolation function the element field can be written as:

$$\phi_e(x,y) = \sum_{i=1}^{3} N_i(x,y) \cdot \phi_i \tag{2.56}$$

Where ϕ_i are the nodal field values. The equation (2.56) can also be shown in a matrix form as:

$$\phi_e(x,y) = [N_1 \ N_2 \ N_3] \begin{Bmatrix} \phi_1 \\ \phi_2 \\ \phi_3 \end{Bmatrix} \tag{2.57}$$

$$\Rightarrow \quad \phi_e(x,y) = [N]\{\phi_e\} \tag{2.58}$$

Where $[N]$ is referred to as shape function matrix and the column vector $\{\phi_e\}$ is the vector corresponding to the element nodal field values at the three vertices of the triangular.

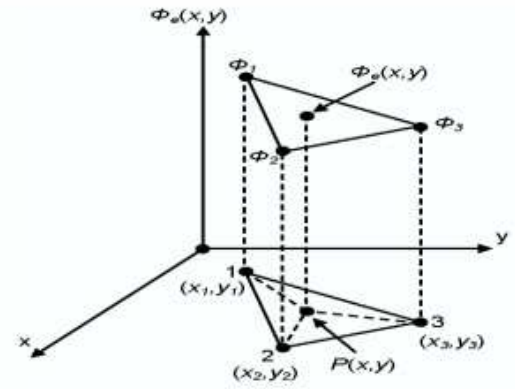

Fig. 2.4 Illustration the First-order triangular element with the components.

The first-degree polynomial ($a+bx+cy$) is used over each element for a simple first order triangular element. The element shape function can be presented in a matrix notation as:

$$[N]^T = \begin{bmatrix} N_1 \\ N_2 \\ N_3 \end{bmatrix} = \frac{1}{2A_e} \begin{bmatrix} x_2y_3 - x_3y_2 & y_2 - y_3 & x_3 - x_2 \\ x_3y_1 - x_1y_3 & y_3 - y_1 & x_1 - x_3 \\ x_1y_2 - x_2y_1 & y_1 - y_2 & x_2 - x_1 \end{bmatrix} \begin{bmatrix} 1 \\ x \\ y \end{bmatrix} \tag{2.59}$$

Where T denotes a transpose, x_1, x_2, x_3, y_1, y_2, and y_3 are the x and y coordinates of the three nodes respectively. A_e is the area of the triangular element given as:

$$A_e = \frac{1}{2}\begin{bmatrix}1 & x_1 & y_1\\ 1 & x_2 & y_2\\ 1 & x_3 & y_3\end{bmatrix} = \frac{1}{2}\{(x_2y_3 - x_3y_2) + (x_3y_1 - x_1y_3) + (x_1y_2 - x_2y_1)\} \quad (2.60)$$

The shape function matrix can also be written as:

$$[N]^T = \begin{bmatrix}N_1\\ N_2\\ N_3\end{bmatrix} = \begin{bmatrix}a_1 + b_1x + c_1y\\ a_2 + b_2x + c_2y\\ a_3 + b_3x + c_3y\end{bmatrix} \quad (2.61)$$

And a_i, b_i, c_i (i = 1,2,3) are the constants for a given element and calculated as:

$$a_1 = \frac{x_2y_3 - x_3y_2}{2A_e}$$

$$b_1 = \frac{y_2 - y_3}{2A_e} \quad (2.62)$$

$$c_1 = \frac{x_3 - x_2}{2A_e}$$

The values of a_2, b_2, c_2, a_3, b_3, and c_3 can be obtained by a cyclic exchange in equation (2.62) simultaneously. The shape functions N_i can also be expressed in terms of the areas of the triangle shown earlier in Fig. 2.3 as:

$$N_i = \frac{\text{area of triangle P23}}{\text{area of sub triangle 123}} \quad (2.63)$$

Similarly N_2 and N_3 can be defined in the same way. Hence, N_i has the following property:

$$\sum_{i=1}^{3} N_i = 1 \quad (2.64)$$

The shape function N_1 yields the value 1when evaluated at the node 1(x_1,y_1) and the value 0 at nodes 2 and 3 and all the other points passing through the nodes on the line. This is the unique first-degree interpolation functions N_2 and N_3, the value 1 is at nodes 2 and 3, respectively, and the other nodes are 0.

2.6.3 Element and Global Matrices:

The solution of the optical waveguide problem by the FEM can be transformed to a standard eigenvalue problem as in equation (2.46) where matrices [*A*] and [*B*] are known as global matrices and consist of the summation of the element matrices for each triangular element of the discretised cross-section of the optical waveguide.

In this section, the assembly of the element and global matrices is shown, with respect to the shape functions and the nodal field values of each triangular element, based on the

variational formulation. Considering each triangular element, the three unknown ***H***-field components H_x, H_y and H_z of the magnetic field can be written as follows:

$$H_x(x,y) = \begin{bmatrix} N_1 & N_2 & N_3 \end{bmatrix} \begin{bmatrix} H_{x1} \\ H_{x2} \\ H_{x3} \end{bmatrix}$$

$$H_y(x,y) = \begin{bmatrix} N_1 & N_2 & N_3 \end{bmatrix} \begin{bmatrix} H_{y1} \\ H_{y2} \\ H_{y3} \end{bmatrix} \tag{2.65}$$

$$H_z(x,y) = \begin{bmatrix} N_1 & N_2 & N_3 \end{bmatrix} \begin{bmatrix} H_{z1} \\ H_{z2} \\ H_{z3} \end{bmatrix}$$

Where H_{xi}, H_{yi} and H_{zi} for i=1,2,3 are the x, y and z components of the nodal magnetic fields. The nodal magnetic field vector $[H]_e$ for each element can be described as:

$$[H]_e = \begin{bmatrix} H_x(x,y) \\ H_y(x,y) \\ H_z(x,y) \end{bmatrix} = \begin{bmatrix} N_1 & N_2 & N_3 & 0 & 0 & 0 & 0 & 0 & 0 \\ 0 & 0 & 0 & N_1 & N_2 & N_3 & 0 & 0 & 0 \\ 0 & 0 & 0 & 0 & 0 & 0 & N_1 & N_2 & N_3 \end{bmatrix} \begin{bmatrix} H_{x1} \\ H_{x2} \\ H_{x3} \\ H_{y1} \\ H_{y2} \\ H_{y3} \\ H_{z1} \\ H_{z2} \\ H_{z3} \end{bmatrix} \tag{2.66}$$

In more compact form, the above equation (2.66) can be written as:

$$[H]_e = [N]\{H\}_e \tag{2.67}$$

Where $\{H\}_e$ is the column vector which contains the three components of the nodal field values of the elements and $[N]$ is the shape function matrix. Also using equation (2.67), the curl of ***H*** equation can be written as:

$$(\nabla \times H)_e = \nabla \times [N]\{H\}_e = \begin{bmatrix} 0 & -\frac{\partial}{\partial z} & \frac{\partial}{\partial y} \\ \frac{\partial}{\partial z} & 0 & -\frac{\partial}{\partial x} \\ -\frac{\partial}{\partial y} & \frac{\partial}{\partial x} & 0 \end{bmatrix} [N]\{H\}_e = [Q]\{H\}_e \tag{2.68}$$

Where the matrix $[Q]$ can be written as:

$$[Q]=\begin{bmatrix} [0] & -\frac{\partial}{\partial z} & \frac{\partial [N]}{\partial y} \\ \frac{\partial [N]}{\partial z} & [0] & -\frac{\partial [N]}{\partial z} \\ -\frac{\partial [N]}{\partial y} & \frac{\partial [N]}{\partial y} & [0] \end{bmatrix} \tag{2.69}$$

Where [0] = [0 0 0] and [N] = [N_1 N_2 N_3] and some of the shape function derivatives are assumed substituted using equation (2.64) as shown:

$$\frac{\partial N_1}{\partial x} = b_1,\ \frac{\partial N_2}{\partial x} = b_2,\ \frac{\partial N_3}{\partial x} = b_3$$

$$\frac{\partial N_1}{\partial y} = c_1,\ \frac{\partial N_2}{\partial y} = c_2,\ \frac{\partial N_2}{\partial y} = c_3 \tag{2.70}$$

The values of the constants b_1, b_2, b_3, c_1, c_2 and c_3 were given earlier in equation (2.62). By substituting the expressions shown in equations (2.67) and (2.68) in to the variational formulation of equation (2.69), the vector **H**-field formulation functional for an element can be obtained as:

$$\omega^2 = \frac{\int (\nabla \times H)^* \cdot \hat{\varepsilon}^{-1} \cdot (\nabla \times H) d\Omega}{\int (H^* \cdot \hat{\mu} \cdot H) d\Omega}$$

$$\Rightarrow \omega^2 = \frac{\int_{\Delta} ([Q]\{H\}_e)^* \cdot \hat{\varepsilon}^{-1} \cdot [Q]\{H\}_e d\Omega}{\int_{\Delta} ([N]\{H\}_e)^* \cdot \hat{\mu} \cdot ([N]\{H\}_e) d\Omega} \tag{2.71}$$

$$\Rightarrow \omega^2 = \frac{\int_{\Delta} \{H\}_e^T [Q]^* \cdot \hat{\varepsilon}^{-1} [Q]\{H\}_e d\Omega}{\int_{\Delta} \{H_e^T\}[N]^T \cdot \hat{\mu}([N]\{H\}_e) d\Omega}$$

Re-arranging the last part of the above equation (2.71), the following can be obtained:

$$J_e = \int_{\Delta} \{H\}_e^T [Q]^* \cdot \hat{\varepsilon}^{-1} \cdot [Q]\{H\}_e d\Omega - \omega^2 \int_{\Delta} \{H\}_e^T [N]^T \cdot \hat{\mu}[N]\{H\} d\Omega \tag{2.72}$$

Where Δ represents the integration over the triangular element domain. T and * denote the transpose of a matrix and the complex conjugate transpose, respectively. The [Q] matrix was defined earlier in equation (2.69). A transpose operation on this matrix would define the [Q]* matrix. For isotropic material, the relative permittivity ε_r is a scalar quantity. For waveguides

consisting of anisotropic material the relative permittivity ε can be taken as a tensor represented by a 3×3 matrix and the inverse of the matrix should be implemented.

The total function, J associated with the whole cross-section of the waveguide can be obtained by summing J_e of all the individual elements as:

$$J = \sum_{e=1}^{N} J_e \tag{2.73}$$

Where *N* is the number of elements.

The minimisation of the functional given in equation (2.73) can be performed by differentiating with respect to the field nodal values and equating it to vary as below:

$$\frac{\partial J}{\partial \{H\}_e} = 0 \tag{2.74}$$

Thus the following relation can be obtained:

$$\frac{\partial J}{\partial \{H\}_e} = 2\int_{\Delta} \{H\}_e [Q]^* \cdot \hat{\varepsilon}^{-1} [Q] d\Omega - 2\omega^2 \int_{\Delta} [N]^T \hat{\mu} [N] \{H\}_e d\Omega = 0 \tag{2.75}$$

$$\therefore \int_{\Delta} [Q]^* \cdot \hat{\varepsilon}^{-1} [Q] d\Omega \cdot \{H\}_e - \omega^2 \int_{\Delta} \mu [N]^T [N] d\Omega \cdot \{H\}_e = 0$$

Thus the following eigenvalue equation can be obtained:

$$[A]\{H\} - \omega^2 [B]\{H\} = 0 \tag{2.76}$$

Where the matrices [*A*] and [*B*] can be defined as:

$$[A] = \sum_{e=1}^{N} [A]_e = \sum_{e=1}^{N} \int_{\Delta} [Q]^* \hat{\varepsilon}^{-1} [Q] d\Omega$$

$$[B] = \sum_{e=1}^{n} [B]_e = \sum_{e=1}^{n} \hat{\mu} \int_{\Delta} [N]^T [N] d\Omega \tag{2.77}$$

[*A*] and [*B*] are the global matrices of the eigenvalue equation, while $[A]_e$ and $[B]_e$ represent the element matrices. Column matrix {*H*} contains all **H**-field nodal values over the whole cross section of the waveguide structure. The evaluation of the elements $[A]_e$ and $[B]_e$ are shown in the Appendix.

When solving waveguide problems by using finite elements, the key factor affecting storage requirements and computational effort is the choice of algorithm to solve the matrix equation. The global matrices [*A*] and [*B*] shown in equation (2.77) are highly sparse. The sparcity increases with the order of the matrices and decreases with the polynomial order of the shape functions. It is obvious that using higher order basis functions, one may obtain a

more accurate solution of the problem under consideration. However, the added disadvantage to that is that the process involves increasing the programming effort, particularly when considering waveguide problems with material anisotropy, infinite elements and penalty functions. In addition to that higher order polynomials for a given matrix order increases the density of the matrix although this can be handled with reasonable effort by using a sophisticated matrix solver.

2.7 The finite element method and Least Squares Boundary Resdiual Methods:

The finite element method (FEM) is described to be more accurate and versatile in order to find the modal solution than the other available techniques [103], this is because, to its preferable properties, which have been already mentioned in detail. The FEM can be employed to arbitrary shaped guides which the refractive indices, nonlinearities and anisotropies can have arbitrary profiles.

The power transfer efficiency between two guides can be calculated from the supermodes of the coupled structures, which requirement that the accurate eigenvalues and eigenvectors can be obtained. Since the FEM can be able to calculate the supermodes of the propagation constants from the coupled structures, this approach is used where possible. To find the power transfer efficiency, the coupled mode [121-122], or simple overlap integral [123] techniques can be used. An alternative and a powerful tool to analyse the coupled structures is the employment of the least squares boundary residual method. The advantage of this method, compared to other available techniques, is that it can calculate the reflection coefficients of the modes, and also it enforces the satisfaction of the field continuity more rigorously at the interfaces.

2.7.1 Using the data from the finite element results:

In majority of the coupled devices the calculation of only the propagation constants and the field values is not so much concern. Hence an additional technique [121-123] has had to be developed to finding the power transfer from the input to the intermediate or output sections. However, it has been shown in this study that the LSBR method is an accurate and versatile numerical tool to calculate the power transfer between the coupled waveguides. The LSBR method employees the propagation constants and the field values generated by the finite element and also used to calculate the transmission and the reflection coefficient at the discontinuity interfaces. From the LSBR technique the continuity of the tangential components of the **E**-field and **H**-field in the least squares sense over the discontinuity interface by considering a several modes to yield the general scattering matrix are accommodated. The LSBR method can be applied to a wide range of discontinuity problems, consist of abrupt changes at the transverse plane between arbitrary guiding structures of uniform cross section.

By applying the LSBR, problems including the vertical shifts, horizontal misalignments, sudden changes of width or height change in guide dimensions or materials or combinations of all these verities can be solved and the other hand the LSBR method is employed to find the optimum matching of the two side waveguides by controlling the geometries and material

properties of the guides. The LSBR method is rigorously convergent, and the error minimisation being global rather than sampled and the method has flexibility of introducing and electric/magnetic weighting factor to balance electric and magnetic field continuity errors.

2.7.2 Analysis of the waveguide discontinuities:

Considering the abrupt junction of two dielectric waveguides as illustrated in Fig. 2.5. It is assumed that the discontinuity junction is excited by an incident wave of one mode from side I. This incoming wave is partly reflected, partly transmitted and radiated at the junction interface. Let E_t^{in} and H_t^{in} be the transverse components of the electric and magnetic fields of the incident wave respectively. Some of the incident wave is reflected back into the side I. On the other hand, many modes will be generated at the discontinuity plane to satisfy the boundary conditions. These can be guided or radiated modes in both sides of the discontinuity.

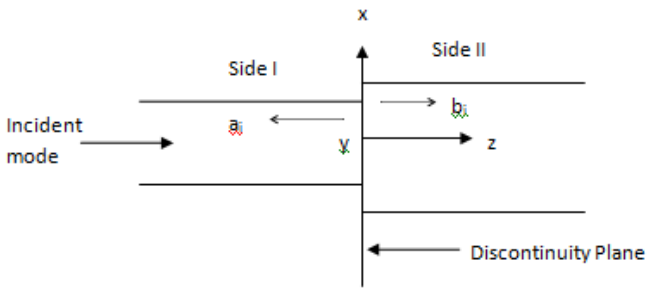

Fig. 2.5 Discontinuity representation of LSBR.

The total transverse electric and magnetic fields E_t^I and H_t^I in side I and E_t^{II} and H_t^{II} in side II at the discontinuity plane ($z = 0$), can be expressed in terms of the eigenmodes in side I and side II, respectively as follows:

$$E_t^I = E_t^{in} + \sum_{i=0}^{\infty} a_i E_{ti}^I \tag{2.78}$$

$$H_t^I = H_t^{in} - \sum_{i=0}^{\infty} a_i H_{ti}^I \tag{2.79}$$

$$E_t^{II} = \sum_{i=0}^{\infty} b_i E_{ti}^{II} \tag{2.80}$$

$$H_t^{II} = \sum_{i=0}^{\infty} b_i H_{ti}^{II} \tag{2.81}$$

The generated modes at the discontinuity of the plane, may be propagated, radiated or evanescent, and a_i are the amplitudes of the different i^{th} modes from modal field profiles E_{ti}^{I} and H_{ti}^{I} reflected from the junction in side *I* and b_i are the amplitudes of the i^{th} modes transmitted in side II, with their modal electromagnetic field profiles, E_{ti}^{II} , H_{ti}^{II} .

The LSBR method looks for a stationary solution to satisfy the continuity conditions of the tangential fields in a least squares sense by minimising error functional J, $\frac{\partial J}{\partial a_i} = 0$ and $\frac{\partial J}{\partial a_i} = 0$ for i = 1, ...infinity, where:

$$J = \int \left| E_t^I - E_t^{II} \right|^2 + wZ_0^2 \left| H_t^I - H_t^{II} \right|^2 d\Omega \tag{2.81}$$

Where Z_0 is the free-space wave impedance and *w* is a convenient, positive and dimensionless weighting factor, and the integral is calculated over the discontinuity plane. To obtain the approximate numerical solution to the problem, the infinite series expansion of equations (2.78) to (2.81), including all the relevant propagating modes plus as many radiating and/or evanescent modes as is convenient. The minimum criterion of equation (2.81) reduces to the following linear equation:

$$Cx = v \tag{2.82}$$

Here *C* is the square matrix generated from the eigenvectors and υ is an array due to the incident mode. The solution of this equation gives the vector in $\{x\}$ consisting the required modal coefficient a_i and b_i of the reflected and the transmitted modes. These constitute one column of the scattering matrix, corresponding to the chosen incident mode. Vector $\{x\}$ is made up of all the unknown modal amplitudes. The elements of *C* and υ are given by:

$$C_{ij} = \left\langle E_{ti}, E_{tj} \right\rangle + wZ^2 \left\langle H_{ti}, H_{tj} \right\rangle \tag{2.83}$$

$$v_i = \left\langle E_t^{in}, E_{ti} \right\rangle + wZ^2 \left\langle H_t^{in}, H_{ti} \right\rangle \tag{2.84}$$

Where i, j = 1,...,N and N is the total number of modes in side I and II and the vector E_t and H_t are made up of all the corresponding modal fields in both sides. Inner products involved in the above expression are defined similar as equation of (2.44).

2.8 Summary:

The application of the finite element technique according to the variational principle in modal analysis for the variety of the waveguide structures has been discussed in this chapter. A brief properties for the different numerical methods involved in the analysing waveguide

problems also has been mentioned. A detail of mathematical discipline is provided for the **H**-field based FEM formulation.

The characteristic of the scalar and vector formulations, some kind of boundary conditions and shape functions have been also detailed. Since the vector formulation suffer from the appearance of spurious solutions, to employ of the penalty functions aspect was discussed in detail in order to eliminate the non-physical modes.

A rigorously convergent least squares boundary residual method is described for using to analyse the discontinuities in the waveguides. The method is able to calculate the power transfer between two waveguides by utilising of the scattering and transmitting coefficients. The role of the finite element program using of the LSBR technique is also presented followed by the calculation of the insertion loss. The application of this method for optimising and also improvement of the performances in such photonic devices will be presented in the subsequent chapters.

Rigorous Modal Analysis of Silicon Strip Nano-Scale Waveguides

In this chapter, a rigorous **H**-field-based full-vectorial modal analysis is carried out and this is used to characterize, more accurately, the abrupt dielectric discontinuity of a high index contrast optical waveguide. The full vectorial **H**- field vector profiles are described in detail. The single and second mode operation, vector field profiles, modal hybridness, birefringence, and power confinement of this silicon nanowire are also presented.

3.0 Introduction:

Revolution of the electronic technology was only possible due to both miniaturization and also integration of millions of transistors into single VLSI chip. On the other hand, optical communication systems of today rely heavily on hybrid integration of a limited number of relatively larger discrete components like lasers, modulators, multiplexer, detector etc. Similar to the revolution that single chip integration brought to electronics, one way to reduce the cost of optoelectronics, is to make the devices as small as possible and find a material system for monolithic integration of all the components.

Photonic Integrated Circuit (PIC) can improve reliability and reduce the size of most complex systems by using fewer components. However, there has not been a large scale PIC commercially deployed because of the high development cost and poor flexibility associated with the fabrication processes of the monolithically integrated subsystems. One way of reducing the devices size is to use dielectric material with a refractive index as high as possible, which can improve the optical confinement and effectively reduce the waveguide dimensions. High index contrast also allows very small bending radius, which suitable for increasing the number of components on a chip to increase both functionality and reliability of the chip.

When the waveguide dimensions of an optical device are much smaller than the operating wavelength, unique material and structurally-dependent properties can be exploited and recently these have attracted considered attention. Amongst the variety of materials considered so far, silicon has been particularly attractive as the low-cost and mature CMOS fabrication technology developed for the electronics can be exploited. Its high index contrast results a tight modal confinement, allowing efficient scaling and close packing of photonic components. In waveguiding applications, the small size of the silicon core with the silica cladding has allowed the fabrication of quantum wire [124]. Recently the high index contrast in devices with a silicon core and silica or air cladding has initiated a number of studies in the silicon photonics field [125]. As a result, it is expected that high speed opto-electronic silicon-based technology would be a suitable candidate for ultra-high-speed communications [126], slow light devices [127], atomic trapping [128], and sensing applications [129]. It has also been reported that in the sub-wavelength regime, the shape of the waveguide becomes crucial in the determination of the dispersion properties, and also taking advantage of high optical intensities coupled with carefully engineered group-velocity-dispersion (GVD) characteristics [130].

It is the aim of this chapter to present a review in **H**-modal parameter of the Si photonic waveguides. The characterisation of the mode fields of the Si strip with a nanoscale cross-section will be studied and shown in detail. A prototype of the geometry with the core size of the waveguides in Si photonic devices for single mode operation will be illustrated in this chapter. For designing any practical device, a single mode condition plays a very important characteristic, because its reasonable function depends on the fundamental guided modes. Therefore, determining the single mode condition for any specific dimension can be considered and, due to this, birefringence, the hybridness, the effective area and power confinements of the Silicon strip nano-scale waveguides will be investigated, specifically for air-clad waveguides.

3.1 Waveguide structure:

The structure considered here for the rigorous investigation is a typical silicon strip optical waveguide or Silicon photonic wire waveguide. The symmetry of the photonic structure being studied can be exploited elegantly to reduce the degrees of freedom and hence the calculation involved. The idea is that for the given structure and also associated modal field was expected, which indentifying the symmetry and the also continuity of the field components can be considered and applying these to reduce the order of the matrices and this is feasible which determine of the electric and/or magnetic walls boundary conditions. Then for a rectangular waveguide, the structure has an inherent 90° rotational symmetry. If only a half or a quarter of the structure is need to analyze, it can use a finer mesh and obtain better accuracy.

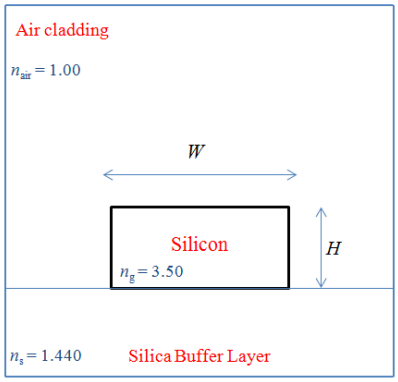

Fig. 3.1 Schematic of a Silicon nanowire waveguide.

The structure considered here for a thorough investigation is a conventional silicon strip optical waveguide or Si photonic wire waveguide. Particular types of waveguide consist of a silicon core with small rectangular cross-section, surrounded by Air. The silicon core can also be buried under a thick SiO_2 layer. The structure can be fabricated by using SOI (Silicon-On-Insulator) wafer on a Si substrate. A resist mask can be used on the surface of the Si layer and the Si waveguide core can be formed by etching down to the SiO_2 buffer layer by use of Inductively Coupled Plasma (ICP) dry etcher. In this study, the thickness of the core waveguide are taken as *H*, that of the lower SiO_2 buffer layer as 1.50 μm and wavelength as 1550 nm. The refractive index of the rectangular Si core at 1.55 μm wavelength is taken as

3.50. The refractive indices for the SiO_2 substrate and air cladding are taken as 1.50 and 1.00, respectively.

3.2 Effective index and Birefringence analysis:

In planar (infinite slab) waveguides, modes can be purely TE or TM. However, in optical waveguides with 2-dimensional confinement the modes are never purely TE or TM and are denoted by quasi-TE or quasi-TM modes. Although scalar formulation based FEM may be sufficient for solving solutions on quasi-TE, quasi-TM or any one dimensional waveguide problems, it is however, inadequate to found solutions for hybride modes of anisotropic or inhomogeneous or any two-dimensional optical waveguide problems. The vectorial based FEM formulation is more appropriate for two-dimensional hybride modes problems. In this study, the **H**-field based VFEM may be used to obtain the modal solutions of such a waveguide structure.

Most of the planar Silicon nanowires are fabricated by using mature CMOS technology that was developed for the semiconductor industries. In this case, commercial wafers are available for a fixed thickness of Silicon guiding layer on a Silicon substrate with a Silica buffer layer. Typically 220 – 400 nm thick Silicon guiding layer are used.

In the simulation carried out, the waveguide heights (H) at 220 nm, 260 nm, 300 nm, 350 nm and 400 nm, while the waveguide width (W) as decreased very slowly from 3 μm to nano-dimensions to determine higher mode transition to the single mode condition. The effective index, n_{eff}, of a given mode is normalized propagation parameter, which can be defined by:

$$n_{eff} = \frac{\beta_0}{k_0} \tag{3.1}$$

Where β_0 is the propagation constant of the mode and k_0 is the free space wavenumber defined as:

$$k = \frac{2\pi}{\lambda} = \omega(\varepsilon_0\mu_0)^{0.5} \tag{3.2}$$

For this research, due to availability of symmetrical waveguide structure, computational discretised using more than twice irregular sized first order triangular elements.

Variations the effective indices for the fundamental quasi-TE (H^y_{11}) and quasi-TM (H^x_{11}) modes with the waveguides width, W, for the Air-cladding are shown in Fig. 3.2. In this case height, H was kept constant at 220 nm. It can be noticed that when the width of the waveguide is large in comparison to the height of the device structure, the waveguide can be support many modes and in that case n_{eff} is closer to the refractive index of the Si waveguide core. It can be also observed that as the waveguide width is reduced, the effective indices values are reduced. Initially it reduces slowly with the width and then rapidly to reach the cut-off points, in $W \approx 360$ nm. This simulation data generated suggest that the single-mode operation occurs when the waveguide width lies approximately between 280 nm to 360 nm when the operating wavelength, λ, is 1550 nm with a height of 220 nm.

When width of waveguide too large, effective index value reaches asymptotically that of an asymmetric silicon slab waveguide of thickness H = 220 nm, with air cladding and silica substrate on two sides.

It is mention that, when width of silicon nanowire waveguide is too small, this waveguide cannot support any mode, effective index value approaches that of the silica index value as most of the power would be in silica substrate.

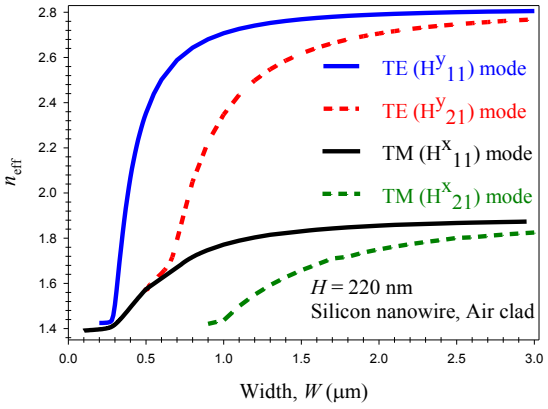

Fig. 3.2 Variation of the effective indices with the waveguide width, W, for the quasi fundamental and second TE (H^y_{11}) and TM (H^x_{11}) modes, in H = 220 nm.

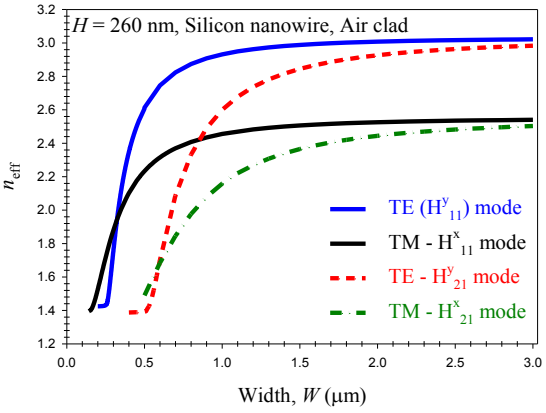

Fig. 3.3 Variation of the effective indices for the quasi-TE (H^y_{11}) and quasi-TM (H^x_{11}) for the first and second modes, with the waveguides width, W, in H = 260 nm.

Next, a higher waveguide thickness is considered in Fig. 3.3. It shows that as waveguides width reduces the effective indices of the quasi-TE (H^y_{11}) and quasi-TM (H^x_{11}) modes also reduces. In this case H = 260 nm, reduction is not striking by the time the waveguide width reaches less than about 0.6 μm and 0.9 μm, for the fundamental and second quasi modes, respectively.

For those regions, all of the effective indices rapidly decrease to achieve a constant value as the cross-over point. It can be also noticed that, at this point, for the fundamental quasi-TE and TM modes, the height of silicon nanowire is nearly equals the waveguide width. Also, it is shown in here that when the dimension of the waveguide's width is smaller than height, the quasi-TM effective index is higher than the quasi-TE mode.

It is found that when the height of the waveguide is large, the quasi-TM (H_{11}^x) mode is more dominant. Comparing Fig. 3.4 with Figs. 3.2, and 3.3, it can be noticed that as the height is increased, the effective indices for quasi-TE (H^y_{11}) mode and quasi-TM (H^x_{11}) mode are bigger and also, the larger the height is, the larger cross point value is. These values for the quasi fundamental TM (H^x_{11}) and the second quasi- TE (H^y_{11}) modes are calculated as 525 nm, 745 nm, and 858 nm for H = 220 nm, H = 260 nm and H = 300 nm, respectively.

Finally, the Fig. 3.4 shows the effective indices for quasi-TE (H^y_{11}) and quasi-TM (H^x_{11}) modes by reduction of waveguide width when H = 300 nm.

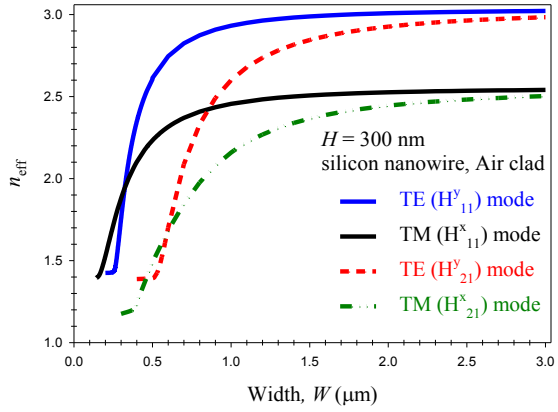

Fig. 3.4 Variations of the effective indices for the first and second quasi TE and TM modes with the waveguides width, W, when H = 300 nm.

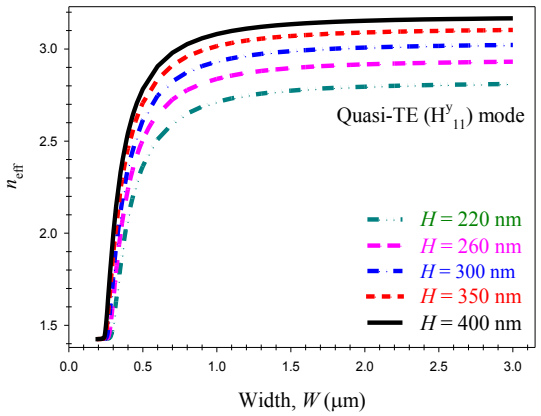

Fig. 3.5 Variations of the effective indices, n_{eff}, of the fundamental quasi-TE (H^y_{11}) mode, with the waveguides width, W, for different Heights.

The variations of effective indices with the change of width from 3.5 μm to nano-dimensions for the fundamental quasi-TE (H^y_{11}) mode are shown in Fig. 3.5 for the waveguides heights, 220 nm, 260 nm, 300 nm, 350 nm, and 400 nm. It can be observed that, the difference between the effective indices of the quasi-TE (H^y_{11}) mode for different height are almost the same. The effective index of quasi-TE mode for the waveguide height 400 nm is about 3.167 with the waveguide width of 3.0 μm, while the value reduces for the same waveguide width to 2.805 with silicon nanowire waveguide height equal to 220 nm. It is shown that the increase in waveguide heights leads to the decrease in the shape of trend. It can also be noted that when H = 220 nm, it reaches its cut-off state for the fundamental mode earlier than the other heights and that the cut-off width is at between 240 nm to 280 nm.

The variations of effective indices for the fundamental quasi-TM (H^x_{11}) mode with the waveguides width, W and different heights are shown in Fig. 3.6. If they are compared, as a difference between effective indices for quasi-TM (H^X_{11}) mode for same waveguide heights as quasi-TE (H^{y11}) mode, it can be find out that the effective indices for quasi-TE modes are much more than their asymmetric quasi-TM modes for waveguides heights. For example, effective index for quasi-TE mode for waveguide height of 400 nm is 3.167, while this value is 2.945 for quasi-TM mode in the same waveguide height. It can also be observed that the variation of effective indices for quasi-TM (H^X_{11}) modes with different waveguides height are not the same, compare to variation of quasi-TE (H^y_{11}) mode in the same waveguide height.

When it comes to cut-off condition value, its values increasing in fundamental quasi-TE (H^y_{11}) mode compared to quasi-TM (H^x_{11}) mode for the same waveguide heights. The cut-off width is around between 120 nm to 270 nm.

Figure 3.7 shows the variations of the modal birefringence with the change of width, for the waveguide heights, 220 nm, 260 nm, 300 nm, 350 nm and 400 nm.

The modal birefringence is determined as difference between the effective indices of the fundamental quasi-TE (H^y_{11}) and quasi-TM (H^x_{11}) modes.

In the design of photonic integrated circuit (PIC), for this case, silicon nanowire waveguide surrounded by air.

It is shown here that modal birefringence increases as W increase and then saturates. This figure shows that when the width is large as in the case of width, W = 3.0 µm, the modal birefringence is at 0.94 for height equal to 220 nm and for the case of when H = 400 nm, the modal birefringence for the W = 3.0 µm is 0.22.

It can be noticed that the birefringence values are decreasing as the width of waveguides are decreasing. Also, this figure shows that, the high modal birefringence related to the smaller waveguide height as H = 220 nm, because the difference between effective indices for the quasi-TE (H^y_{11}) and quasi-TM (H^x_{11}) modes compare to another silicon nanowires waveguide is high.

It can be noted that for the different waveguide heights, if it refer to birefringence zero zone, the waveguides have a specific values, respect to the width of waveguides. These values are taken 0.41 µm, 0.37 µm, 0.32 µm, 0.29 µm and 0.27µm for H = 400 nm, H = 350 nm, H = 300 nm, H = 260 nm and H = 220 nm respectively.

It can be described that for width beyond 500 nm, modal birefringence will be large when H is reduced but the width for zero birefringence will be small. It is also shown here that the birefringence is zero when the waveguides width and height are of similar values.

It can be also observed that modal birefringence is negative when the width of the waveguide is reduced to the nano-scale, because in these cases, the fundamental quasi-TM (H^x_{11}) mode becomes dominant.

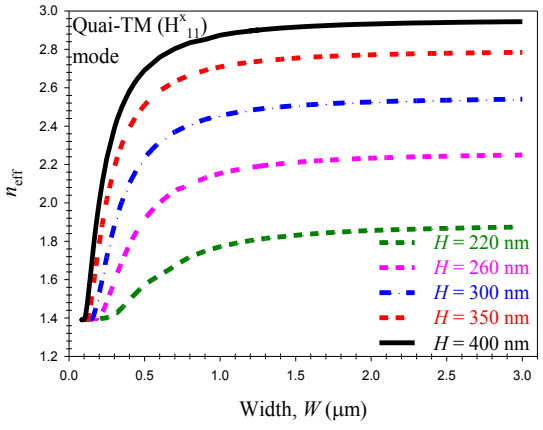

Fig. 3.6 Variations of the effective indices, n_{eff} of the quasi- TM (H^x_{11}) mode, with the waveguide width, W, for different H.

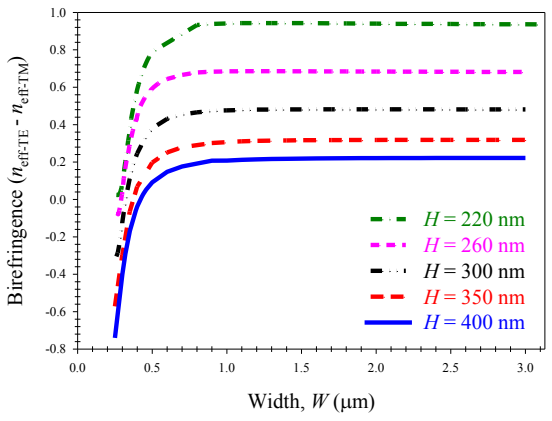

Fig. 3.7 Variations of the modal birefringence with the width, W, for different Height in a Silicon nanowire waveguide.

3.3 Analysis of modal H-field profiles:

In the analysis of modal H-field profiles, for the Air clad, quasi-TE (H^{y}_{11}) mode, the H_y field component is dominant, and H_x and H_z are the non-dominant components.

Also, for the quasi-TM (H^{x}_{11}) mode, H_y and H_z are the non-dominant components, while the H_x field component is dominant.

The dominant H_y field component of the H^{y}_{11} mode is shown as an inset in Fig. 3.8 for the waveguide width, $W = 0.30$ µm, when height of the waveguide is kept in 220 nm.

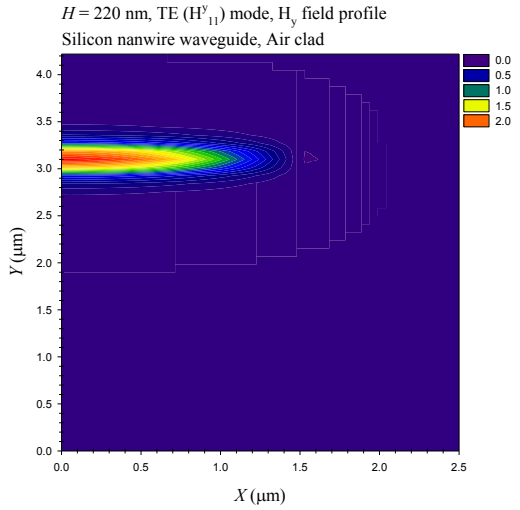

Fig. 3.8 Dominant H_y field profile of the H^{y}_{11} mode.

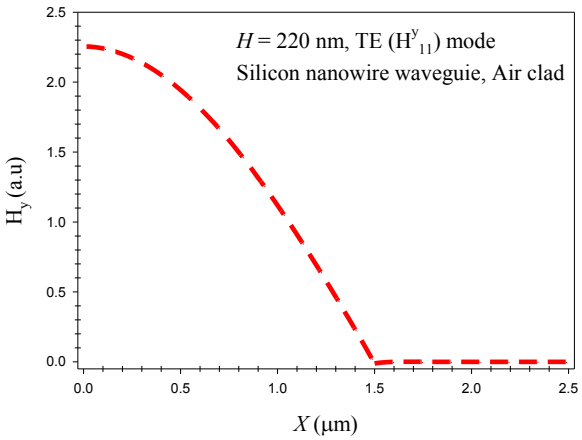

Fig. 3.9 Variation of the H_y field for the quasi-TE (H^{y}_{11}) mode, along X-axis.

The field profile shown in Fig. 3.8 clearly identifies the maximum intensity occurring at the centre of the core. It is also shown that there is symmetry along the axes. It can be noticed that, the mode can be extended into the cladding and substrate, Air and SiO_2 regions, respectively.

To illustrate its variation more clearly, the variation of the H_y field along the waveguide width is also shown in Figure. 3.9.

The H_y field is monotonically decreasing rapidly along the X-axis, and at the boundary between the core and cladding (Si/Air), the magnitude of the H_y field is zero.

In the contour plot is clearly visible that the modal confinement in the horizontal direction is much stronger. The n_{eff}, of the quasi-TE (H^{y}_{11}) mode was found to be 2.8104, when $H = 220$ nm.

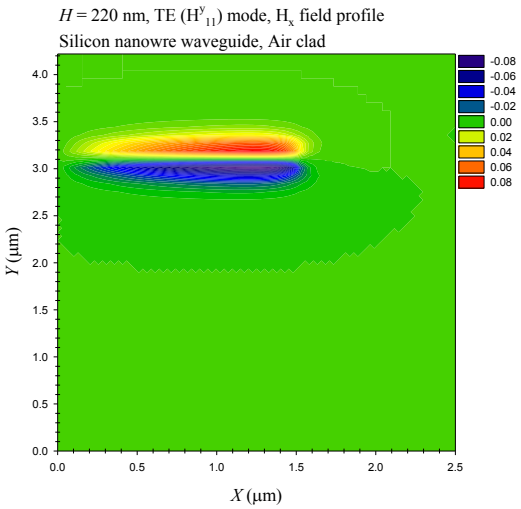

Fig. 3.10 Non-dominant H_x field profile of the H^y_{11} mode.

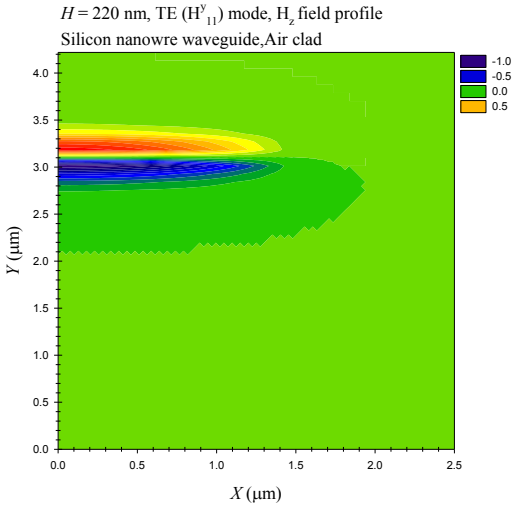

Fig. 3.11 Non-dominant H_z field profile of the quasi-TE (H^y_{11}) mode.

For the quasi-TE (H^y_{11}) mode, H_x field component is non-dominant. In contour plot shown in Fig. 3.10. It is found that when $W = 0.3$ µm, and $H = 220$ nm. In contour plot shown in Fig. 3.10, it is clearly visible that the H_x field modal confinement is much stronger, and it spreads more in the horizontal direction, resulting in a dumbbell-shaped profile.

The contour of non-dominant H_z field component of the quasi-TE (H^y_{11}) mode is shown in Fig. 3.11 that when $W = 0.3$ µm and $H = 220$ nm. It can be observed that the maximum intensity occurs at the two horizontal interfaces between the Si and SiO_2. This because the value of H_z is proportional to the derivate $^{\partial E_x}/_{\partial y}$ and therefore the H_z value is shown to peak in the y-direction.

For the quasi-TM (H^x_{11}) mode, the H_x field component is dominant, and H_y and H_z are the non-dominant components.

In the analysis of modal **H**-field profiles, for the Air clad, H_x field component of the H^x_{11} mode is shown as in Fig. 3.12 for the waveguide width, $W = 260$ nm, and height, $H = 260$ nm. The field profile shown in Fig. 3.12 clearly identifies the maximum intensity occurring at the centre of the core.

To illustrate its variation more clearly, the variation of the H_x field along the X-axis is also shown in Fig. 3.13. In this case, the H_x field is monotonically decreasing with a rapid reduction along the X-axis and when $X = 0.13$ µm (as H = 260 nm), at the boundary between the Si and Air, the magnitude of the H_x field is 61 % of its maximum value.

In the contour plot it is clearly visible that the modal confinement in the horizontal direction is much stronger. The n_{eff} of the H^x_{11} mode was found to be 1.50148 when $W = 260$ nm.

The non-dominant H_y field component of H^x_{11} mode shown in Fig. 3.14. It has a maximum intensity at the centre of the core. It is also shown that there is symmetry along the vertical

and horizontal axes. As a high index contrast Si waveguide, the non-dominant H_y field component of H^x_{11} mode has a significant magnitude, which is shown in Fig. 3.15. In the case where H = 260 nm and W = 260 nm, the maximum magnitude of H_y field is found to be 12 % of maximum H_x field.

The contour of non-dominant H_z field component of the H^x_{11} mode is shown as in Fig. 3.16. It can be observed that the maximum intensity occurring at the centre of the core.

From the Fig. 3.17, the maximum magnitude of H_z is found to be 40 % of the maximum H_x field and it is significantly higher than the non-dominant of H_y field amplitude. The H_z field is zero along the X-axis.

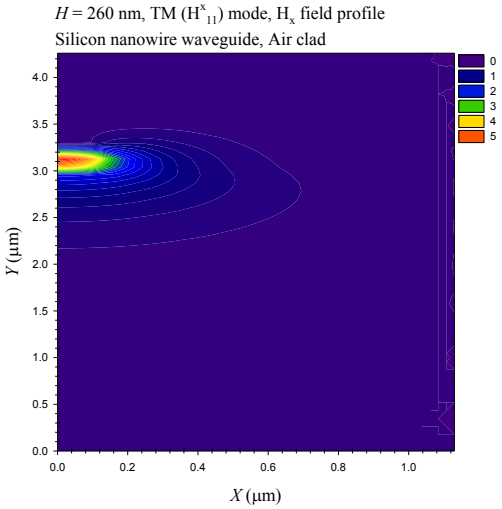

Fig. 3.12 Dominant H_x field profile of the quasi-TM (H^x_{11}) mode.

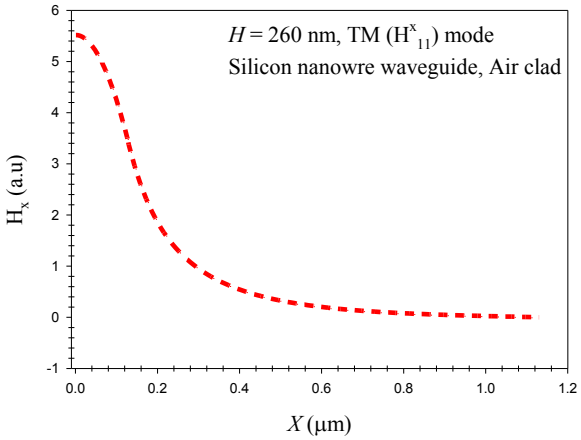

Fig. 3.13 Variation of H_x field along X-axis in Air clad Silicon nanowire for the quasi-TM (H^x_{11}) mode.

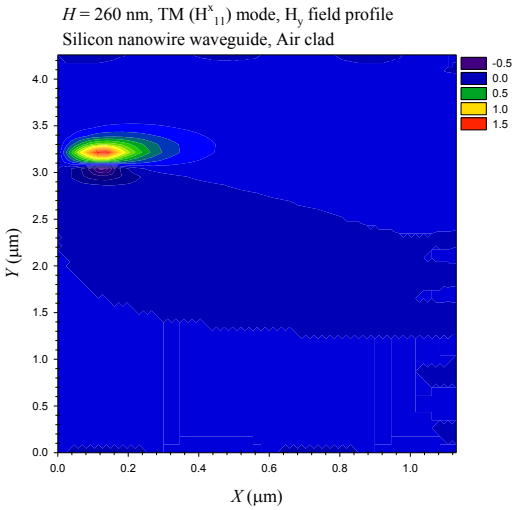

Fig. 3.14 H_y field profile of the quasi-TM (H^x_{11}) mode.

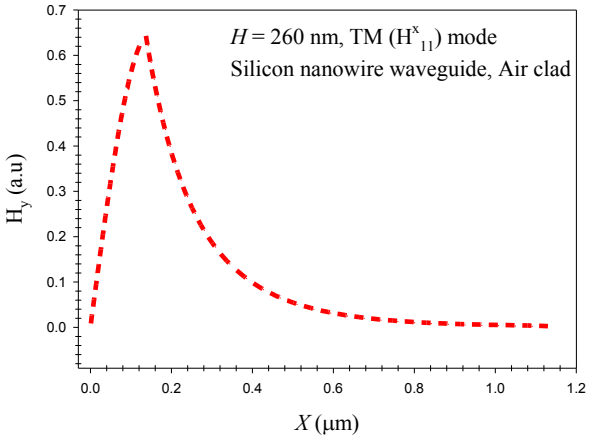

Fig. 3.15 Variation of H_y field along X-axis, in Air clad Silicon nanowire for the quasi-TM (H^x_{11}) mode.

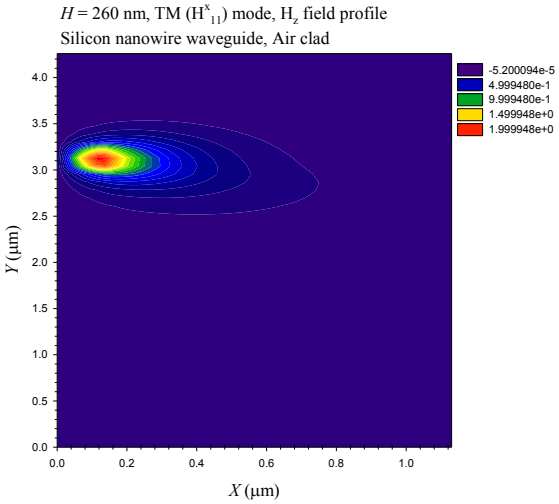

Fig. 3.16 H_z field profile of the quasi-TM (H^x_{11}) mode.

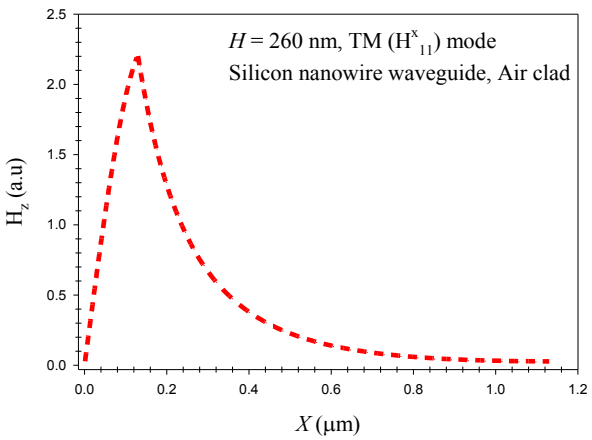

Fig. 3.17 Variation of H_z field along *X*-axis, in Air clad Silicon nanowire for the quasi-TM (H^x_{11}) mode.

3.4 Hybridism analysing:

Pure TE and TM modes can only exist in planar slab waveguides with 1-dimensional confinement. However, in all optical waveguides with 2-dimensional confinement, the modes are classified as quasi-TE and quasi-TM modes, which contain all the six components of the **E** and **H** fields. Besides that, in the high index contrast Silicon nanowires, the modal hybridness is much higher. To find all the three components of the **H**-field and the evolution of fully hybrid quasi-TE and quasi-TM modes along a guided-wave device all the methods to be used must be fully vectorial in nature. It is mentioned that, the modal hybridness defined as the ratio of the maximum value of the non-dominant H_x and / or H_z field components to the maximum value of the dominant in H_y modal field component. Modal hybridness is a key property in polarization issues. This parameter can be used to calculate polarization cross-talk [7] and also in the design of polarization rotator or polarization mode dispersion.

The variations of the modal **H**-field and the hybridness with the waveguide width in nanometer scale for the H = 220 nm in fundamental quasi-TE (H^y_{11}) mode will be analysed in this section.

Variation of its maximum value with the width is shown in Fig. 3.18, the reduction of waveguide width is followed by the steady increase in the maximum value of dominant H_y field to a maximum point of about 6.138, at W = 0.34 μm. Then its maximum value drops rapidly to less than 1 when the waveguide width reduces further and approaches cut-off value.

The normalisation of the eigenvector is carried out by the solver and related to the power of the mode. In this case when the spot-size was smaller, magnitude of the dominant field was higher. For the quasi-TE (H^y_{11}) mode the H_y field component is dominant and other components H_x, and H_z are non-dominants.

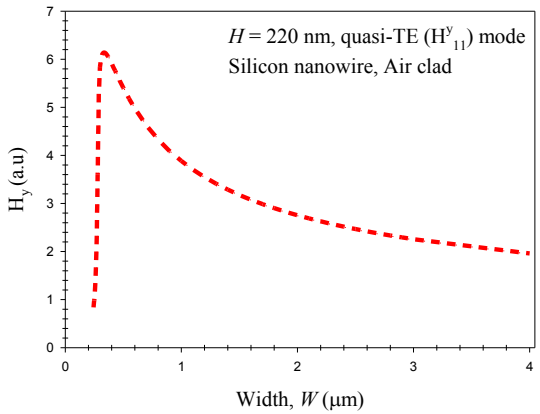

Fig. 3.18 Variation of the maximum H_y field with the width, W, for the quasi-TE (H^y_{11}) mode in $H = 220$ nm.

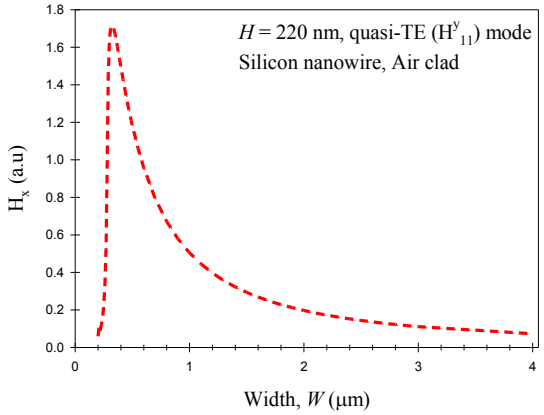

Fig. 3.19 Variation of the maximum H_x field with the width, W, in Air clad silicon nanowire for the quasi-TE (H^y_{11}) mode.

Variation of the maximum H_x modal field with the waveguide width, W, for the quasi-TE (H^y_{11}) mode in $H = 220$ nm is shown in Fig. 3.19. A low maximum amplitude can be observed for a wider waveguide in clearly, however as W is reduced, maximum H_x field reaches a peak value, then rapidly reduces as the fundamental quasi-TE mode approaches its cut-off region. The maximum value for the H_x non-dominant field is found to be 1.716 at $W = 320$ μm.

The variations of the maximum H_z field with the waveguide width, W is also shown, when $H = 200$ nm, in Fig. 3.20, which increases monotonically but with a rapid reduction from the $W = 0.33$ μm. The maximum magnitude of H_z is found to be 45 % of the maximum H_y field and it is higher than that the non-dominant of H_x field. It can also be noted that all the three **H**-field components of the quasi-TE (H^y_{11}) mode are continuous across the junction core and the clad.

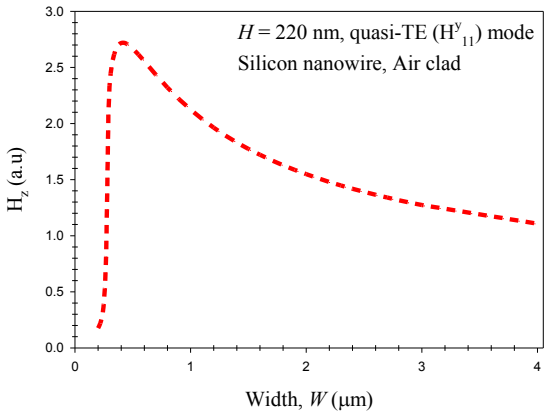

Fig. 3.20 Variation of maximum H_z field with the width, W, in Air clad Silicon nanowire for the quasi-TE (H^y_{11}) mode.

The variation of the modal hybridness with the width for the quasi-TE (H^y_{11}) mode is shown in Fig. 3.21. The modal hybridness, in this case is defined as the ratio of the maximum value of non-dominant H_x field to the maximum value of dominant H_y field. It is shown in here that when *W* is small, hybridness will reach a higher maximum value as in the case when *H* = 220 nm. It is also shown that as *W* reduces, the hybridness increases until it reaches its maximum value as in 0.28 at the *W* = 320 nm, and then starts to reduce as it approaches to its cut-off.

For the other non-dominant H_z field, the hybridness can also be defined as the ratio of H_z / H_y, and this parameter a function of the width, is shown in Fig. 3.22. It can be observed that the hybridness increase slightly as the width increases. It is also shown that the H_z , hybridness of the fundamental H^y_{11} mode is significantly larger than its H_x hybridness.

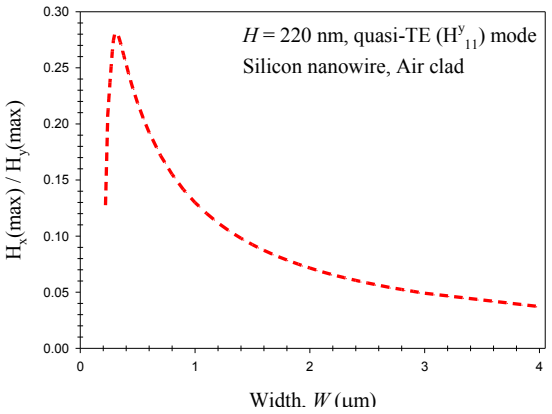

Fig. 3.21 Variation of H_y hybridness with the width, *W,* in Air clad Silicon nanowire for the quasi-TE (H^y_{11}) mode.

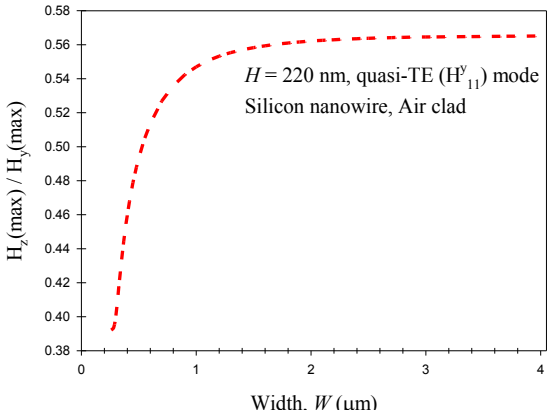

Figure. 3.22 Variation of the H_z hybridness with the width, *W*, in Air clad silicon nanowire for the quasi-TE (H^y_{11}) mode.

The variation of the field component ratio with the waveguide width, *W*, for the different height of the waveguides is shown in Fig. 3.23. From the figure, it can be clearly seen that the hybrid nature is enhanced by reducing the waveguide width, *W*. When *H* = 220 nm, hybridness is shown by a blue solid line, reaches its maximum, then rapidly reduces as the fundamental mode approaches its cut-off region.

The maximum hybridness for the fundamental 220 nm height is found to be 0.2815 at *W* = 311 nm. Furthermore, the behaviour for the higher waveguides are shown to be similar to that of the *H* = 220 nm, in which, as the width decreases, the hybridness increases until each higher height of the waveguides approaches its cut-off regions. It can be observed that if the width is reduced further, the waveguide cannot support a guided mode.

For the non-dominant H_z field, the hybridness can also be defined as the ratio of Hz / Hy, and this parameter is a function of the width, is shown in Fig. 3.24.

It can be observed that the hybridness increases as the width increases. It is also shown that the H_z hybridness of the smallest height is significantly larger than the other heights. The H_z

hybridness of the different heights follows a similar behaviour, in which, they all decreases as width decreases.

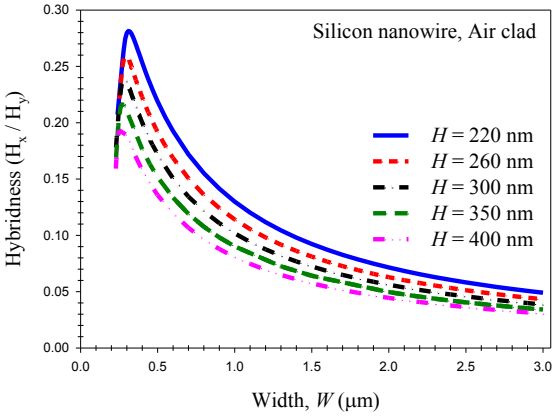

Fig. 3.23 Variations of H_y hybridness with the width, W for the quasi-TE (H^y_{11}) mode.

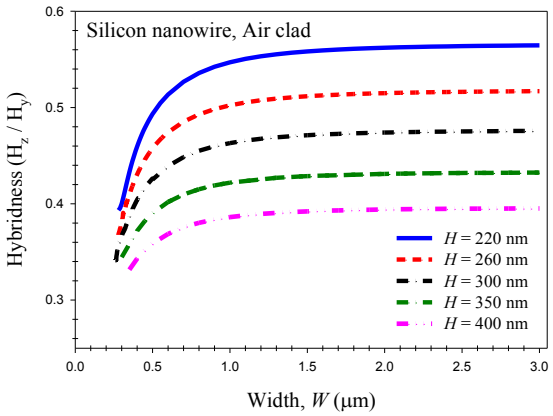

Fig. 3.24 Variations of H_z hybridness with the waveguide width, W for the fundamental H^y_{11}mode.

3.5 Analysis of optimum parameters in silicon nanowire waveguide:

In the design of PIC, some silicon guided wave components may be surrounded by air, which the variations of their effective indices and also the effective areas with the width are rigorously investigated. Here the air-clad structure has only got one-fold symmetry, so half of the waveguide is used in the simulation.

For various applications, the mode size or its effective area is an important modal parameter. Here, following the second moment of the intensity distribution recommended by ISO Standard 11146, the effective area (A_{eff}) is used to evaluate this area [131] can be given by:

$$A_{eff} = \frac{(\iint_{\Omega} |E_t|^2 \, dx \, dy)^2}{\iint_{\Omega} |E_t|^4 \, dx \, dy} \tag{3.3}$$

Figure 3.25 shows the variation of the effective index and also the effective area with the waveguide width for the quasi-TE (H^y_{11}) mode. In this case the height was kept constant at 220 nm. It can be observed that as width reduces, effective area reduces slowly reaches a minimum value of 0.16 μm^2 at W = 0.36 μm, then increases rapidly as mode approaches its cut off.

Variations of the effective indices and effective areas for the fundamental quasi-TE (H^y_{11}) and fundamental quasi TM (H^x_{11}) modes are shown in Fig. 3.26. In this case height, H, was kept constant at 220 nm. The striking feature is that the effective index for fundamental quasi TE (H^y_{11}) mode is larger than that of the fundamental quasi TM (H^x_{11}) mode. However when the waveguides width, W, becomes smaller, the trends for these two cases are almost similar.

When it comes to effective area for quasi –TE and quasi-TM modes, we can see that the both of them reduce as the width reduces. Generally, about the cut-off region for the quasi-TE mode and TM mode both effective area increases rapidly.

The effective indices and effective areas of the fundamental quasi-TE (H^y_{11}) mode and quasi-TM (H^x_{11}) mode for the waveguide height equal 260 nm are varied with respect to the width of waveguide.

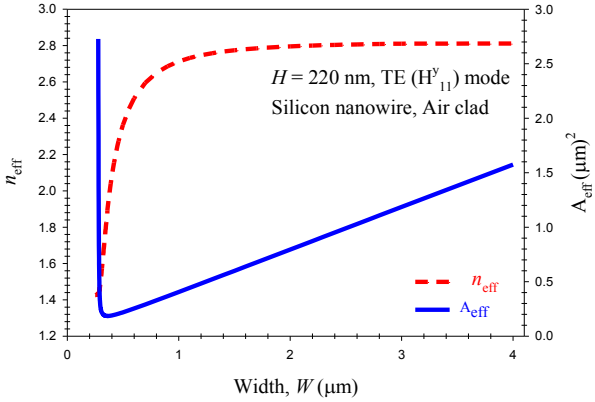

Fig. 3.25 Variations of the n_e and A_{eff} with the width, W, for the quasi-TE (H^y_{11}) mode.

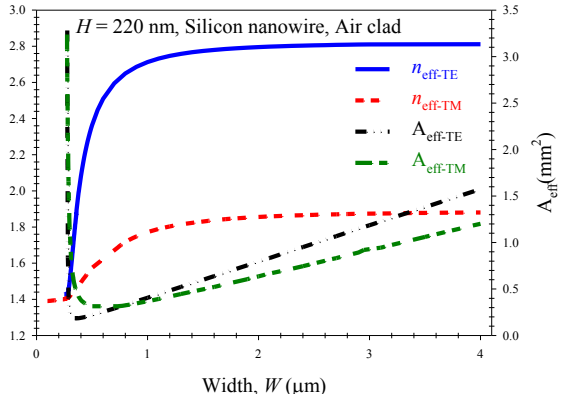

Fig. 3.26 Variation of effective indices and effective areas for the quasi-TE (H^y_{11}) mode and quasi-TM (H^x_{11}) modes with the width.

According to the Fig. 3.27, the effective index and effective area for the quasi TE mode is larger than effective index and effective area for quasi TM mode, but when the width of a gets smaller the difference between the effective indices becomes smaller. This difference reaches to almost zero, when the waveguide width has nearly 0.23 μm as cross point.

Effective area for quasi-TE and quasi-TM mode then expands rapidly, when the waveguide width reaches to the lowest value, which is the cut-off point.

The variations of the power confinement with the width, W, are shown in Fig. 3.28 for the quasi-TE (H^y_{11}) mode in different heights of the waveguide.

The confinement factor in any particular area normalized to the total power, which is obtained by integrating the Poynting vector, from the **H**- and **E**- fields as given below:

$$S_z = \iint_{\Omega} \{\boldsymbol{E}^* \times \boldsymbol{H}\}_z \, dx \, dy \tag{3.4}$$

It is expected that as the waveguide dimension becomes large, most of the power would be confined in the Si core and that, Γ_{Si} would be close to 1.0. However, it can be noted that, the maximum power confinement in this case is closer to 0.895, because the height of the core was restricted to 300 nm.

If the height of the core also becomes larger, then the power confinement in the Si core could approach 1.0. It can be observed here that as the width is reduced, the power confinement in the Si core also reduces. It can be also observed that although, for a wider waveguide, the power confinement for all height of the waveguides almost similar, but for a narrower waveguide, say $H = 220$ nm, the power confinements is smaller.

The variations of the effective index, n_{eff}, the effective area, A_{eff} and the power confinement in the Air cladding region, Γ_{SiO2}, with the width, W, of the fundamental H^y_{11} mode are shown together in Fig. 3.29, for their comparison. It can be observed that for the single mode operation in the case of a 220 nm thick waveguide, the value of the width should lie between 280 nm and 400 nm and this may chosen optimally to be around 360 nm, when the spot-size is also the smallest about 0.077. In this case, the power confinement in SiO_2 is 0.18 and remaining power will be stored in Si core. From this figure, it can be seen that the power confinement range in SiO_2 for the single mode operation for the single mode operation range could be between 0.86 and 0.15 for those width values varying from 280 nm to 400 nm.

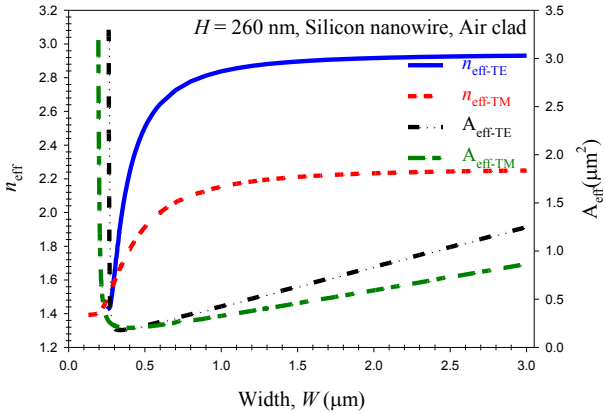

Fig. 3.27 Variations of the effective indices and effective areas of the quasi-TE and TM modes, with width, when $H = 260$ nm.

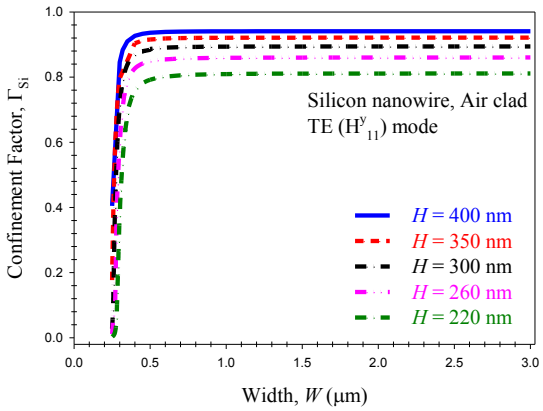

Fig. 3.28 Variations of power confinement factor in silicon nanowire, Γ_{Si}, with the waveguide width, W, for the different height.

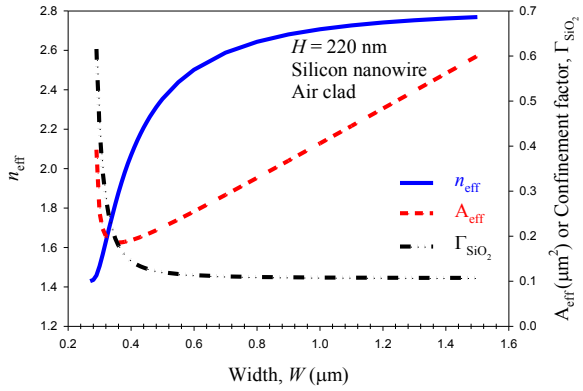

Fig. 3.29 Variation of n_{eff}, A_{eff} and Γ_{SiO2} with the waveguide width, W, for the fundamental H^y_{11} mode, when $H = 220$ nm.

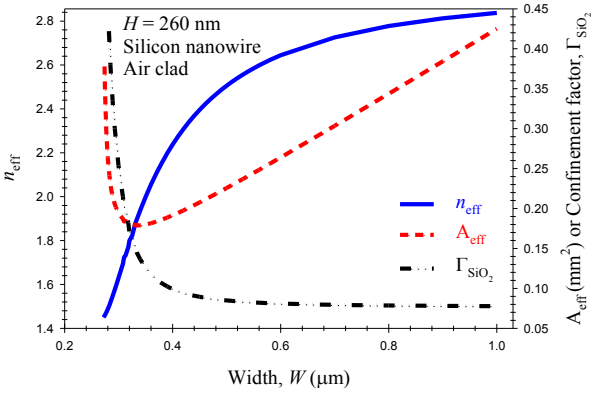

Fig. 3.30 Variation of the n_{eff}, A_{eff} and Γ_{SiO2} with the waveguide width, W, for the quasi-TE (H^y_{11}) mode, when $H = 260$ nm.

In Fig. 3.30 investigating the condition for selecting the range of the single mode operation, in the case of H = 260 nm thick is considered. To obtain the optimum region in Fig. 3.30, the variation of the effective index, power confinement in the SiO_2 and also, effective area with the waveguide width in quasi-TE (H^y_{11}) mode are studied as a comparison. It can be observed that, in the single- mode region, the value of the spot- size reaches to its smallest value about 0.18. This region in term of the waveguide width is selected between 280 nm and 380 nm, which optimal point can be chosen about 335 nm, when the power confinement in the substrate is 0.14 and the remaining power is loaded to the Si core, which corresponding in the single mode region, those values for power confinement in the core is varied between 0.35 and 0.82, respectively.

3.6 Summary:

There is an impetus to develop low-cost photonic devices that can be furthered by exploiting the well-developed, low-cost CMOS technology. The higher index contrast, Δn, of silicon also allows for smaller waveguides and compact bend designs which will allow more reliable PIC to be developed, with increased functionality.

It is shown here that for a silicon waveguide with a strong index contrast, the single mode operation region is 280 nm to 400 nm, when the waveguide height is varied from 220 nm to 260 nm and the operating wavelength is 1550 nm. It is also shown here that, for the case of H = 220 nm, the effective area not only is minimum, when $W \approx$ 360 nm, but also these values are similar for both the polarizations. In this case, the modal birefringence is also small and spotsize is near circular and could be a suitable dimension for many applications.

It has also been shown here that the modes in such nanowires with a strong index contrast are not pure-TE or TM modes, but have very high non-dominant components. It should be noted that the performance of these highly birefringence guided-wave devices are polarization dependent. The existence of higher non-dominant components may have a strong effect on the polarization crosstalk in these devices, particularly in the presence of any manufacturing deformity which may be introduced.

On the other hand, the existence of larger longitudinal field components can also be exploited for various novel applications, such as beam shaping or atom trapping. The work has revealed that the dispersion properties can be strongly controlled when the waveguide dimensions are small, for various linear and nonlinear applications.

It has been shown that for a silicon wire waveguide with the nano dimensions, the electric and magnetic fields are fully vectorial and all the six components are demonstrated here. Therefore, to obtain the modal solutions of the waveguides, it is essential to employ a fully-vectorial formulation.

It also has been investigated that the **H**-field components are continuous across the dielectric interfaces, but, for the **E**-field components impossible. It should be noted that if, instead of the **H**-field formulation, an **E**-field formulation is used, this may wrongly force the continuity of the **E**-field across the dielectric interface and introduce a significant error,

particularly for a high birefringence of the silicon nano-wire waveguide. Hence, an **E**-field based formulation would also not suitable, unless an additional integral is incorporated at the interfaces, which may be tedious if this interface has an arbitrary profile, as in the case of a nanowire.

In this study, the spatial variations of all components of the **H**-fields are shown. The modal hybridness, the power confinement and the modal birefringence for the Air-clad Si nanowires are also shown here. However, in the presence of slanted side walls and bends, there may be additional polarization conversion that occurs due to the presence of higher magnitude of the nondominant field components and this can only be studied by using a rigorous full-vectorial approach, as was done in this work.

Design of a Compact Polarization Rotator Using Simple Silicon Nanowires

4.0 Introduction:

Revolution of electronic technology was only possible due to miniaturization and the integration of millions of transistors into a single VLSI chip. On the other hand, unlike highly developed, low-cost, user-friendly electronic goods, optical communication systems of today rely heavily on hybrid integration of a limited number of relatively larger discrete components such as lasers, modulators, multiplexers, detectors, etc. Similar to the revolution that single chip integration brought to electronics, one way to reduce the cost of optoelectronics is to make the devices as small as possible and to find a material system for monolithic integration of all the components.

Photonic integrated circuit (PIC) can improve reliability and reduce the size of a complex device by using fewer components. However, so far there has not been a large-scale PIC commercially deployed because of high development cost and poor flexibility associated with the fabrication processes of the monolithically integrated subsystems. One way of reducing the device size is to use dielectric material with a refractive index as high as possible, which can improve the optical confinement and effectively reduce waveguide (WG) dimensions. High index contrast also allows for a small bending radius, which is suitable for increasing the number of components on a chip to increase its functionality and reliability of the chip.

Silicon (Si) is the most mature material for electronics but a relatively newer material for photonics. The expensive compound semiconductor materials, such as GaAs or InP, can provide light sources, but their low yield coupled with higher assembly and packaging costs has kept optical communication a costly technology. Recently, it has been suggested [132], [133], that silicon-on-insulator (SOI) technology can be considered to be a material choice for designing, and also, has great potential as a platform for the integration dense PIC and Optoelectronic Integrated Circuits (OEIC) devices. However, the high index difference between silicon (Si) core layer and silicon dioxide (SiO_2) cladding layer of SOI induces strong birefringence, leading to some drawbacks. Telecommunication industry embraces for a higher optical transmission network, and the importance of minimizing the unexpected polarization rotation and polarization crosstalk (CT) to compensate the polarization mode dispersion (PMD) in the optical transmission network, and polarization dependent loss, which limit their applications in optical communication, where polarization independent characteristic is commonly required. Thus many solutions are proposed to overcome the issue, including the polarization independent waveguide, the polarizer and the polarization diversity system.

It is well known that modes in optical WGs with 2D confinement are hybrid in nature, with all six components of their **E** and **H** fields being present. Circularly symmetric optical fibre cannot maintain its polarization state as a signal travels through bends, stressed sections, or some small irregularities.

As a result, light input to an integrated optical chip can be randomly polarized. This polarization of light has a significant impact on photonic circuit design and operation. Therefore, it is desirable to have a fixed degree of polarization state, such as a transverse electric (TE) or transverse magnetic (TM) polarization, and it may be necessary to rotate an incoming polarization state by incorporating a polarization splitter and polarization rotator (PR), in a compact system as a polarization diversity [134], [135], [136].

The polarization diversity system consists of integrates the polarization splitter, the polarization rotator (PR) and the signal processing component together. In such system, the input light with arbitrary polarization state is first split into two orthogonal polarization states, which travel in separate arms. After rotating first and then passing through photonic structures in one arm, while in the other arm passing through the same photonic structures first and then rotating, the two polarized beams are combined by a polarization combiner at the output of the chip [137], [138].

It has been reported that polarization rotation can be achieved by exploiting the electro-optic effect in $LiNbO_3$ [139] and InP [140]. However, it was also suggested that a passive polarization converter [141] would be preferable because it would be much simpler to fabricate and to process. Earlier passive polarization converters based on the use of asymmetrically periodic loaded [142]. Then Tzolov [136] proposed the concept of rotation coefficient R, and improved the periodic structure to non-periodic structure, which simplifies the design and fabrication process. Cascaded [143] WGs also have been reported, but such converter has a relatively large device length. To minimize the device length and to reduce the excess loss, a single-section passive PR [144] has been suggested, but it may require a complicated fabrication process often due to its tilting [145] or slanting sidewalls [146,147], or with an asymmetric notch [148].

Up to now, various polarization rotators have been proposed and most of them realized in experiment, including bend waveguides [149,150], slanted-angle waveguides [136,151,152], double-core waveguides [153,154], multi-etch waveguides [155, 156, 157, 158, 159], single/double trench waveguides [160, 161, 162, 163], triangle waveguides [164], and adiabatic tapered waveguides [165,166].

The material platform has extended from III–V compounds to Silicon, which is more suitable for high-density integration and high yield due to the high-index-contrast and the complementary metal–oxide-semiconductor (CMOS) compatible fabrication process.

The design asymmetric waveguide could be obtained from either to change the material or structure of the waveguides. As to the SOI platform, the symmetry could be broken by using asymmetric waveguide structure, such as triangle and irregular polygon, and by introducing material different from SiO_2 to be the upper cladding, such as air and Si_3N_4. Based on this principle, there have been many types of polarization rotators, such as slanted cores [136,151], multi-cores [153, 154] and partially-etched cores [155, 156, 157]. However, the fabrication processes of the above mentioned PRs are complex, either requiring wet etch process or multi-etch process.

In order to simplify the fabrication process, PRs with single/double trench [160, 1561] or tapered waveguide [167, 168, 169, 170] were proposed, which needs only one-mask lithography [171]. The PR with single/double trench utilizes the reactive ion etch (RIE) lag phenomenon, that is, different width trenches correspond to different etch rates in the RIE process when the trench is just tens of nanometers in width. But the trench width and depth must satisfy certain conditions, thereby increasing the design and fabrication difficulty. For the PR based on the tapered waveguide, the mode conversion of the channel waveguides happens between the TM fundamental mode and the higher-order TE modes, requiring an additional structure to separate the fundamental and higher-order TE modes, such as directional coupler [168] or multi-mode interference coupler [170]. In addition, PRs between different types of waveguide provide significant performance [158, 159], just several micrometers long with high extinction ratio, but the fabrication process is complex, difficult to be realized.

Silicon on insulator (SOI) – based nano sized compact slot optical WG has assumed importance due to its potential applications [171]. Due to high index contrast at the interface, transverse electric field shows a very high discontinuity at the interface with very high optical confinement inside the low index slot region when the transverse dimension of the slot is less than the characteristics decay length of that electric field [171], [172], [173]. Though the slot and strip WG dimensions are small but they are highly polarization sensitive. However, for polarization diversity system, this problem can be sorted out by incorporating polarization splitter and polarization rotator/convertor.

Recently, PR made of horizontal slot and strip waveguide (WG) has been reported based on mode evolution [174]. Its fabrication is not easy as the required control of tapered structure is relatively difficult to realize. Moreover, it can rotate only one polarization state for one input direction. Simpler PR by using vertical slots guides have also been reported [175, 176, 177]. Three WGs-based polarization splitter and rotator have also been reported [178].

Another approach is made for this TE-TM conversion based on 2-D photonic crystal slab WG [179]. In this case, though the conversion has been good, but the structure itself is complicated. Researchers have also tried to implement TE to TM convertor by increasing the polarization crosstalk in μ-bend Si WG [180] or bent guide with slanted side wall [181]. Here the conversion efficiency is high though very sensitive to issues like bend loss, slant angle, smooth wall of the WG around bent region etc.

The Si polarization rotator proposed here shows a very compact design without slanted side wall or bent. In this paper, design optimization of a Si polarization rotator based on SOI technology is presented which requires less complex fabrication process with single mask only and compatible with the mature CMOS technology which is backed by a well-established semiconductor industry.

The conversion of one polarized mode to the orthogonal polarized mode is realized by efficient power coupling between these two polarized modes at the phase matching or

resonance condition. The Si polarization rotator reported here has a relatively small footprint and has very low loss compared with the other polarization rotator so far reported.

The symmetry of the Si nano-scale waveguide which consists of the two Si strip core waveguide is therefore been rigorously investigated in this work by using a H-field VFEM [182] to calculate the propagation constant and the modal field profiles of the proposed waveguide structure and a Si strip waveguide.

A Beam Propagation Method (BPM) [183] can be used to calculate the power conversion between the two polarization states; however, the proposed structure consisting of only two discrete interfaces, the Least Squares Boundary Residual (LSBR) [184] method would be more efficient to use to calculate the coefficients of the excited modes at the butt-coupled junctions and also to find the resulting polarization rotation. The half-beat length and polarization crosstalk along with the power loss in the proposed polarization rotator are presented in this chapter. Finally, different lateral offsets between the butt-coupled sections are also considered to further improve the design.

This chapter aims presenting at the important characteristics of silicon nanowire waveguide which is specified with a nano-scale cross section. A novel comprehensive analysis of the performance of polarization waveguide is provided. The supermodes effective indices, field ratio as a hybridism, and more particularly, the modal coefficient, conversion ratio and cross-talk on the device length, have been investigated.

4.1 Numerical analysis:

Accurate calculation of the magnitudes of the non-dominant field components and their profiles for the fundamental quasi-TE and quasi-TM polarized modes are of great importance when designing a polarization rotator. In the design of a compact optical polarization rotator, a full vectorial finite element method (VFEM) is needed and used here to obtain the modal field profiles of the constituent waveguides. In this formulation all the **H**-field components are continuous across the dielectric interface. As for the hybrid modes, a significant non-dominant field component exist around the dielectric interfaces, hence, **H**-field formulation can treat such waveguides more rigorously. In the design process, it is necessary not only to increase the magnitude of the non-dominant field components but also its profile can also be optimized to enhance its overlap with the dominant field components to achieve maximum polarization rotation. This full-vectorial FEM modal solution is also used to determine the polarization beat length between the quasi-TE and TM polarized fundamental modes.

A junction analysis approach is also used, as the proposed polarization rotator structure is composed of two butt-coupled uniform waveguide sections with only two discrete interfaces between them. A powerful numerical approach, the Least Squares Boundary Residual (LSBR) method can be also used, which rigorously satisfies the continuity of the tangential electric and magnetic fields at the junction interface in a least squares sense, and obtains the modal coefficients of the transmitted and reflected fully hybrid modes at the discontinuity

interface. The result of LSBR can provide converted power and polarization rotator along the propagation direction of the polarization rotator. The cross-talk is the unwanted polarization power, which is normalized to the total input power remains at the end of the device.

This particular LSBR method is used to look for a stationary solution to satisfy the continuity conditions by minimizing the error energy functional has been discussed in details in Chapter 2. The integrations carried out over the junction interface, Ω, between the straight and asymmetric Si waveguide.

4.2 Principle of polarization rotator:

In the design of polarization rotator, separation section which supports the highly hybrid modes of the quasi-TE and quasi-TM modes, are accommodated between two asymmetric waveguides where the hybridness is big. If a standard Si waveguide with smaller modal hybridness is placed at this position, this quasi-TM mode would propagate in this waveguide without any further polarization rotation.

When a quasi-TE mode from a standard Si waveguide with its polarization angle at nearly zero degrees (or 90°) is launched into the asymmetric section, which supports highly hybrid modes as M_1 and M_2, with polarization direction ± 45 degree, then both of them are excited almost equally to satisfy the continuity of the $\mathbf{E}_t$ and $\mathbf{H}_t$ fields at that interface, and travels along the asymmetric sections.

The half-beat length (L_π) is a key parameter used in order to identify the optimum length of this section to achieve the maximum polarization rotation. The half-beat length is defined as follow:

$$L_\pi = \frac{\pi}{\Delta\beta} = \frac{\pi}{(\beta^y - \beta^x)} \tag{4-1}$$

Where, β^y and β^x the propagation constants of the quasi-TE (H^y_{11}) and quasi-TM (H^x_{11}) modes, respectively. After propagating a distance, $L = L_\pi$ the original phase condition between the highly polarized modes, M_1 and M_2 would be reversed and the polarization state of the superimposed modes would be rotated by 90° as shown in Fig. 4.1.

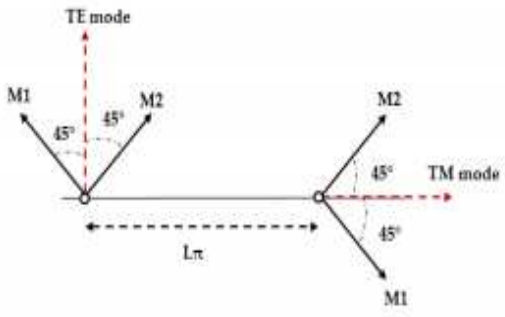

Fig. 4.1 Principle of polarization rotator.

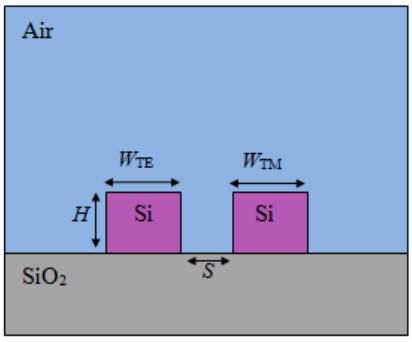

Fig. 4.2 Schematic diagram of a polarization rotator.

4.3 Waveguide of the polarization rotator:

The schematic cross-section of the polarization rotator is shown in Fig. 4.2 consist of two silicon nanowires (NW) but with unequal width. They are of equal height, identified by *H* which would be easy to fabricate. However, they have different widths, given here as W_{TE} and W_{TM}, to achieve phase matching between the quasi-TE (H^{y}_{11}) and quasi-TM (H^{x}_{11}) polarized modes of these two waveguides with unequal widths and it can easily be fabricated by using a SOI wafer on a Si substrate. A single-trench photoresist mask can be used on the surface of the Si core and then etched down to the desire depth in the Si core waveguide. The Si core waveguide then either can be buried under a thick silica (SiO_2) or covered by air.

In the numerical simulations used, the structure is surrounded by air and initially, *W*, is varied in order to study its effect on modal field profiles and particularly the effect of polarization degeneration. In this analysis, the separation between the guides is *S*, as shown here. The refractive index of the silicon and silica are taken as 3.4754752 and 1.4440236 at the operating wavelength of 1.55 μm.

4.4 Phase matching condition in polarization rotator state:

It is well known that propagation constants or the effective indices of the two polarized modes are different for a high index contrast Si NWs due to structural non-symmetry.

Variations of the effective indices, n_{eff}, in the isolated condition for silicon nanowire with the waveguide width for the quasi- TE (H^{y}_{11}) and quasi-TM (H^{x}_{11}) modes are shown in Fig. 4. 3, when height of waveguide is kept in constant at 220 nm. This figure shows that, the effective indices for the quasi-TE and the quasi-TM modes are different and Si NWs are highly birefringent. So, these differences are clearly observed. This graph shows that, when the width of the waveguide is large the effective indices reach to that of the slab waveguide asymptotically.

On the other hand, the effective indices, decreases with the waveguide, *W*. This reduction for the quasi-TE (H^{y}_{11}) mode is more rapidly than quasi-TM (H^{x}_{11}) mode. It can be also noticed that, the quasi-TE and quasi-TM modes approach their cut-off when the width of the waveguide is lower than 150 nm, and 100 nm, respectively.

Since for most of the Si NW the effective indices of the quasi-TE (H^{y}_{11}) and quasi-TM (H^{x}_{11}) modes are not equal, so a directional coupler using two identical NWs, the quasi-TE (H^{y}_{11}) mode in one guide will not be phase matched to quasi-TM (H^{x}_{11}) mode in the other guide. However, by using unequal widths for these two guides quasi-TE (H^{y}_{11}) mode in one guide can be phase matched to the quasi-TM (H^{x}_{11}) mode in the other guide, as illustrated in Fig. 4.2. Now, it is considered to find the necessary width of the waveguide (W_{TE}) supporting the quasi-TE (H^{y}_{11}) mode to be phase-matched with another guide with the waveguide of the quasi-TM (H^{x}_{11}) mode, W_{TM}.

The necessary width of a guide (W_{TE}) supporting the quasi-TE (H^{y}_{11}) mode to be phase matched with another guide with width (W_{TM}) supporting the H^{x}_{11} mode is studied.

To obtain maximum interaction between the the two polarized modes their effective indices are need to be equal.

The condition causes the power transfer between the two modes to be almost 100 % which means the modes are phase-matched. In this case, the magnitude of the field components of the fundamental quasi-TE (H^{y}_{11}) mode and also quasi- TM (H^{x}_{11}) mode gets to its maximum amplitude.

It can be noticed that, the minimum device coupling length is also occurred in phase-matching condition.

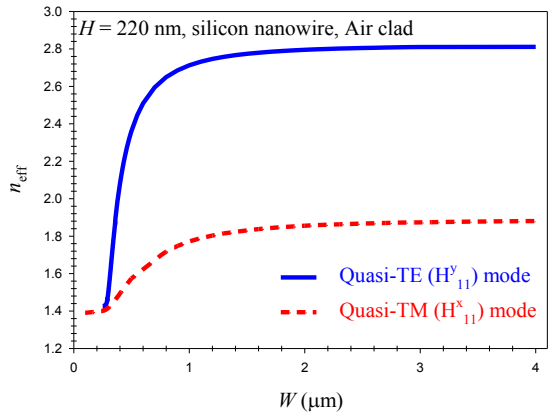

Fig. 4.3 Variation of the effective indices for the quasi-TE and quasi-TM modes with the waveguide width, *W*.

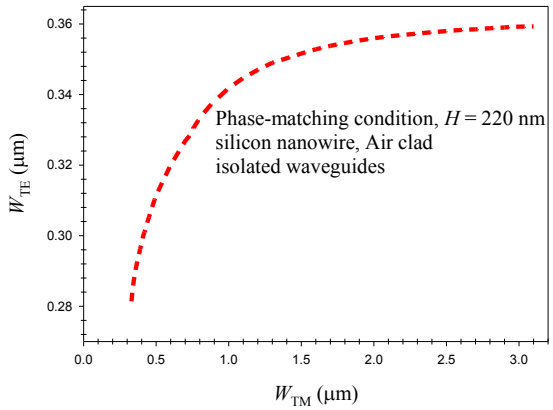

Fig. 4.4 Phase matching widths condition, *W*, for the quasi-TE (H^{y}_{11}) and the quasi-TM (H^{x}_{11}) modes in two isolated waveguides.

Variation of the phase-matching condition for the waveguide height equal to 220 nm is shown in Fig. 4.4. The results for the isolated waveguides shows that, when the width of W_{TM} is 1200 nm, the width necessary (W_{TE}) for phase-matching its quasi-TE mode is 350 nm, when the design is kept in H = 220 nm, and at this time, effective indices for both modes are 1.80. It is illustrated that, generally the quasi-TM (H^{x}_{11}) mode curve of the waveguide width as a comparison cover wider range than in waveguide width of the quasi-TE (H^{y}_{11}) mode. This figure shows that, with increasing the waveguide width of the quasi-TE (H^{y}_{11}) mode, the required width of the quasi-TM (H^{x}_{11}) waveguide is increased, and reach to the saturation point.

Variations of the effective indices, n_{eff} of the quasi-TE (H^{y}_{11}) and quasi-TM (H^{x}_{11}) modes for isolated silicon NW waveguide but with longer heights, H = 260 nm and 300 nm are shown in Fig. 4.5. It can be observed that when the width of the guide is large the effective indices reach that of a slab waveguide (with the same height) asymptotically. However, as the width is reduced, initially effective indices reduce slowly and then quite rapidly as the cut-off width is approached. It can be noticed that effective indices of the H^{y}_{11} mode is higher than that of the H^{x}_{11} mode, particularly when the width is large.

It can be noted, but not clearly observed that H^x_{11} mode approaches its cut-off when the width is lower than 200 nm and 150 nm, for H = 260 nm and 300 nm, respectively. Similarly the H^y_{11} modes approach their cut-off when W is reduced below 265 nm and 260 nm for H = 260 nm and 300 nm, respectively.

Variations of the waveguide width, $W_{TE,}$ of the quasi-TE (H^y_{11}) mode necessary to phase match a guide with the waveguide width, W_{TM} in quasi-TM (H^x_{11}) mode are shown in Fig. 4.6 for three different waveguide heights, H of photonic devices. It can be seen that the curve related to H = 350 nm is much bigger than the trend depend on height equal to 260 nm. As example, for the height 260 nm, shown by a dark yellow dashed-dotted line, and when the width of W_{TM} is 600 nm, the width necessary (W_{TE}) for phase-matching its quasi-TE mode is 353 nm and at this time effective indices for both the modes are 2.00. However, this phase matching condition shown here is strictly valid only for the isolated guides.

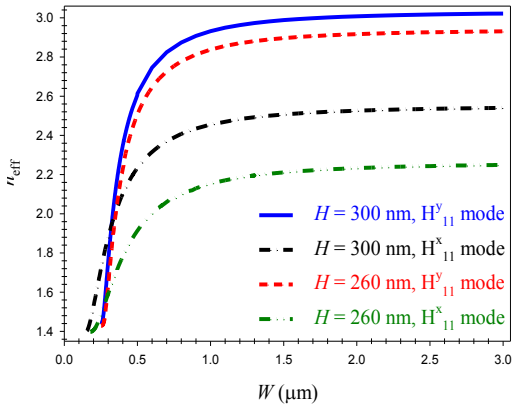

Fig. 4.5 Variation of the effective indices for the quasi-TE and quasi-TM modes, with the waveguide width, W.

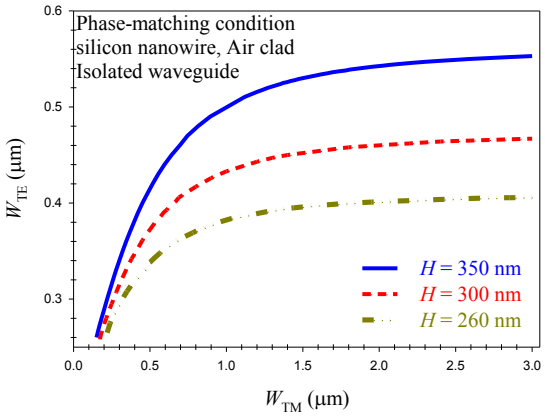

Fig. 4.6 The phase-matching widths, W, for quasi-TE (H^y_{11}) and quasi-TM (H^x_{11}) modes in two unequal waveguides.

4.5 Effective indices of the supermodes:

In a directional coupler, as shown in Fig. 4.2 to obtain phase-matching between the quasi-TE (H^y_{11}) and quasi-TM (H^x_{11}) modes of the two waveguides of different width is considered. It is well known that for non-identical waveguides the loading of one waveguide to another are unequal for both of them. So, in the next stage of the design the supermodes of this directional coupler structure are studied.

Here, the waveguide height is taken as 300 nm, and width of the first guide, W_{TE}, is kept fixed at 366 nm, when the effective index of the quasi-TE mode is equal to 2.20.

Variation of the effective indices for fundamental quasi-TE (H^y_{11}) and quasi-TM (H^x_{11}) modes with the second waveguide width, W_{TM}, are shown in Fig. 4.7. In this case separation between the guides is taken as 200 nm. So when the W_{TM} was varied, effective index of the fundamental quasi-TE (H^y_{11}) mode remained almost constant, shown by a horizontal line. However, as W_{TM} was increased, n_{eff} quasi-TM (H^x_{11}) mode increased progressively. The effective index of the quasi-TM (H^x_{11}) mode reached to be equal to that of the quasi-TE

(H^{y}_{11}) mode at W_{TM} = 465 nm. Actually, the effective index curves did not cross, but mode continuously transforms at the anti-crossing point.

Figure 4.8 shows the variations of effective indices for quasi-TE (H^{y}_{11}) and quasi-TM (H^{x}_{11}) supermodes with varied waveguide width, W_{TE} when the height is fixed at 220 nm. For this case, the separation was fixed at 150 nm. The right waveguide width was equal to 1.20 μm and the effective of its TM mode was remained roughly constant at 1.80.

According to the figure 4.8, it is seen that, when W_{TE} was increased from 325 nm, the optimum point of 359 nm effective index for TE mode was increased, while effective index for TM mode was remained stable. It can be noticed that, for the higher value of the device length, the effective index for TE mode reached the n_{eff} value of the TM mode.

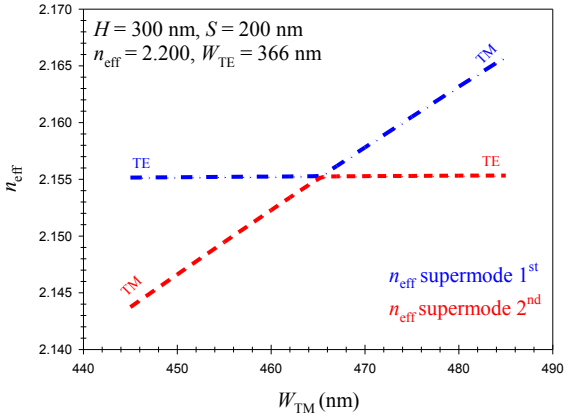

Fig. 4.7 Variations of the effective indices for the fundamental quasi-TE (H^{y}_{11}) and TM (H^{x}_{11}) modes with the waveguide width, W_{TM}.

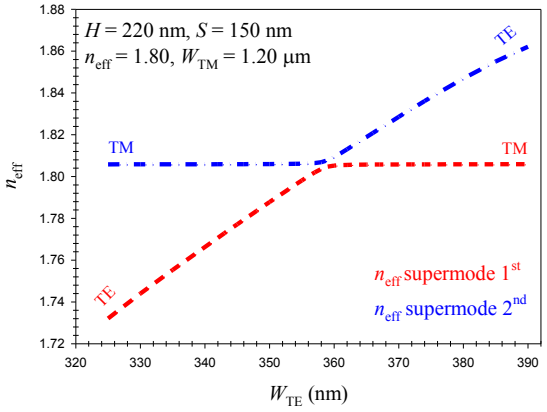

Fig. 4.8 Variations of the effective indices for the fundamental quasi-TE (H^{y}_{11}) and TM (H^{x}_{11}) modes with the waveguide width, W_{TM}.

Figure 4.9 shows the variations of effective indices for quasi-TE (H_{11}^{y}) and quasi-TM (H_{11}^{x}) supermodes with varied waveguide width, W_{TM}. For this case, the height of waveguide and separation were fixed at 260 nm and 200 nm, respectively. The left waveguide width was equal to 353 nm and effective index of its TE mode remained roughly constant at 2.00. According to this figure, it is seen that, when W_{TM} was increased from 515 nm, the optimum point of 575 nm effective index for TM mode was increased, while effective index for TE mode was remained stable. It can be noticed that, for the higher value of the device length, the effective index for TM mode converted to the n_{eff} TE mode. It can be observed that W_{TM} is increased from 515 nm, the effective index of its quasi-TM mode progressively increases. When $W_{TE} \approx 575$ nm, effective index of its quasi-TM mode becomes equal to that of the effective index of quasi-TE mode of the W_{TE} with its width 353 nm. However, as supermodes, effective indices of these supermodes, never crosses. When W_{TM} is lower than 575 nm, first supermode is like the quasi-TE mode is the left guide and the second supermode is like the quasi-TM mode in right guide. When $W_{TM} > 577$ nm, they change their positions and the first supermode is now is like the quasi-TM mode in the right guide and 2th supermode is like the quasi-TE mode in the left guide as stated in this figure. However, when

$W_{TM} \approx 575$ nm, the soupermodes are highly complex and they are combination of both quasi-TE and quasi-TM modes, and exist in both the guides. These highly hybrid supermodes are shown in Figures 4.11 – 4.18.

Variation of the effective indices for the two supermodes are shown in Fig. 4.10 for two different waveguide separations, S. Both the cases width of W_{TE} supporting quasi-TE mode is kept constant at 353 nm. It can be observed that for a larger separation, S = 200 nm, as the width, W_{TM} is varied, effective index of one of the supermode remains almost constant. This supermode mostly looks like the H^y_{11} mode of guide 1 (quasi-TE mode in W_{TE} with a fixed width of 353 nm). On the other hand the effective index of the other supermode increases with the 2nd waveguide width, W_{TM} and this mode mostly resembles the H^x_{11} mode of this guide (W_{TM}).

However, the effective index curves do not cross each other but like the supermodes of a directional coupler transform from one isolated mode to another. In this case, phase match condition is happening the H^x_{11} mode of one guide (W_{TM}) with the H^y_{11} mode of another guide (W_{TE}), near the interactions regions, two supermodes show the mixture of both the polarized modes which are highly hybrid in nature.

For S = 200 nm, when W_{TM} = 577 nm, H^x_{11} mode of this guide is phase matched with the H^y_{11} mode of W_{TE} = 353 nm width. When the separation is reduced, the interactions between the polarized modes are more intense, which demonstrates a larger gap between the two effective indices near the phase matching. However, the phase matching width of 2nd guide, W_{TM}, changes as mutual loading of two unequal guides for different separations are also different.

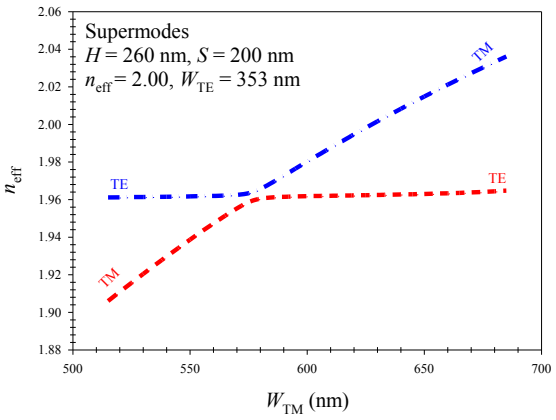

Fig. 4.9 Variations of the effective indices for the fundamental quasi-TE (H^y_{11}) and TM (H^x_{11}) modes with the waveguide width, W_{TM}.

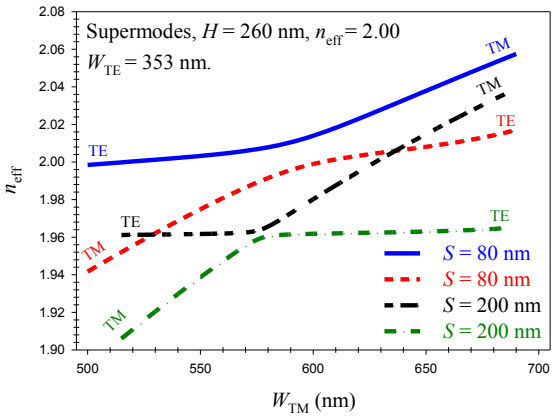

Fig. 4.10 Variations of the effective indices of two supermodes for the fundamental quasi-TE (H^y_{11}) and TM (H^x_{11}) modes with the second guide width, W_{TM}.

4.6 Analysis of the H-field modal characteristics:

Near the phase matching these supermodes are highly hybrid in nature and shows a combination of the both the polarized modes, and the field profiles of both the modes are

shown here. The dominant H_y field component of the quasi-TE (H^y_{11}) mode is shown in Fig. 4.11, when the first waveguide width of the supermodes is 353 nm, and second waveguide width is fixed in W_{TM} = 593 nm, and its height is kept 260 nm. These supermodes are highly hybrid in nature and shows a combination of the polarized modes. It should be noted here that the H_y field is mainly in the left waveguide in the directional coupler device in width of the waveguide, W_{TE}. However, it can also be observed that field also spread in the other waveguide.

Figure 4.12 shows the 3-dimensional field profile of the dominant H_y field of the quasi-TE (H^y_{11}) mode. In this case sign of the amplitude field is negative and its magnitude is equal to 3. The non-dominant H_x field profile of the same supermodes quasi-TE (H^y_{11}) mode shown in Fig. 4.13, which illustrates the H_x field component is predominantly in the right hand side guide, in W_{TM}. This field profile is clearly shown to be anti-symmetric in nature.

Figure 4.14 shows the 3-dimensional form of the non-dominant H_x field component of the quasi-TE (H^y_{11}) mode and its maximum magnitude is about 3, which normalized to the maximum value of the H_y field. In this case signs of both the H_x and H_y fields opposite and their magnitudes nearly equal, so the resulting polarization angle is – 45 ^{0} degrees with the *X*-axis. It should be noted that since all the three components of the **H**-field are continuous across the dielectric interfaces, the H_x contours do not show any singularities at the corners. Vector field profiles of the second supermodes are shown in Fig. 4.15. Its H_x field in this figure shows that mainly power is confined in the right of the waveguide. Here, the dominant H_x field component of the quasi-TM (H^x_{11}) mode is nearly similar in shape like that of the dominant H_y mode in Fig. 4.5. For this mode magnitude of the H_x field is found to be maximum value about 3 in Fig. 4.16.

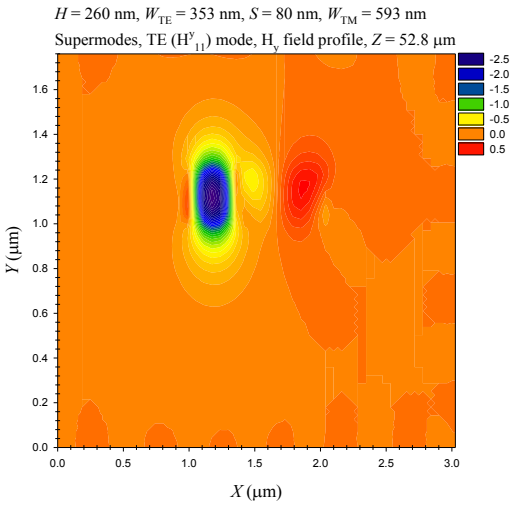

Fig. 4.11 The dominant H_y field component of the quasi-TE coupled supermode.

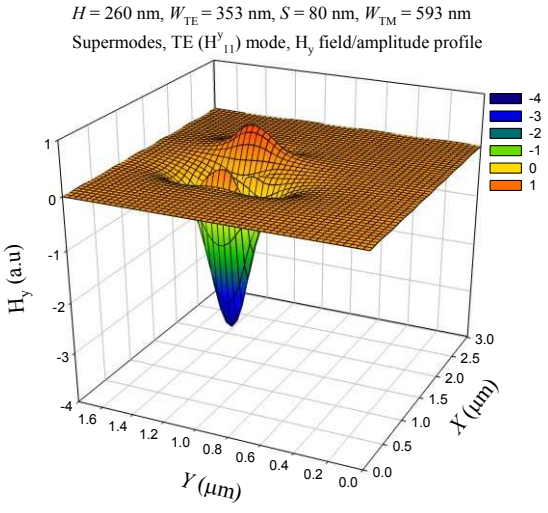

Fig. 4.12 The 3-dimensional view of the dominant H_y field of the coupled H^y_{11} (TE) supermode.

The non-dominant H_y field component and its 3-D field profile are shown in Figs. 4.17 and 4.18, respectively, and these field profiles show a similar behaviour as the H_y contours and

spatial profile of quasi-TE (H^{y}_{11}) mode, but of opposite sign. On the other hand, It can be noticed that magnitude of the H_x and H_y fields in the second supermodes (H^{x}_{11}mode), were similar, so its resulting polarization angle is + 45 degrees with the x-axis. It should be noted the waveguide on the left (W_{TE}) had a fixed width and its quasi-TE (H^{y}_{11}) mode was matched with the quasi-TM (H^{x}_{11}) mode of the right guide (W_{TM}), whose width was varied. Hence for both the supermodes, it can be observed that its H_y field was mainly in the left guide whereas H_x field was mainly in the right side waveguide.

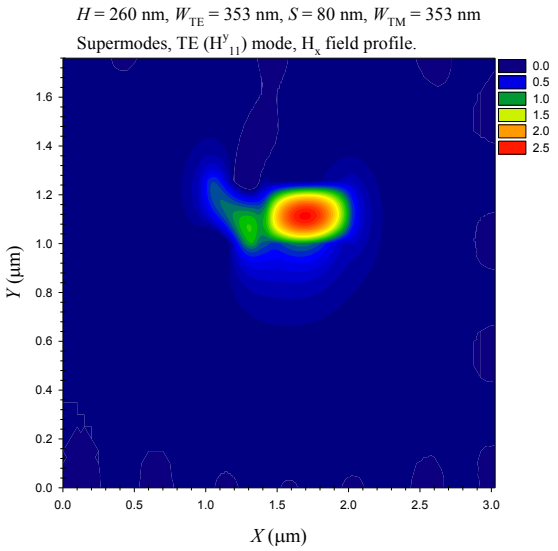

Fig. 4.13 The non-dominant H_x field component of the quasi-TE (H^{y}_{11}) mode.

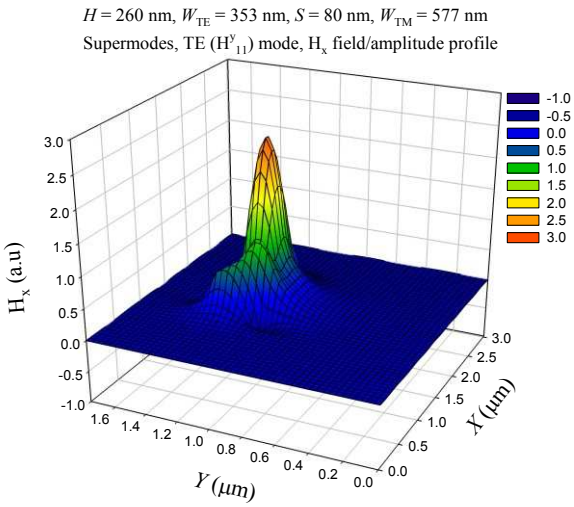

Fig. 4.14 The 3-D view of the non-dominant H_x field of the H^{y}_{11} (TE) mode.

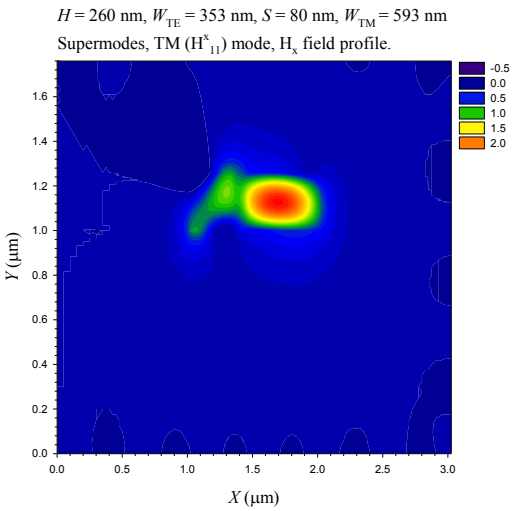

Fig. 4.15 The dominant H_x field component of the quasi-TM (H^{x}_{11}) mode, for the H = 260 nm, W_{TE} = 353 nm, and W_{TM} = 353 nm.

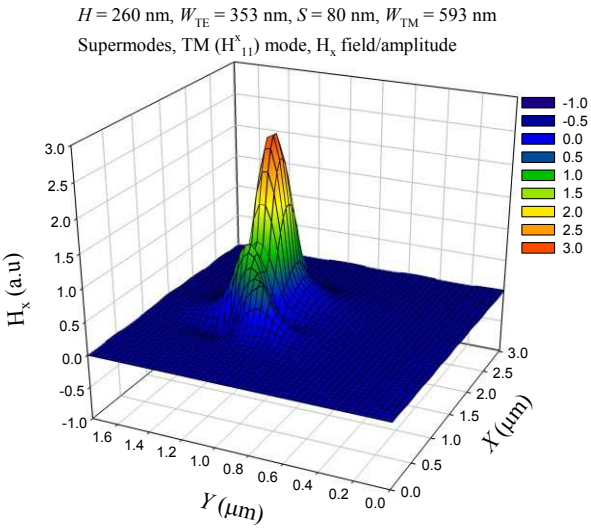

Fig. 4.16 The 3-D view of the H_x field component in quasi-TM for the second supermodes, when, W_{TE} = 353 nm, and W_{TM} = 593 nm.

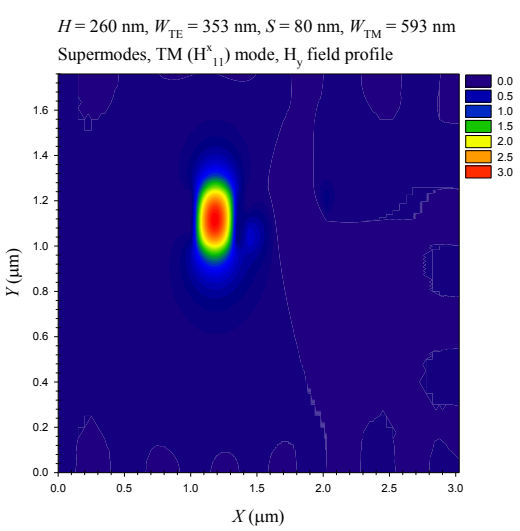

Fig. 4.17 The non-dominant H_y field component of the quasi-TM (H^x_{11}) mode, when, H = 260 nm, W_{TE} = 353 nm, S = 80 nm, and W_{TM} = 593 nm.

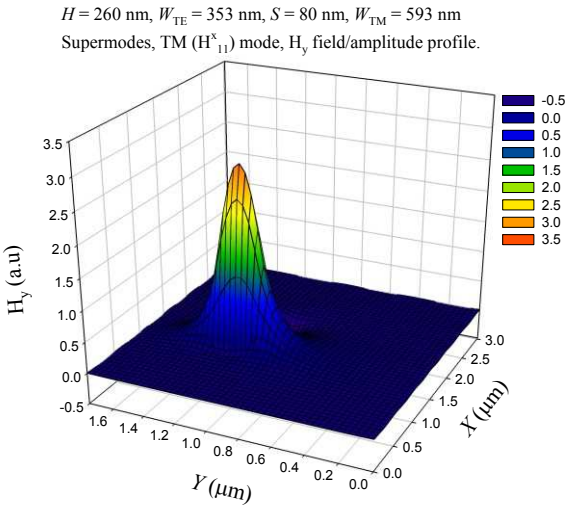

Fig.4.18 The 3-D view of the non-dominant H_y field component of the quasi-TM (H^x_{11}) mode, H = 260 nm, W_{TE} = 353 nm, S = 80 nm, and W_{TM} = 593 nm.

4.7 Analysis of the hybridism in the polarization rotator device:

The optical modes in polarization rotator waveguide devices are hybrid in nature. In the design of a polarization rotator, one of the main and most important objectives is to increase the non-dominant field values of the quasi-TE and quasi-TM modes. For the fundamental quasi-TE (H^y_{11}) mode, the E_x and H_y field components are the dominant field components, and E_y and H_x field components are the dominant field components of the fundamental quasi-TM (H^x_{11}) mode. Therefore, if the H_x / H_y ratio for the quasi-TE (H^y_{11}) mode or the H_y / H_x ratio for the quasi-TM (H^x_{11}) mode is high, there exists a high possibility of achieving polarization rotation. Unlike the compact passive polarization rotator, which contains two simple silicon nanowire waveguides (NWs) is capable for an enhanced field hybridism by destroying symmetry of the structure. The polarization rotator design presented here exploits two highly hybrid supermodes supported by a phase matched, that, between two different polarized modes in directional coupler structure.

The effect of the waveguide width, W_{TM}, on the modal hybridism is shown in Fig. 4.19. This figure shows the modal hybridness for a coupled structure with a height of 300 nm, a fixed waveguide width supermodes TE mode equal to 363 nm, separation of 200 nm and with of waveguide soupermodesTM mode is varied. As mentioned that, the modal hybridness is defined as the ratio of the maximum value of non-dominant field to that of the dominant field. In the case of the H^y_{11} mode, the modal hybridness is given by the ratio of the non-dominant H_x field (the maximum value) to the dominant H_y field (its maximum value) and it is shown by a dashed-dot line. The modal hybridness of the H^x_{11} mode, calculated from the ratio of the maximum value of the H_y field to the H_x field, is also shown by solid line. It can be seen here that for both polarized modes, when W_{TM} is reduced from 468 nm to 465 nm, the hybridness is increased rapidly. Hybridness of the both the quasi-TE and quasi-TM modes are mostly constant equal to ≈ 0.2 for the whole range of W_{TE} varied. However, when

$W_{TM} \approx 466$ nm, then hybridness of both the quasi-TE and quasi-TM increase rapidly, as two degenerate isolated modes of different polarizations forms the two supermodes. As it can be observed that hybridness of H_x / H_y is more than hybridness of H_x / H_y, which, 0.95 and 0.84, respectively. The further W_{TM} away from resonance point the less values of the field ratio will be. This reduction is quite significant.

Figure 4.20 shows the modal hybridism for both H^y_{11} and H^x_{11} modes with W_{TM}. It can be seen that when W_{TM} was increased hybridism modes were increased to width of resonance equal to 577 nm and device length of 530 µm. At exactly 577 nm width of the waveguide TM mode, the hybridism reaches its maximum value of nearly one, which indicates that both of the transverse field components are almost equal.

The waveguide considered here remains single mode until $W_{TM} = 577$ nm and a waveguide wider than that supports higher order modes. From this point the increase in W_{TM} caused decrease in hybridism modes. However, the hybrid nature of the TM mode is slightly higher than that of the TE mode for a given waveguide width (1.135 and 0.91 respectively). Also, compare to Fig. 4.19, the spread of hybridness was much more in this case.

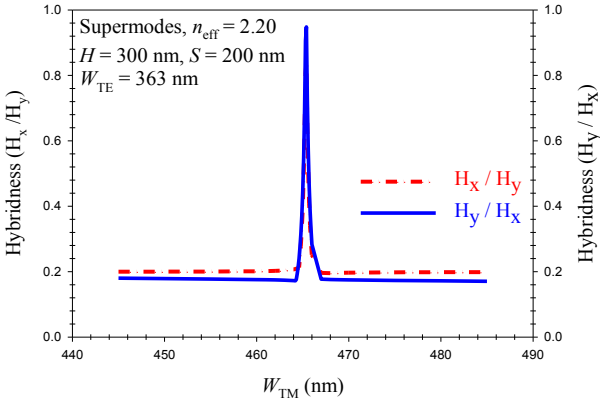

Fig. 4.19 Variation of the hybridness with 2nd waveguide width, W_{TM}, for the fundamental quasi-TE (H^y_{11}) and quasi-TM (H^x_{11}) modes.

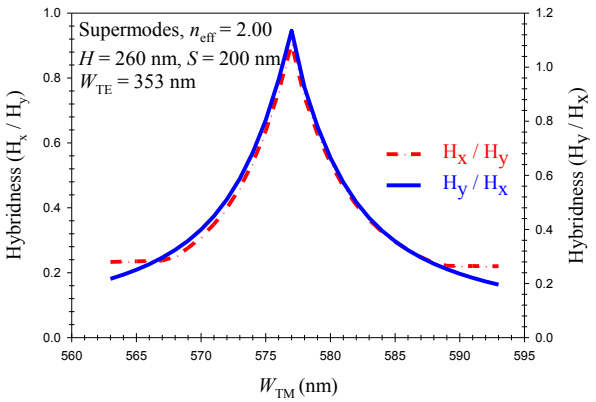

Fig. 4.20 Variations of the hybridness with the second waveguide width, W_{TM}, for the fundamental quasi-TE (H^y_{11}) and quasi-TM (H^x_{11}) modes.

Variations of the modal hybridness of the first supermode with the waveguide width (W_{TM}) are shown in Fig. 4.21. It should be noted that when the two polarized modes in two waveguides are phase matched the magnitudes of the H_x and H_y fields are nearly equal, but, not exactly equal as their core areas were not identical, and hybridness increases.

It can also be noted when separation between the waveguides is reduced, as shown by a solid blue line for $S = 80$ nm, the reduction of the modal hybridness is slower with the waveguide width variation allowing a more stabilized design. A quasi-TE mode in a standard silicon NWs will have higher H_y field compared to its non-dominant H_x field.

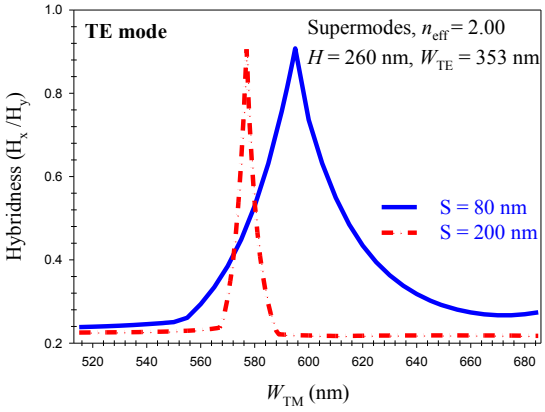

Fig. 4.21 Variations of the hybridness with the waveguide width, W_{TM} for the fundamental-TE (H^y_{11}) mode.

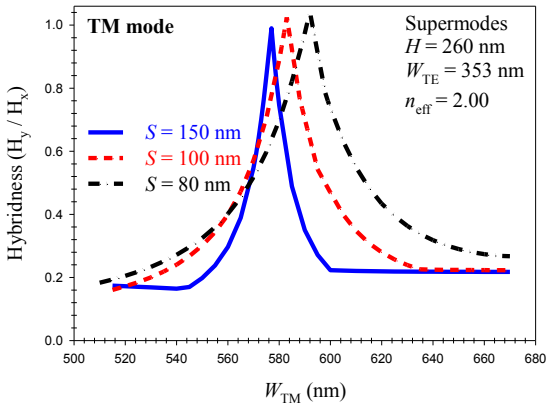

Fig. 4.22 Variations of modal hybridness of the quasi-TE (H^y_{11}) mode with the waveguide width, W_{TM}, for three different values of S = 80 nm, 150 nm, and 200 nm.

Around anti-crossing point, these two modes become degenerate and they get mixed up. For a quasi-TE mode, the H_y component is dominant whereas for a quasi-TM mode, its H_x component is dominant. Near anti-crossing the non-dominant field starts increasing leading to higher modal hybridness, which can be defined as the ratio of the maximum values of the H_y to H_x field components for the TM and similarly H_x / H_y for the TE mode. In Fig. 4.22, at lower W_{TM}, the mode is near quasi-TM, with H_y component being much smaller. So its hybridness is low. As W_{TM} increases, it travels through the anti-crossing region leading to stronger mode mixing and higher hybridness. At a higher W_{TM}, away from this anti-crossing region, again hybridness reduces. All the peaks appear around the mode exchange regime with increasing value as S decreases. Note that for smaller S, curves are wider as mode coupling get stronger, the interaction become easier.

4.8 Calculation of optimum device length:

The device length (L_c) is key and an important parameter used in order to identify the optimum length of the asymmetrical section to achieve the maximum polarization rotation. This parameter is employed for designing polarization rotators because this also represents the convertor length that must reverse the polarization state from one to the other. This length is the proportion of π over the difference between propagation constant (birefringence). At the L_π, the phase mismatch between the two polarized modes, H^y_{11} and H^x_{11}, is also at its minimum. To obtain maximum polarization rotator and also the maximum power conversion, the length of the polarization rotator waveguide is needed to be equal to the half-beat length L_π of the two polarized modes.

Figure 4.23 shows the variations of the coupling length with the waveguide width, W_{TE} for three separations (S = 80 nm, S = 100 nm and S = 150 nm). The fixed values for the device were H = 220 nm, n_{eff} = 1.80, W_{TM} = 1.20 µm, with varied waveguide width, W_{TE}.

From Fig. 4.23, it can infer that, as S increases, coupling become weaker, and hence, Δβ is getting smaller near anti-crossing point, so peak L_c become larger. From this figure, it should

be noted that as separation between the waveguides is reduced the phase matching value of W_{TE} reduces. When a directional coupler is composed of two identical WGs, they are always phase matched or synchronous. But, for asynchronous coupler composed of non-identical waveguides, its phase matching also depends on mutual loading of the waveguides. Consequently, the phase matching condition for W_{TE} value changes with S, as shown here, as mutual loading are unequal for coupler with unequal widths.

Figure 4.24 are shows the variation of the coupling length in Log-scale with the $W_{TE} - W_{res}$, when height of the device is kept in 220 nm, and n_{eff} = 1.80. Here, to study the effect of fabrication tolerance is used from W_{res}, which is the phase matching resonating width. It can be noticed from this figure that for the W_{res} = 353 nm, W_{res} = 356 nm, and W_{res} = 358 nm, the separation between the guides, S, should be 80 nm, 100 nm, and 150 nm, respectively to consider the 1st waveguide of width value, W_{TM} = 1.2 µm. In these cases, half beat length (the maximum coupling length) is to be 131µm, 160 µm, and 252 µm, respectively, and also, the trends are symmetric with respect to the resonance points.

Figure 4.25 shows the half-beat-length which is normalized to their maximum coupling length for the different separations (S = 80 nm, S = 100 nm, S =150 nm and S =200 nm) with the waveguide width, W_{TM}. In this case the height equal to 260 nm, and width of waveguide (W_{TE}) for the quasi- TE (H^{y}_{11}) mode fixed at 353 nm.

Figure 4.24 shows that when separation was 80 nm the normalization of coupling length would cover ± 70 nm deviations from the optimum width of the fundamental quasi-TM (H^{x}_{11}) mode. While, for S = 200 nm, the coverage for normalization was ± 16 nm from the optimum point in the waveguide width, W_{TM}. This extreme reduction in deviation for S = 200 nm was result of the poor hybridism as shown in Figs. 4.21, and 4.22.

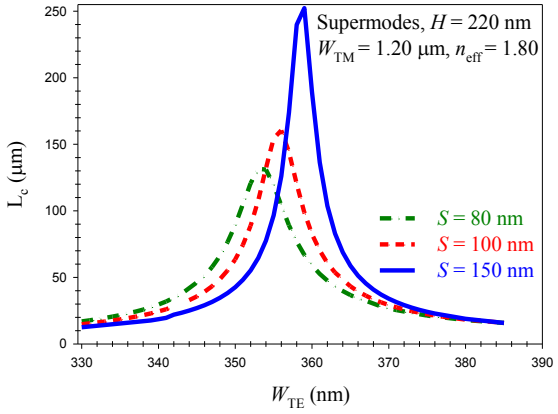

Fig. 4.23 Variations of coupling length (L_c) with W_{TM} for three different S = 80 nm, 100 nm, 150 nm.

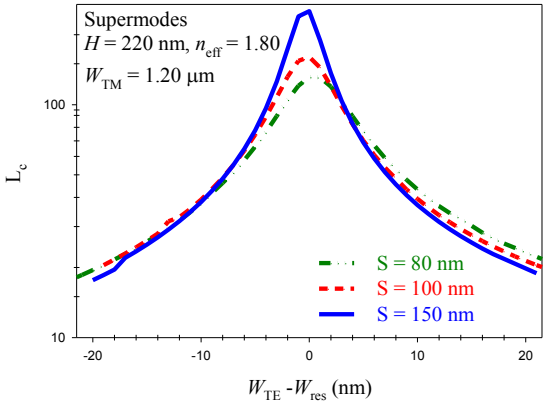

Fig. 4. 24 Variations of half-beat-length L_c with the waveguide width, $W_{TM} - W_{res}$.

Variations of the coupling length L_π in log-scale with the second guide width (W_{TM}) for the height of waveguide 260 nm are shown in Fig. 4.26 for different waveguide separations. In

this case width of the first NW (W_{TE}) was fixed at 353 nm supporting the quasi-TE (H^{y}_{11}) mode with its effective index 2.00. It can be noted that when phase matching was achieved the difference between the effective indices of the two supermodes were minimum and so the coupling length shows a peak value.

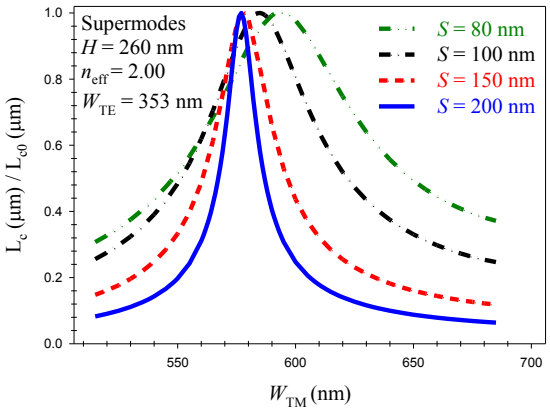

Fig. 4.25 Variations of normalized half-beat-length L_π with the waveguide width, W_{TM}.

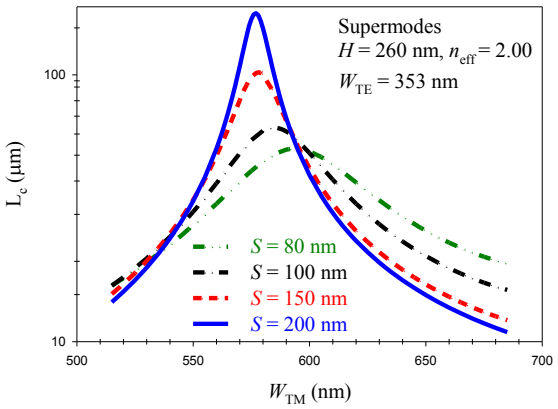

Fig. 4.26 Variations of the coupling length, L_c with the second waveguide width, W_{TM}, for different waveguide separation, S.

It can also be observed that, there are various maximum half-beat-length devices for the different separations and also, coupling length is higher when separation is increased and its variation with the waveguide width (W_{TM}) is also sharper.

The maximum coupling length which 170 μm would be at separation S = 200 nm, while the optimum point for 80 nm separation was 53 μm. It can be noted that phase matching width (W_{TM}) for separation, S = 200 nm, 150 nm, 100 nm and 80 nm were respectively 577 nm, 578 nm, 585 nm and 593 nm, respectively (the width W_{TE} was kept constant at 353 nm).

The changes in the phase matching condition are due to unequal loading on one guide by the other and this loading changes as the separation between the guides reduces. It should be noted that for smaller separation not only the coupling length is smaller, but it would be less sensitive with the change in the waveguide width. .

It is also shown that with ± 70 nm deviation from the optimum point, half- beat-length took place on about 82 % of waveguide width, W_{TM} for separation of the 80 nm. However, with ± 35 nm deviation from the optimum point, the half-beat-length was found to cover almost 12 % of waveguide width, W_{TM} at S = 200 nm. All mentioned various in coupling length devices were symmetric at their optimum points of devices in terms of 2nd waveguide width, W_{TM}.

4.9 Choice of the Optimum device parameters:

In this study, the effect of other waveguide parameter, similar effective index difference between the 1st and 2nd supermodes, Δn was considered to understand its effect and to obtain optimizes parameter values to achieve better polarization conversion.

The half-beat length (L_c) is a key parameter used in order to identify the optimum length of the asymmetrical section to achieve the maximum polarization rotation. At the L_c, the phase mismatch between the two polarized modes, H^y_{11} and H^x_{11}, is also at its minimum. Figure 4.27 shows the variations of the L_c with the W_{TM}. In Fig. 4.27, it is shown in here that L_c starts to increase when W_{TM} increases until it reaches its maximum value, and then the L_c gradually reduces as W_{TM} further increases. Therefore in this study, when the two modes are degenerate, their hybridness is about 1.0, their polarization angles are ± 45° and that L_c also reaches the maximum value of 52.8 μm. It is also shown in Fig. 4.27 that the variations of the modal birefringence with the change of W_{TM}, the minimum modal birefringence is found to be 0.01465 at W_{TM} = 593 nm.

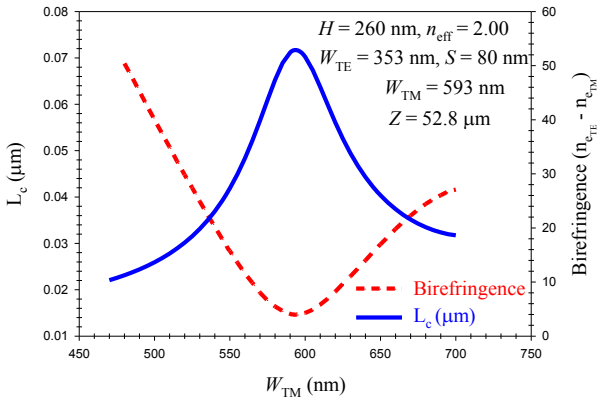

Fig. 4.27 Variations of L_c and birefringence with the second waveguide width, W_{TM}.

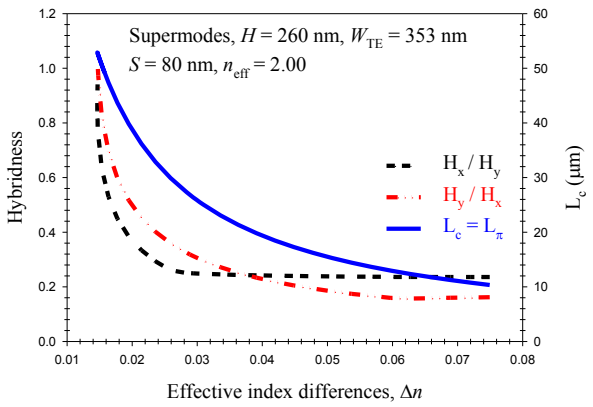

Fig. 4.28 Variations of the hybridness and coupling length, L_c with the refractive index difference.

The effect of index different, $\Delta n = n_{e\text{-}TE} - n_{e\text{-}TM}$, has been investigated in Fig. 4.28. The variation of the H_x / H_y and H_y / H_x field ratios for the H^y_{11} and H^x_{11} modes, respectively, and the half-beat length, L_c, with the birefringence are shown in Fig. 4.28. Here, the 1st waveguide width is kept constant at W_{TE} = 353 nm and the 2nd waveguide, W_{TM} is varied from 705 nm to 596 nm.

It can be observed from the figure, that hybrid nature is reduced when Δn is reduced, the reason believed to be the fact that the modes are much more confined in the guide core and the fields at the waveguide slab are rather small (for the same core dimensions).

However, one important factor that can be observed is the significant reduction of L_c, which can give rise to a better compact polarization rotator design. When Δn = 0.075, the L_c value was smaller, but hybridness was also smaller, so will not be a better design.

4.10 Least Squares boundary residual method results in the polarization rotator device:

In this section, modal coefficients, power conversion and cross-talk are rigorously studied. It was shown in previous section that the modes obtained from the polarization rotator waveguide are not pure TE or TM, but hybrid in nature. Moreover due to the asymmetric of the rotator waveguide, it is possible to achieve polarization conversion, where if a quasi-TE (H^{y}_{11}) or quasi-TM (H^{x}_{11}) mode is launched at the start of the directional coupler section as Figure 4.29, this would excite two highly-hybrid supermodes at the junction between the input and rotator waveguides, whose field profiles were shown in Figs 4.11 – 4.18. The fundamental boundary conditions is the continuity of the tangential electric (E_t) and magnetic (H_t) fields at the dielectric interface. A quasi-TE mode in a standard silicon nano-wire will have higher H_y field compared to its non-dominant H_x field and also, in quasi-TM mode in isolated Si-NWs, the amplitude of the H_x field is higher than the amplitude of its H_y field. The rigorous Least Squares Boundary Residual method [184] is used to implement these boundary conditions. This method yields the modal coefficients of the two supermodes excited in the directional coupler section**.**

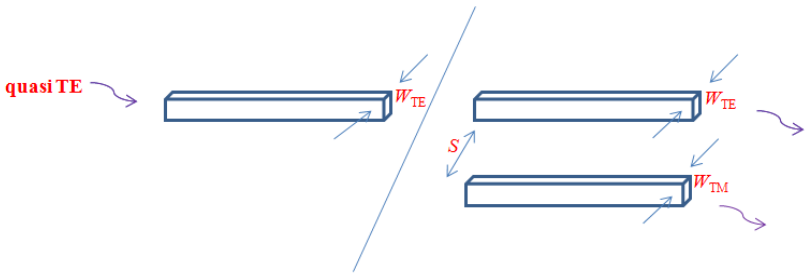

Fig. 4.29 Discontinuity representation for LSBR.

4.10.1 Characteristics of the transmitted modal coefficient:

According to the section of 4.7, the incoming quasi-TE polarized wave of a standard silicon waveguide would excite two highly hybrid, with ± 45° polarized modes in the asymmetric section.

To quantify further in the analysis, the scattering modal coefficients, C_y and C_x of the two fundamental quasi-TE (H^{y}_{11}) and TM (H^{x}_{11}) modes, respectively, at the junction need to be obtained. In this study, a rigorous numerical solution using the LSBR has been used to obtain the modal coefficients at the discontinuity interface by enforcing the boundary conditions in a least squares sense.

The butt-coupling of the standard input silicon-NW waveguide with vertical side walls, and the PR waveguide was considered as the mode conversion can only be expected to happen at waveguide discontinuities.

For the input waveguide, the silicon NW waveguide width is taken W_{TE}, and no transverse offset between the guides has been considered. The junction of the waveguide is shown in as in Fig. 4.30.

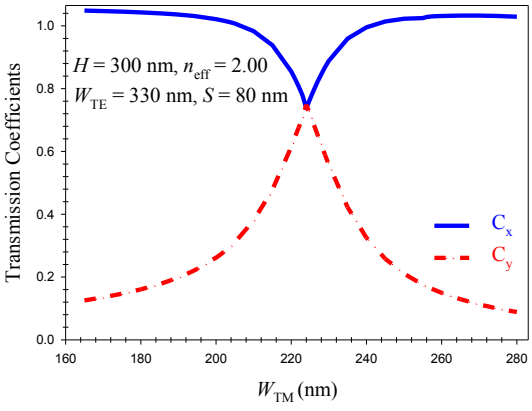

Fig. 4.30 The variations of the excited transmitted modal coefficients C_x, C_y, with the PR waveguide, W_{TM}, for the input fundamental quasi TE (H^y_{11}) mode.

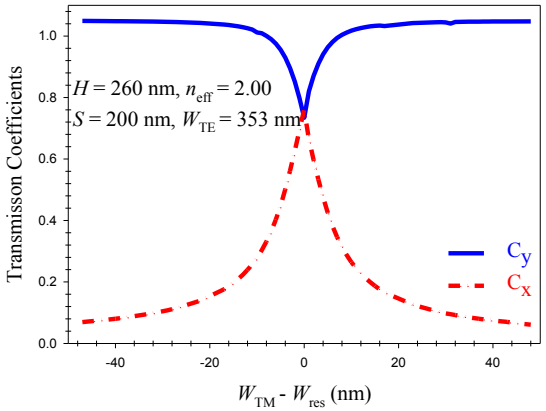

Fig. 4.31 Variations of the transmitted modal coefficients C_x, C_y, with the waveguide, W_{TM}-W_r, for the input fundamental quasi TE (H^y_{11}) and quasi TM (H^x_{11}) modes.

When a quasi-TE (H^y_{11}) mode from the input guide with very small hybridness is incident on the PR waveguide, it excites two highly hybrid modes, C_x, and C_y. The variation of these two parameters with the PR waveguide width, W_{TM}, is shown in Fig. 4.30. It can be seen that at W_{TM} = 280 nm, C_x is 1.03 and as W_{TM} is reduces, it reaches a minimum value of 0.77 at W_{TM} = 225 nm. On the other hand, at W_{TM} = 280 nm, C_y is 0.088 and it reaches a maximum value of about 0.75 at W_{TM} = 280 nm, where the hybridness is at its highest.

For a system where 100 % polarization rotation can be achieved without any power loss, these two values are expected to be equal to $1/\sqrt{2}$, indicating that each mode is carrying equal and half of the total power (50 % of the total input optical power). Hence in this case, at the mode degeneracy condition, since the modal coefficient of both the modes are similar, the power carried by each of them is also similar and here the total power loss is found to be only 0.1 dB, which is very small.

The transmitted modal coefficients, C_y and C_x of the fundamental quasi-TE (H^y_{11}) and quasi-TM (H^x_{11}) modes, respectively, were calculated and the variations of these two modal coefficient with the polarization rotator device width, $W_{TM} - W_{res}$ are shown in Fig. 4.31. To study the fabrication tolerances of the device, the height of polarization rotator waveguide equal to 260 nm, and separation S = 200 nm, at W_{TE} = 353 nm have been considered for various waveguide widths, W_{TM}.

It can be seen that as W_{TM} reduces, the modal coefficient of the transmitted quasi-TM (H^x_{11}) polarized fundamental mode, C_x, reaches maximum value of 0.76 at W_{res} = 577 nm and reduces to 0.08 at W_{TM} = 537 nm, where the hybridness is low. On the other hand, at W_{TM} = 617 nm, C_y reaches a maximum value of 1.0473 while for the same width of the waveguide, C_x is approached a minimum point at 0.0744. It can be observed that with ± 30 nm deviations from the resonance width, 43 % and 86 % of the modal coefficient of the transmitted fundamental modes C_y and C_x respectively will occur.

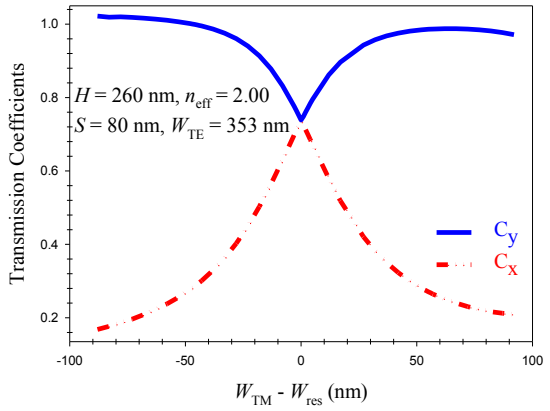

Fig. 4.32 The transmitted modal coefficient C_x, C_y with the width, $W_{TM} - W_r$ for the waveguide.

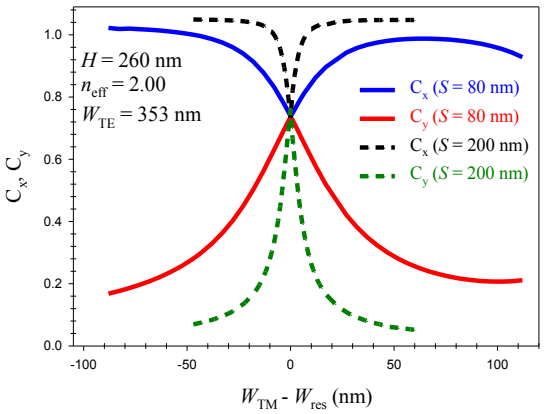

Fig. 4.33 The transmitted modal coefficient C_x, C_y with the width, $W_{TM} - W_r$ for the waveguide.

The variations of these two modal coefficients with the polarization rotator waveguide ($W_{TM} - W_{res}$) are shown in Fig. 4.32. To study the fabrication of the device, the height of polarization rotator waveguide equal to 260 nm, and effective index 2.00, separation S = 80 nm, at W_{TE} = 353 nm have been considered for various waveguide widths, $W_{TM} - W_{res}$. It can be seen that as W_{TM} reduces, the modal coefficient of the transmitted H^x_{11} polarized fundamental mode C_x reaches a maximum value of 0.736 at W_{TM} = 593 nm and then reduce to 0.20688 at W_{TM} = 695 nm. It is also shown that the modal coefficient of the transmitted quasi-TE (H^y_{11}) polarized fundamental mode, C_y, reaches its minimum value of 0.7388 as W_{TM} reduces to 593 nm.

Also this figure shows that important of the transmitted coefficient are found for a deviation of ± 85 nm from the resonance point for separation of the 80 nm, which are covered by 40 % and 75 % of the fundamental modal coefficient modes, C_y and C_x respectively.

Variation of these two coefficients with the 2nd waveguide width are shown in Fig. 4.33, for two different separations, for S = 200 nm shown by two dashed lines and for S = 80 nm, shown by two solid lines. Here, in the horizontal axis instead of W_{TM}, it is used $W_{TM} - W_{res}$, to study the effect of fabrication tolerance, where W_{res} was the phase matching resonating width.

It should be noted that for different waveguide separation, the phase matching width, W_{res}, were slightly different. When the W_{TM} is low and far away from the phase matching an incident quasi-TE (H^y_{11}) mode does not excite two polarized supermodes equally.

In this case, the magnitude of the quasi-TE (H^y_{11}) mode (given by C_y) is nearly one and magnitude of the quasi-TM (H^x_{11}) mode (given by C_x) is nearly zero.

However, when the waveguides are phase matched, these two supermodes are highly hybrid, then the magnitudes of the two polarized modes are nearly equal. Their values are nearly 0.707 = √2, indicating that each of the supermodes is carrying half power. By carefully observing the supermodes, it can be stated that a quasi-TE (H^y_{11}) mode in guide one, which has dominant H_y field in 1st guide will excite two supermodes, and they must have similar magnitudes so that H_y field in 1st guide adds up but H_x fields in 2nd guide will cancel to match the input quasi-TE (H^y_{11}) mode in the isolated input 1st guide. It can also be noted that when separation is smaller, the variation of C_y and C_x are less sensitive with the waveguide change. Reflections from both the butt-coupled interfaces were small, with the reflection coefficient less than 1 %.

4.10.2 Performances of the device on the polarization conversion:

At the start a quasi-TE mode with smaller hybridness supported by left guide, W_{TE}, is coupled to the one guide of the directional coupler section as shown in Fig. 4.29.

As the modes can be highly hybrid or can be equally or unequally distributed over two coupled waveguides, here we have used a notation to identify the polarized powers. The power associated with H_x or E_y field is identified as P_x and similarly power associated with H_y or E_x as P_y. These values are numerically integrated over left or right waveguides.

Along the polarization rotator, the power P_y of the TE polarized mode incident at the junction between two interfaces and most of the power will be converted into TM polarized mode as a P_x at the end of this section. However there may remain some power from P_x ; here this normalized residual power P_y is referred to as polarization cross-talk.

If the length of the directional coupler section is taken as L_c, then at this distance two excited supermodes would be out of phase and their vector addition will cancel the H_y field in first waveguide let guide with width, W_{TE}, and add up the H_x field in guide 2 or right guide with width, W_{TM} to yield a polarization rotated H^x_{11} mode in guide 2. From the modal coefficients shown in Fig. 4.33, and their full vectorial mode profiles polarized power in each waveguides can be calculated.

The variations of the polarization conversion with W_{TM}, for the H = 300 nm is shown in Fig. 4.34, when W_{TE} = 330 nm, n_{eff} = 2.00, and separation is kept in 80 nm.

The fraction of TE power converted to TM polarized power conversion as a P_x is shown by a solid line. The amount of TE power remain unconverted in P_y power is shown by a dashed line. It can be clearly seen that, as W_{TM} increases from 160 nm, the normalized power conversion of TE, to the TM polarized power, reaches a maximum value of 0.976 at W_{TM} = 225 nm, and then reduces as W_{TM} increases further. With ± 5 nm tolerance from the maximum power conversion at the optimum width, the power conversion is found to be 0.880 when W_{TM} = 220 nm and 0.820 when W_{TM} = 230 nm and this shows that the polarization

conversion only decreases by about 10 % for a deviation of ± 5 nm from the desired optimum width.

The variations of the polarization conversion and cross-talk with the polarization rotator device width, W_{TM} is shown in Fig. 4.35. For this design, the device height and separation equal to 260 nm, and 200 nm respectively, are considered and also W_{TE} was fixed at 353 nm. It can be seen that as the waveguide width $W_{TM} - W_{res}$ increases from – 40 nm, polarization cross-talk starts to decrease and reaches a minimum value, at W_{TM} = 577 nm in optimum length, equal to -18.0 dB, as the width starts to deviate away from width of minimum cross-talk value of – 0.31 dB at W_{TM} = 620 nm. It is again shown that with ± 6 nm at the optimum length point, 99 % of polarization conversion (TE to TM) will occur and that the cross-talk values are found to be -1.575 dB and -1.70 dB when the widths of TM mode are at 583 nm and 571 nm, respectively.

The variations of polarization conversion with the waveguide $W_{TM} - W_{res}$ for the height of device 260 nm, effective index of 2.00, W_{TE} = 353 nm and S = 80 nm is shown in Fig. 4.36. It can be clearly seen that as W_{TM} increases from $W_{TM} - W_{res}$ = - 90 nm (W_{TM} = 507 nm), the normalized power conversion of TE (P_y) to TM (P_x) reaches a maximum value of 0.9886 (-0.0496 dB) at W_{TM} = 593 nm and then reduces as W_{TM} increases further. With ± 5 nm tolerance from the maximum power conversion at the optimum point width, the power is found to be 0.946825 when W_{TM} = 588 nm and 0.972035 when W_{TM} = 598 nm, which shows that the polarization only decrease about 4% for a deviation of ± 5 nm from the desired optimum width.

Along the polarization rotator device, the power P_y of the TE polarized mode incident at the junction between two interfaces, and most of the power will be converted into TM polarized mode P_x at the end this section. However, there may remain some power from p_y; here, this normalized residual power P_y is referred to as cross-talk.

In this study, the cross-talk is defined as the unwanted polarized power, normalized to the total input power, which remains at the end of the polarization rotator device. It is again shown here that at this 593 nm optimum width, the cross-talk reaches a minimum value of – 19.45 dB, which a very low value. However, with ± 5 nm deviation from the optimum width, the cross-talk values are – 15.55 dB and – 13.85 dB when the widths of quasi-TM (H^x_{11}) mode are at 598 nm and 588 nm, respectively.

Variations of the TM polarized power with H_x field in guide 2 and TE power with H_y field in guide 1 with the changes in waveguide width are shown in Fig. 4.37. In this case, instead its variation with the waveguide width, changes with the deviation from the idealized design are shown to study of the fabrication tolerances simultaneously.

It can be observed that the maximum conversion for S = 200 nm, and 80 nm, shown by dark green dashed and blue solid lines are about 0.985 and 0.99, respectively.

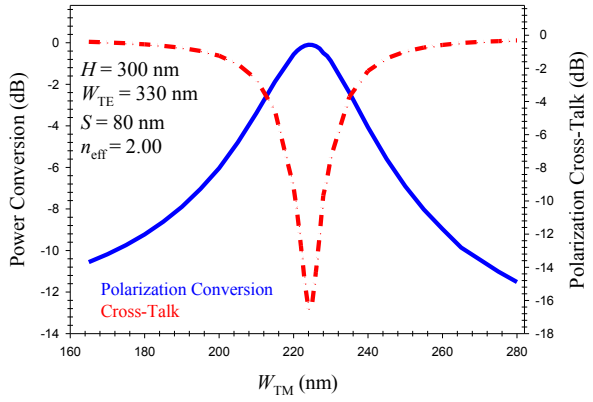

Fig. 4.34 Variations of the polarization conversion, and polarization cross-talk with 2nd waveguide width, W_{TM}.

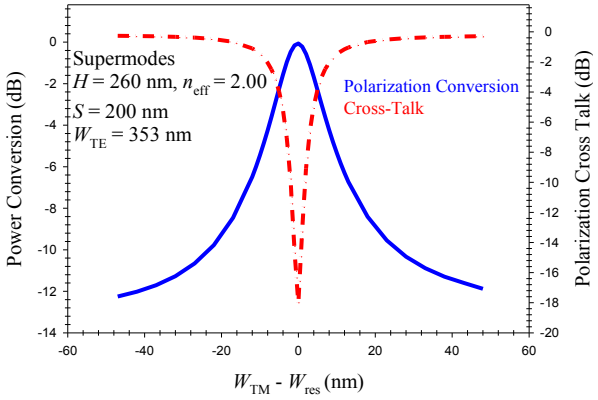

Fig. 4.35 Variations of the polarization conversion and polarization cross-talk with the waveguide, $W_{TM} - W_{res}$.

The amount polarized power amount polarized power remains unconverted is shown as cross-talk (C.T). It is shown here that for separation S = 200 nm, and 80 nm, shown by a black dased-dotted line and a red dashed line, respectively, demonstrate that C.T is better that –18.0 dB for both the cases.

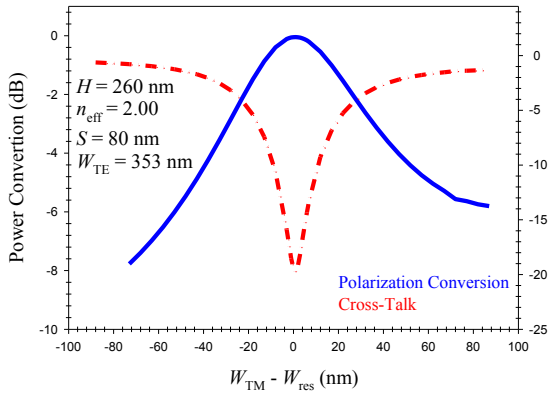

Fig. 4.36 Variations of the polarization conversion and the polarization cross-talk.

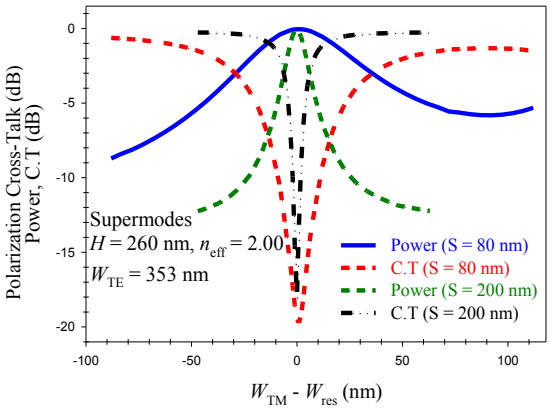

Fig.4.37 Variations of the polarization conversion and the polarization cross-talk with the width tolerance, $W_{TM} - W_{res}$.

4.10.3 Effect of fabrication tolerances in power conversion:

The curves above show the maximum polarization conversion and polarization cross-talk with the possible width variations, but still assumed to have the correct coupling length. But, in practice the fabrication errors cannot be anticipated so, the device length would be the same as originally designed even when the width deviation may appear.

A study of how the fabrication tolerance on waveguide width, affect the power conversion and corresponding cross-talk at specified positions along the propagation direction, Z, has been carried out.

In this case as the coupling length will also change with the width variation, and next combined effect of these is also simulated.

Variations of polarization conversion with the waveguide width W_{TM} is shown in Fig. 4.38. To study the fabrication of the device, the height of polarization rotator waveguide equal to 260 nm, and separation S = 200 nm, at W_{TE} = 353 nm have been considered for various waveguide widths, W_{TM}.

The variations were studied in two cases. One was varied device length at exact L_π and the other was fixed at optimum length which was 170 μm. In this case, equal to the coupling length at the optimum design. The solid line shows the exact L_π while the dashed line represents fixed L_c at 170 μm. As width of waveguides, in quasi-TM (H^y_{11}) mode varies, the device is fabricated at optimum point, polarization conversion decreased sharply compared to exact L_π. This sharp reduction occurred at10 nm deviation from resonance point at ratio for optimum length to the device length equal 2. While, the value of polarization conversion at optimum point of waveguide width equal to 577 nm is the same for the two cases equal to 0.984. The trend for optimum device length followed a symmetrical regular fluctuation with on offset of ± 6 nm in waveguide, W_{TM}. The ratio of optimum device length to exact L_π device length is numeral order determined the points at which oscillation happened and by the time it is damped. As it is seen this trend is exactly enveloped by the trend of varied device length.

The numerically simulated results are shown in Fig. 4.39 for various waveguide widths, W_{TM}, ranging from 165 nm to 280 nm. Here, the optimum device length was fixed at 142 μm, because this length correspond to the ideal design condition to obtain maximum power conversion. The converted quasi-TM (H^x_{11}) power, P_x, at their corresponding L_π values, increases from – 11.0 dB to the maximum value of – 0.1 dB, when the width increases from 165 nm to 225 nm, and then power decreases up to – 11.5 dB with further increase of the width to 280 nm. It can be seen that if the device is fabricated with a fixed device length of 142 μm, then as the waveguide width, W_{TM} varies; power conversion (P_x) will be very much lower than that at exact L_π, except at W_{TM} = 225 ± 5 nm. At W_{TM} = 225 nm, the L_π matches with the exact fabricated device length, therefore giving highest conversion and also lower cross-talk of – 16 dB (but not shown here). It can be noticed that, during of the fabrication the width, W_{TM} of the uniform sections can be controlled within 225 ± 5 nm, then the loss of the power conversion would be about 0.6 dB.

Variations of the real polarization conversion for two different waveguide separations, S are shown in Fig. 4.40. It can be observed the variation of polarization conversion is not monotonic as width is increased or reduced but shown with a periodicity. This is due to the effect of change in the coupling length. The length of the PR section is taken as the coupling length at the ideal design condition, Z at the resonating case. But when width deviates from the design width, its coupling length reduces, which cannot be anticipated.

When even multiple of this coupling length equals to the device length, all the polarized light reconverts to the original input polarization state, and overall polarization conversion will be zero, as shown here. The zero conversions are related to the case when the modified

coupling length (due to fabrication error) is $2m$ times smaller than the originally designed length considered for this polarization rotator when m is an integer. It can be observed that, for with S = 200 nm as shown by red dashed-dotted curves, even a small change of 10 nm in the width the resulting polarization conversion can drop to zero, and this would be very difficult to control. On the other hand, for S = 80 nm, shown by a solid blue line, polarization rotation drops to zero only when ΔW is ± 45 nm, as in this case coupling length becomes half. However, for ΔW = ± 10 nm, the polarization rotation will be 85 %, which could still be acceptable as a practically achievable and a viable design.

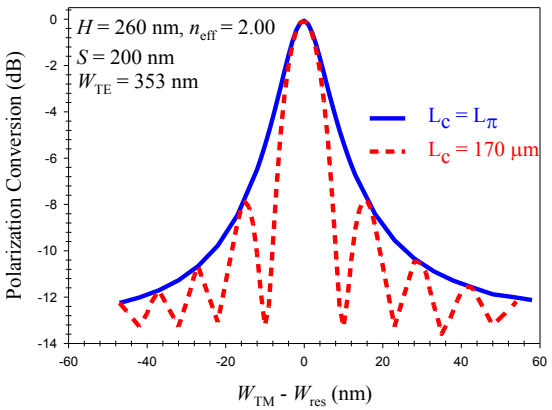

Fig. 4.38 Variations of the converted power P_x at $Z = L_\pi$, and Z = 170.0 µm, with the waveguide width $W_{TM} - W_{res}$.

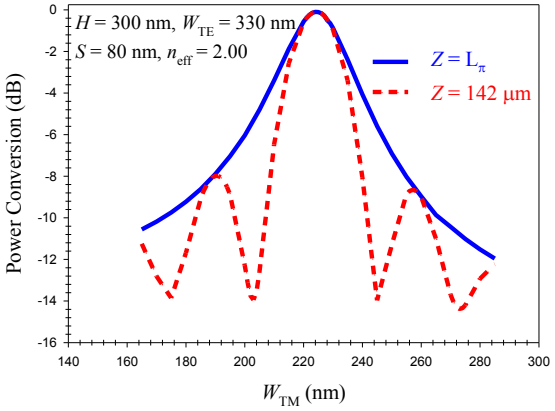

Fig. 4.39 Variations of the converted power P_x at $Z = L_\pi$, and Z = 142.0 µm, with the waveguide width W_{TM}.

Figure 4.41 compares the variation of the cross-talk at exact L_π and optimum device length, respectively shown by solid and dashed-dotted lines. It is indicated that at optimum point the cross-talk for both trends are the same, which is -18.1 dB (0.0156). For a width tolerance ± 10 nm the value of cross-talk for L_c = 170 µm exceeded the corresponding exact L_π value – 1.25 dB, However, further they reached unity value.

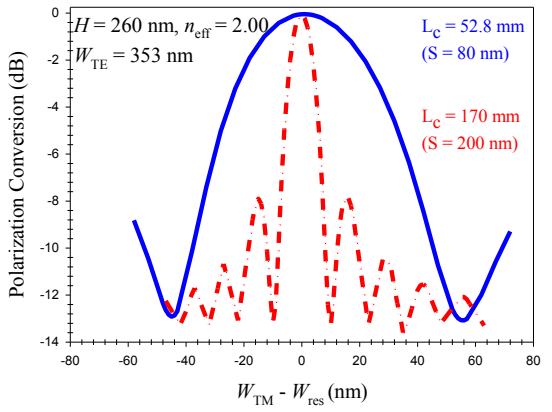

Fig. 4.40 Variations of the converted power P_x at Z = 52.8 µm and Z = 170 µm, with the waveguide width $W_{TM} - W_{res}$.

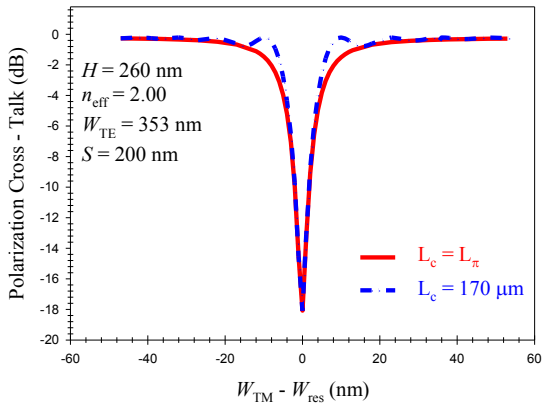

Fig. 4.41 Variations of the polarization cross-talk at $L_c = L\pi$ and Z = 170 µm, with the waveguide width W_{TM}-W_{res}.

4.11 Band-width performance on the device parameters:

Next, performance of the polarization rotator, when the operating wavelength varies from 1500 nm to 1630 nm, was investigated.

Figure 4.42 shows the variation of the hybridity and L_c with the operating wavelength, λ. It can be seen that the wavelength is reduced; initially hybridity reduces slowly with the wavelength and then reaches a minimum value of 0.8208 at λ = 1585 nm, then increases from 1585 nm to 1505 nm, and reaches its maximum value about 1.00 at λ = 1505 nm. Device length, L_c also decreases as λ increases giving a minimum L_c of 32.3 μm at λ = 1630 nm. Also, the value of L_c only shows a change of only 45 μm over the whole wavelength range considered.

The modal coefficients C_x for quasi-TM (H^x_{11}) and C_y for quasi-TE (H^y_{11}) modes with the operating wavelength, λ were obtained by employing the LSBR method in Fig. 4.43. It can be seen that at λ = 1630 nm, C_y is 0.744 and as wavelength is reduced, it reaches a minimum value of 0.72921 at λ = 1580 nm. On the other hand, at λ = 1630 nm, C_x is 0.7171and it reaches a maximum value of 0.744 at λ = 1570 nm, and C_x shows a reduction from 0.744 nm to 0.66433 nm, throughout the reduction from 1570 nm to 1500 nm.

Next, the effect of operating wavelength variation on the performance of the polarization rotator is studied. Although, as the wavelength changes, coupling length also changes and this will also change the Phase- matching conditions, however, in this design, as the waveguide separation was very small, coupling was strong, the effect of small change in the wavelength is almost negligible, as shown here; this suggests the devices will have a large operating bandwidth.

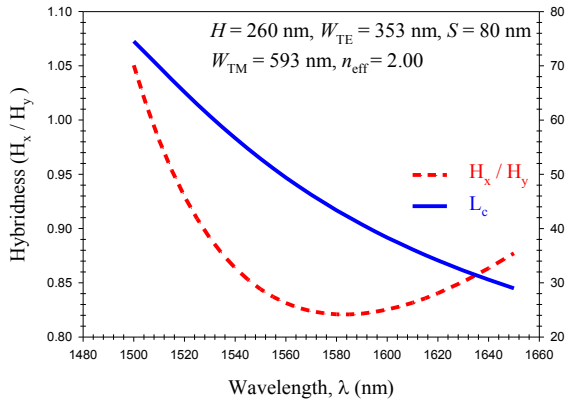

Fig. 4.42 Variations of the hybridness and coupling length, L_c with the operating wavelength, λ.

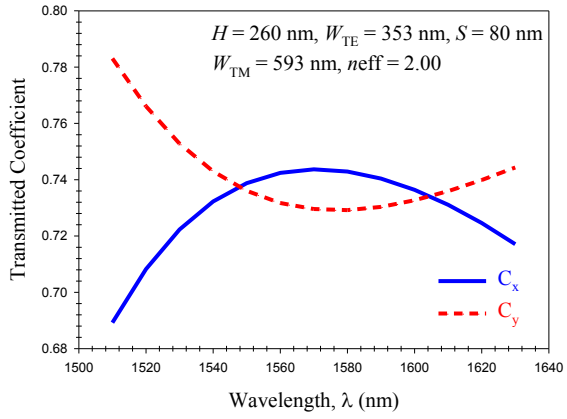

Fig. 4.43 Variations of the transmission coefficients, C_x, and C_y with the operating wavelength, λ.

The effect of temperature variation has also been studied at but this is not shown here. It was identified that a small amount of temperature tuning can be possible, which can be used to compensate fabrication tolerances, but this tuning range is rather very small. Similarly, the previous figure indicates a small amount of wavelength tuning can also be used to compensate the fabrication tolerances.

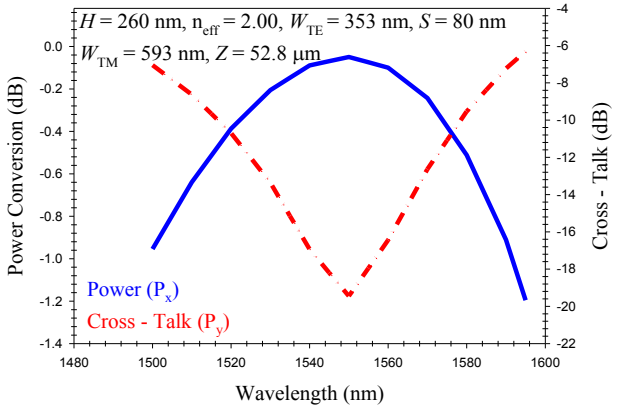

Fig. 4.44 Variations of the polarization conversion and polarization cross-talk with the operating wavelength.

4.12 Summary:

In chapter 4, various designs of passive polarization rotators have been investigated. Numerical simulations have been obtained using the rigorous full vectrorial based Finite Element method. Initially, it was demonstrated that the optical waveguides without symmetry are particularly suitable to increase the hybrid nature of the fundamental modes, thereby increasing the overlap between the polarization states. By using the versatile VFEM approach, the asymmetrical directional coupler of the waveguide were presented exactly.

The design presented here uses two simple silicon nanowires, which would be simpler than the design approaches reported earlier by using slot waveguides [174-177]. As this structure does not consider any bend section or slanted side wall [145-147] or trench with different etching depth [148].

Through a detailed numerical study, a novel design of a compact SOI polarization rotator incorporating polarized coupling between two unequal width waveguides is reported here. The above results suggests that an appreciable short 52.8 μm long PR can be designed for 1.55 μm wavelength by exploiting the phase matching between the two orthogonally polarized modes of these two guides.

A detailed study of the fabrication tolerances of a compact passive, silicon nanowire polarization rotator has been presented, by using rigorous numerical tools based on the VFEM method and the LSBR method. Maximum power coupling efficiency of 99 % is possible from input quasi-TE (H^y_{11}) mode to output quasi-TM (H^x_{11}) mode, with cross-talk better than – 20 dB and loss value lower than 0.1 dB. Fabrication tolerances of the designed structure were studied by varying different WG parameters and it has suggested that, a part of it may be corrected through appropriate temperature tuning or by wavelength adjustment.

Thus, this high conversion efficiency, low footprint, simpler design, along with the existence of well-matured fabrication technologies for SOI structures, should make our

proposal attractive for making an on-chip polarization rotator for their potential deployment. This design should be relatively easy to implement for fabrication and can be made with a single mask. It is also shown here that operating bandwidth of these PR is considerable wider and suitable for WDM applications.

Design of a Compact Polarization Splitter by Using Identical Coupled Silicon Nanowires

5.0 Introduction:

Optical systems incorporating rotationally symmetric optical fibres cannot maintain its polarization states as it encounters random bends, pressures, or manufacturing imperfections which allow power transfer between two orthogonally polarized modes. For many communication and sensing systems this creates a major problem where a specific polarization state is needed. In this case, a polarization independent or polarization diversity system would be useful. TE/TM polarization splitters are important components for design and development of polarization diversity optical systems, such as polarization independent receivers for coherent detection [185], [186], integrated-optic gyroscopes [187], switches and modulators [188].

Instead of pursuing difficult polarization-independent devices on SOI, a polarization diversity scheme could be employed [189]. In this case, the orthogonal polarization components of the input light can first be split into two different waveguides by using polarization splitter (PS) [190]. A polarization rotator (PR) is then employed in one of the waveguides to rotate the polarization by 90° [191], [192]. Finally, for the rest of the photonic chip only one polarization has to be processed. Therefore, design of compact and efficient PS and PR are needed for separating and manipulating the polarization modes in a polarization diversity scheme [193].

Polarization splitters are increasingly being considered for use in optical communications, data storage, imaging and signal processing systems [194], especially as essential components for the realization of integrated–optical circuits for optical sensor and communication applications [195], where polarization plays an essential role.

5.1 Design of polarization splitters:

For the design of polarization splitter the polarization dependent modal properties are exploited. An optical waveguide with small index contrast the resulting modal birefringence is smaller. However, this modal birefringence increases for high index contrast waveguide such as silicon nanowires.

On the other hand, use of anisotropic materials, such as Lithium Niobate [196], or ion-exchanged glass [197], or InGaAsP-InP [198], and using of metal cladding [199] can enhance the modal birefringence. Several metal materials, e.g., gold, silver, copper, and aluminium, have also been studied and incorporated into the dielectric waveguides to generate large birefringence, which can effectively shorten the dimension of optical components. However, metal-clad waveguides are also inherently lossy. It has also been shown that instead of using

metal cladding by using simple layered isotropic material, material birefringence can also be introduced [200].

This modal birefringence can be exploited in the design of guided-wave polarization splitter, by incorporating y-splitter, directional coupler, Mach-Zehnder or MMI-based designs.

The designs of asymmetric asymmetrical y-splitter in highly anisotropic lithium niobate were reported by Masuda and Yip [196] and Wei and Wang [201], but as the angle is often less than 1°, the resulting device length is relatively large.

Among the possible designs, a popular approach is to exploit the polarization dependent coupling of directional coupler because of their simplicity and easy design and also reasonable performance. Modal birefringence of optical waveguides produces polarization dependent coupling length which can be exploited to design polarization splitter. Small material birefringence of GaAs was exploited to design a 3000 μm long PS [202]. Metal clad can introduce strong modal birefringence and Albrecht *et al*. Reported a 1600 μm long metal clad InP rib waveguide based asymmetrical directional coupler [203] and later on Rajarajan et al. Reported a more compact 230 μm PS [204]. On the other hand, silicon waveguide can directly provide stronger shape birefringence Yamazaki [205], and Kiyat *et al.* Reported an even more compact 120 μm PBS using silicon rib waveguide [190].

Polarization splitters have also been designed by exploiting polarization dependent imaging distance of multimode interference (MMI) couplers. In an earlier work, simple modal birefringence was considered for an InP based design where the PS length was 1640 μm [206] and later on a shorter much 1023 μm design was reported [207]. For a very narrow width MMI, supporting only two modes, which is also known as zero-gap directional couplers or two mode couplers, a short PS can be designed [208].

MZI structures have also been used for realizing PSs. In order to make a compact MZI PBS, a large birefringence is needed. One of the earliest work, Soldano et al. Reported [199], a 3300 μm Mach-Zehnder based PS using metal clad in one arm. Liang *et al*. [209] reported a 6000 μm long Mach-Zehnder design using natural modal birefringence of silicon rib waveguide and more recently Augustin *et al*. [210] reported a more compact 600 μm long design using higher waveguide birefringence silicon nanowires using MMI sections in MZI.

Recently there have been extensive research activities to develop silicon based photonics, by exploiting well developed CMOS technology. This can allow incorporation of both photonic and electronic components on the same chip. The high index contrast of silicon waveguides also allows more compact waveguides, bends and also other functional devices. But its modal characteristics are also strongly polarization dependent due to the strong index contrast. The dependence of the TE and TM polarization can be exploited to find the polarization splitting ratio in order to design a compact Polarization Splitter. Owing to the high-index-contrast at the dielectric interfaces, the normal electric field component has to be

discontinuous to satisfy the continuity condition of the electric flux density, leading to the higher amplitude and field enhancement.

Apart from strip silicon nanowires [211], silicon-based slot waveguides [212], where a low refractive index nanometer region placed between two high refractive index silicon nanowires, have been intensively investigated due to their unique properties and potential applications. It is noted that slot waveguides are also highly polarization-dependent, thus compact and efficient PS is greatly required for separating the polarization modes in polarization diversity schemes.

Recently, PSs based on horizontal single [213] and multi-slotted waveguide structures [214] have also been proposed. It is noted that slot waveguides are also highly polarization-dependent, thus compact and efficient PBS is greatly required for separating the polarization modes in polarization diversity schemes. Using an asymmetrical DC with a silicon wire, a PBS of 13.6 μm in length was demonstrated experimentally, using an asymmetrical DC with a silicon wire and a vertical slot, a PS of 13.6 μm in length was demonstrated experimentally [215]. Dai [216] and Fukuda *et al*. [217] have considered asymmetric directional coupler with a NW and slot waveguide, ignoring very long coupling length for TE mode compared to TM modes.

For instance, hybrid plasmonic waveguide (HPW), which confines mode within the low index gap between a metal and a high index dielectric, has already been introduced into the design of PS [218, 219, 220, 221]. In [218], a PBS based on three-guide structures, where a HPW was used as middle waveguide to achieve large birefringence, only allowing TM mode to evanescently couple to the cross port. The experimental results are shown that the coupling length is almost 6.5 μm. It appears that the performance should be further improved. In addition, multi-etch processes are required during the fabrication, which will increase the complexity and cost of fabrication.

Another possible way to make a short PBs is realized by polarization splitters incorporating waveguide bend [222], the polarization dependence of PhC and grating structures (e.g., ~50 μm [223], 20 μm [224] or out-of-plane grating (e.g.,~14 μm [225]). However, the design is usually quite complex, and fabrication is relatively difficult and also, the PhC and grating structures usually introduces a relatively large loss.

Silicon (Si) is the most mature material for electronics but a relatively newer material for photonics. The expensive compound semiconductor materials, such as GaAs or InP can provide light sources, but their low yield coupled with the higher assembly and packing costs, keep optical communication a costly technology today. Recently, it has been suggested [226] that silicon with silicon-on-insulator technology (SOI) can be considered to be material choice for designing and integrating dense PIC and optoelectronic integrated circuit (OEIC) devices. Refractive index contrast for a silicon nanowires (NWs) is high, its modal characteristics are strongly polarization dependent. The dependence of the TE and TM polarization is exploited here to find the polarization splitting ratio in order to design a compact Polarization Splitter.

The Si polarization splitter proposed here shows a very compact design without slanted side wall or bent. In this paper, design optimization of a Si polarization splitter based on SOI technology is presented which requires less complex fabrication process with single mask only and compatible with the mature CMOS technology which is backed by a well-established semiconductor industry [226].

The conversion of two polarized mode to the two separate polarized modes are realized by efficient power coupling between two coupling lengths from the quasi TE and TM polarized modes. Our goal here is to evaluate if a design relationship can be achieved such that the coupling length for the TE polarization coupling length is exactly twice that of the coupling length of the TM polarization.

The conversion of two polarized mode to the two separate polarized modes are realized by efficient power coupling between two coupling lengths from the quasi TE and TM polarized modes.

Our goal here is to evaluate if a design relationship can be achieved such that the coupling length for the TE polarization coupling length is exactly twice that of the coupling length of the TM polarization.

5.2 Theory of polarization splitters:

Pure TE and TM modes can only exist in planar slab WGs with 1D confinement. However, in all practical optical WGs with 2D confinement, the modes are classified as quasi-TE and quasi-TM modes, which contain all six components of the **E** and **H** fields. Besides that, in high index contrast silicon nanowires, the modal birefringence is much higher. To find all the three components of the **H**-field and the evolution of fully hybrid quasi-TE and quasi-TM modes along a guided-wave device all the methods to be used must be fully vectorial in nature. Accurate calculation of the modal solution for the fundamental quasi-TE and quasi-TM polarized modes are of great importance when designing a polarization splitter. In the design of a compact optical polarization splitter, a full vectorial method is needed to obtain modal solutions of the supermodes and modal field profiles of the constituent waveguides across the dielectric interface. In this regard, **E**-field based formulation has been considered; however, since normal component of the **E**-field is discontinuous around the interface, such an **E**-field based approach would require boundary conditions to be implemented and can be difficult for waveguides with arbitrary refractive index profile.

On the other hand, all the three components of the **H**-field components are continuous across the dielectric interfaces and becoming more popular and such a full-vectorial formulation used here, is based on the minimization of the following energy functional [105] in terms of the nodal values of the full **H**-field vector.

In this chapter, the above-mentioned attractive features of this method are utilized to optimize the polarization design especially in the TE/TM Ratio and device length calculations.

Although the FEM can be used to calculate the propagation constant for the even and odd in the fundamental quasi-TE and quasi-TM modes and also their modal field profiles, alone it cannot be used to analyze discontinuity along a guided-wave device or optoelectronic subsystem.

A full-vectorial beam propagation method (BPM) [226] can be used to calculate the power conversion between the two polarization states, however, as the proposed structure being consists of two discrete interfaces, a junction analysis method would be more efficient to use to find the excited modal coefficients at the butt-coupled junctions and also to find the resulting polarization splitter.

In this case a powerful, full-vectorial numerical approach, the Least Squares Boundary Residual (LSBR) method [184] has been used, which rigorously satisfies the continuity of the tangential electric and magnetic fields at the junction interface in a least squares sense, and 92btains the modal coefficients of the transmitted and reflected modes at the discontinuity interface.

The LSBR method looks for a stationary solution to satisfy the continuity conditions by minimizing the error energy functional, J, as given by [184]. This approach would be more rigorous yet computationally efficient than the use of the BPM. The polarization splitter proposed here is very compact design without a metal clad section or bent and less complex fabrication and also compatible with the mature CMOS technology, by using two simple coupled identical nanowires.

They are of equal height and identified by *H*, which would be easy to fabricate and also they have the same widths, given as *W*, and the separation between the waveguides is *S*.
For a directional coupler, its coupling length, defined as:

$$L_c = {}^{\pi}/_{(\beta_e - \beta_o)} \tag{5.1}$$

The L_c is the minimum length necessary for maximum energy transfer, where β_e and β_o are the propagation constants of the even and odd supermodes of the coupled structure. For most of the practical waveguides the coupling length for the quasi-TE and quasi-TM modes are different but for low-index contrast waveguides the difference is small. As stated earlier, for high index contrast this difference could be relatively larger or by using anisotropic material, or metal clad the difference can be further increased. For highly birefringent NWs the coupling length for quasi-TE or TM polarizations, L_c^{TE} and L_c^{TM} are significantly different. Thus if a relationship between the coupling lengths, L_c^{TE} and L_c^{TM}, for the TE and TM polarizations, respectively, can be established such that the device length, *L*, is given by:

$$L = m * L_c^{TE} = n * L_c^{TM} \tag{5.2}$$

where *m* and *n* are integer and when one of them is even and other one is odd, then two orthogonally polarized waves will emerge from two different output ports, as shown in

Fig. 5.1. This condition may not be very difficult to achieve, but often yields larger *m* and *n* values.

Performance error due to any fabrication tolerance is magnified by *m* or *n*, which often makes such design very sensitive to small changes in waveguide parameters. Here, the design target was to have *m* and *n* as small as possible, and for the best possible design to achieve $m = 1$ and $n = 2$.

Hence, we seek a design where, the coupling length for a quasi-TE (L_c^{TE}) polarization is twice that for quasi-TM (L_c^{TM}) polarization, if possible, allowing most of the quasi-TE and quasi-TM polarized powers emerge from two different ports.

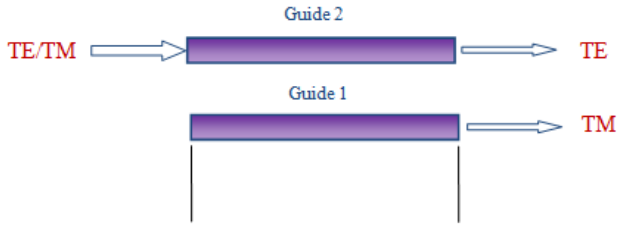

Fig. 5.1 Principle of a polarization splitter.

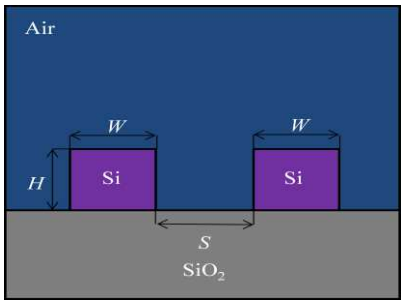

Fig. 5.2 Cross-section of coupled NWs.

5.3 Study of the H-field modal profile characteristics:

From using the **H**-field formulation, the modal amplitudes, field profile and propagation constants of the exited modes, the evolution of the power waveguides along the axial direction can be calculated.

Utilising of the rigorous finite element numerical method, the percentage of confinement power in each of the waveguides for the quasi-TE (H^y_{11}) and quasi-TM (H^x_{11}) supermodes in polarization state, can be analysed and also optimised for the polarization splitter design has been developed.

Near the phase-matching condition area, where a relationship can be derived such that two times the coupling length for the quasi-TM polarization equal to the coupling length of the quasi-TE mode, dominant TE (H^y_{11}) and /or TM (H^x_{11}) even and odd like supermodes fields are highly magnitude compare to the non-dominant, their field profiles of both the even and odd modes in quasi-TE modes will be illustrated.

Figure 5.3a shows the H_y field profile of the H^y_{11} even supermode, when $H = 200$ nm, $W = 350$ nm, and $S = 100$ nm. It can be seen that the guides are coupled and the even supermodes power is equally distributed in both the waveguides in the device, where the propagation constant of the even mode is slightly higher than those of the two isolated guides.

Variation of H_y along the horizontal direction (x) of the same supermode is shown in Fig. 5.3b. Here, it can be observed that, field amplitude are the same, which refer to Fig. 5.3a, shows that for this component fields also spread equally to the waveguides. On the other hand, figure shows that, signs of both the field profiles in the waveguides are the same.

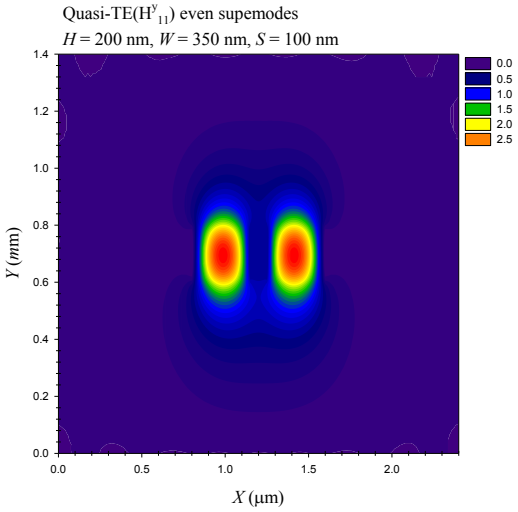

Fig. 5.3a H^y_{11} field profile for the quasi-TE even supermodes.

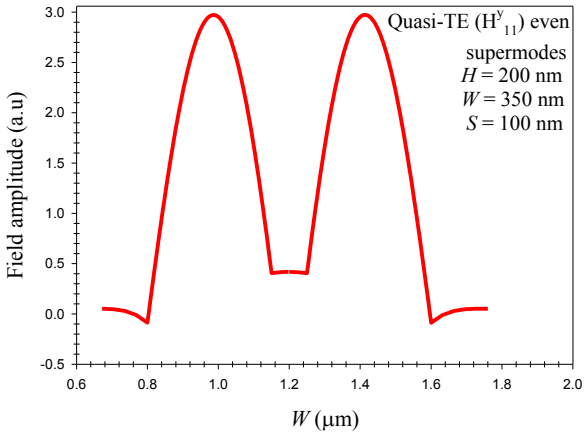

Fig. 5.3b The composite field profile for the quasi –TE (H^y_{11}) even supermodes.

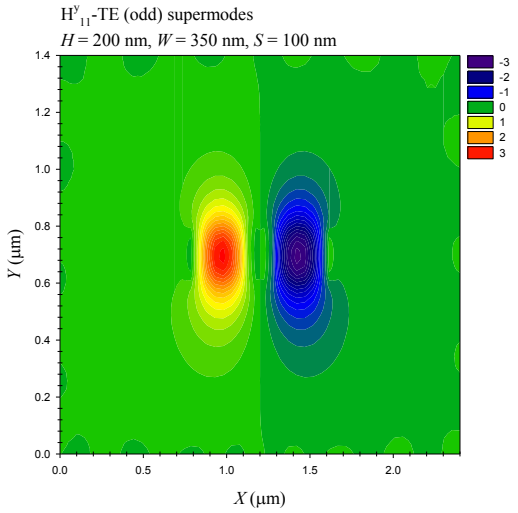

Fig. 5.4a H^y_{11} field profile for the quasi-TE odd supermodes.

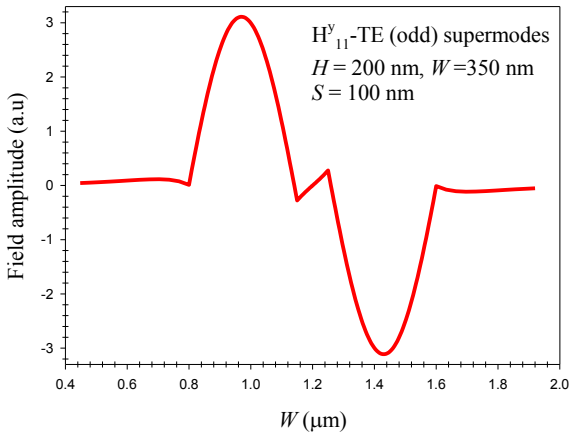

Fig. 5.4b The composite field profile for the quasi (H^y_{11}) – TE (odd) supermodes.

Vector H_y field profile and it variation along X of the TE (H^y_{11}) odd supermode are shown in Fig 5.4a and Fig 5.4b, for the height of 200 nm, width and separation are equal to 350 nm and 100 nm, respectively. In this case, the field is anti-symmetric and again the power confinements in both waveguides are the same. However, for this mode, magnitude of the waveguide fields are equal but of opposite sign, so its resulting is shown in negative amplitude of the waveguide in the left hand of the TE field profile in Fig 5.4a. Hence for both

even and odd supermodes, it can be observed that the sign of the even mode is the same, whereas in odd state modes, fields amplitude are opposite sign in the composite field profile.

5.4 Estimation of accuracy of the modal solutions:

The schematic cross-section of the coupled NWs is shown in Fig. 5.2. Here, the width and height of the NW are shown by *W* and *H*, respectively and separation between the cores is shown as *S*. The refractive index of the Si and Silica are taken as 3.4754752 and 1.4440236 at the operating wavelength of 1.55 μm. Here the symmetry conditions of the coupled structure have been exploited for the modal solutions of directional coupler. This not only avoids mode degeneration by separating two interacting modes, but also allow much improved solutions, with a given computer resources. Since this structure has one-fold symmetry, only half of the waveguide needs to be considered, which will allow a much finer mesh division to be used. The combinations of **n×H** and **n.H** at the vertical symmetry lines have been used to find the even and odd supermodes. From the modal solutions the coupling lengths for the quasi-TE (H^{y}_{11}) and quasi-TM (H^{x}_{11}) polarizations, L_c^{TE} and L_c^{TM}, can be calculated and subsequently these coupling lengths ratio can be calculated as:

$$R_{TE\text{-}TM} = L_c^{TE}\,(\mu m) / L_c^{TM}\,(\mu m) \tag{5.3}$$

Like all other photonic devices, its performance will also depend on the accuracy of the designs and also on the accuracy of the fabrication. Design accuracy will critically depend on the accuracy of the modal solutions. Besides this, a small change of the separation distance (or its width and height) will not only change the quasi-TE and quasi-TM coupling lengths but also the $R_{TE\text{-}TM}$, which will affect the performance and these are discussed in this chapter.

The optical propagation in a directional coupler can be expressed in terms of the propagation constants (β) of the even and odd supermodes of the coupled structures, or their effective indices.

Accuracy of the L_c depends on the accuracy of the modal solutions, and more particularly on their differences, and it is critical that the accuracy of these parameters is established first. As most of the key design parameters are often obtained by using a given numerical methods and it is also known that accuracy of these design parameters are also depend on the numerical parameters used, and as example, for the FEM the number of elements (or mesh divisions used) is the critical numerical parameter, and this is studied first.

Variations of the effective indices, n_{eff} of the fundamental quasi-TE (H^{y}_{11}) even and odd supermodes for a silicon nanowires with the mesh division is shown in Fig. 5.5. In this case, the waveguide Height (*H*), Width (*W*) and Separation (*S*), are taken as 220 nm, 400 nm, and 100 nm, respectively. For simplicity equal number of mesh divisions is used in both the transverse directions. Variations of the $n_{e\text{-}TE}$ (even) and $n_{e\text{-}TE}$ (odd) are shown by a blue solid line and a red dashed line, respectively.

It can be observed that when the number of mesh increases, effective indices of both the fundamental quasi-TE supermodes increase. It can be observed that, the effective index of quasi-TE even supermode is higher than that of the quasi-TE odd supermode and both reach their saturation points asymptotically. It should be noted that when a 200 * 200 mesh is used n_{eff} is accurate to 3rd decimal place, and the accuracy is increased to 4th decimal place when mesh size is increased to 800 * 800. From these modal solutions, coupling lengths of both quasi-TE and quasi-TM polarizations, L_c^{TE} and L_c^{TM}, respectively, can be calculated.

Variations of the coupling lengths for the fundamental quasi-TE and quasi-TM polarizations for H = 220 nm, W = 400 nm, and S = 100 nm with the mesh division are shown in Fig. 5.6. A blue solid and a red dashed line represent L_c of the quasi-TE and quasi-TM-polarizations, respectively. As can be observed from Fig. 5.6, that as the number of mesh is increased from 100 to 500, initially the L_c^{TE} (solid) increases rapidly, and with further increase of number of mesh, the L_c^{TE} reaches a stable values asymptotically, but for the L_c^{TM} curve (dashed) decreases exponentially as a number of mesh increases from 100 to 800, and reaches its stable value about 3.149 μm. Two separate scales are used for L_c^{TE} and L_c^{TM}, and it should be noted that changes in their values are rather small. It can be observed that L_c^{TM} variation is more stable with the mesh, and this is due to the fact that the fundamental quasi-TM (H^x_{11}) mode being close to its cut-off its variation with the waveguide's geometric and numerical parameters is small.

Variations of the effective indices, n_{eff} of the quasi-TE (H^y_{11}) even and odd supermodes for H = 280 nm, W = 300 nm and S = 150 nm with the mesh divisions used in both the transverse directions are shown in Fig. 5.7.

It can be observed that when the number of mesh increases, effective indices of both the fundamental quasi-TE supermodes also increase and reach their saturation points asymptotically. Figure 5.7 also shows that effective index of quasi-TE (H^y_{11}) even-supermode is higher than that of the TE odd-supermodes (two different scales are used).

From the modal solutions, the coupling lengths for the quasi-TE (H^y_{11}) and quasi-TM (H^x_{11}) polarization modes, L_c^{TE} and L_c^{TM}, are calculated for H = 280 nm, W = 300 nm and S = 150 nm, and their variation with the mesh division used are shown in Fig. 5.9. It can be observed that as number of mesh division increases the coupling length for both the polarized fundamental modes increases.

For the design of a polarization splitter the L_c ratio (R_{TE-TM}) is calculated from the polarised coupling lengths, L_c^{TE} / L_c^{TM}. Variation of this coupling length ratio (R_{TE-TM}) for H = 220 nm, W = 400 nm and S = 100 nm with the mesh division is shown in Fig. 5. 9. It can be noticed that as the number of the mesh division is increased, initially this ratio increases appreciably and then converges to its stable value. It can be noted that L_c ratio (R_{TE-TM}) is accurate up to the second decimal point when 800 * 800 mesh divisions are used.The modal characteristics of the devices were analysed. The coupling length, L_c, for quasi-TE (H^y_{11}) and quasi-TM (H^x_{11}) modes of the PS structure were calculated using the equation (5.1), where the propagation constants were obtained using the full vectorial modal solution approach.

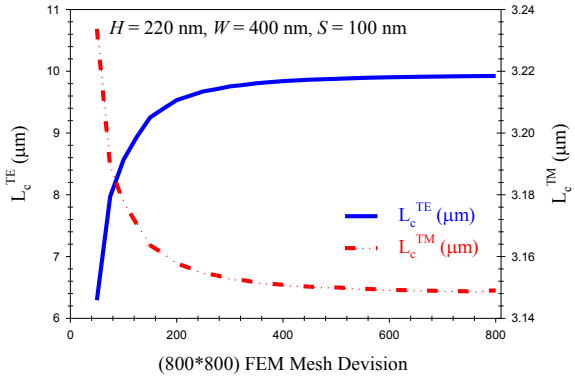

Fig. 5.5 Variation of the effective indices for the quasi-TE even and odd like modes with the mesh.

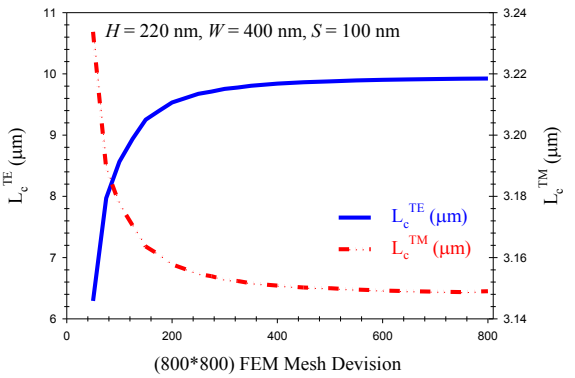

Fig. 5.6 Variation of the coupling lengths for the TE and TM polarization with the mesh.

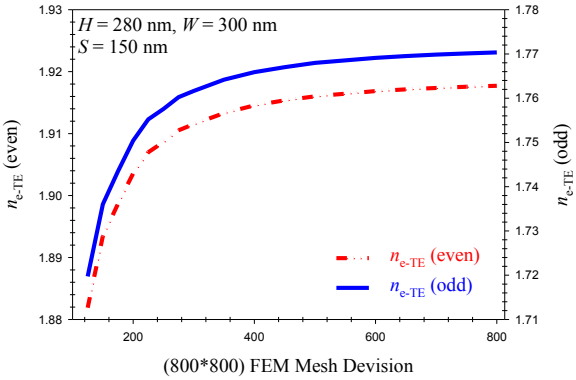

Fig. 5.7 Variation of the effective indices for the quasi-TE even and odd modes with the mesh.

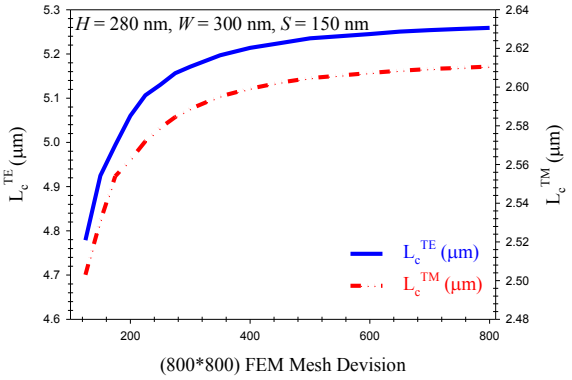

Fig. 5.8 Variation of the coupling lengths for the quasi-TE and quasi-TM polarization with the mesh.

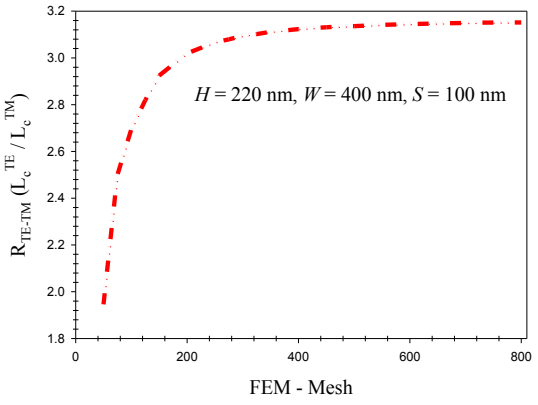

Fig. 5.9 Variation of the coupling length ratio of the quasi-TE and quasi-TM supermodes with the mesh.

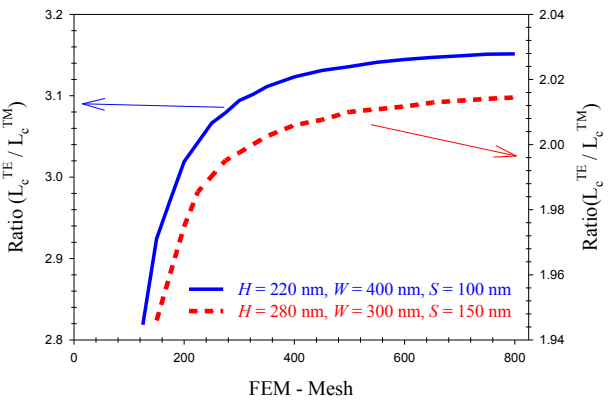

Fig. 5.10 Variation of the coupling length ratio of the quasi-TE and quasi-TM supermodes with the mesh.

Fig. 5.10 shows the variation of the ratio L_c^{TE} / L_c^{TM} with the mesh division for two different designs. It can be noted that the ratio (R_{TE-TM}) increases with the mesh size, following exponentially and then converge to the saturation points. It should be noted here that ratio (R_{TE-TM}) with the mesh division, for the height of 220 nm, W = 400 nm, and S = 100 nm is consistently higher than the height of 280 nm, W = 300 nm, and S = 150 nm.

Following this all the numerical simulations are carried out using equivalent to or better than 800 * 800 mesh divisions in the two transverse directions, where more than 1.2 million first-order triangular elements have been employed to represent the half of the waveguide structures.

5.5 Analysis of the optimal design parameters:

Here, design optimization of a compact optical polarizer is presented in order to study the effect of key fabrication parameters, such as the guide width, guide height and guide separation on the coupling lengths and power transfer characteristics.

Variations of the device coupling lengths, L_c^{TE}, and L_c^{TM} of the quasi-TE (H^y_{11}) and quasi-TM (H^x_{11}) supermodes for H = 280 nm, and S = 150 nm with the waveguide width used in both the transverse directions are shown in Fig. 5.11.

It can be observed that when the width of the waveguides decreases from 380 nm to 230 nm, coupling length of the quasi-TM (H^x_{11}) mode, L_c^{TM} also decreases as almost linear curve, from 4.643 µm to 1.80 µm, respectively.

On the other hand, as width of the waveguides increases, the device length, L_c^{TE} initially reduces and reaches its minimum value before it starts to rise (the left-hand Y-axis scale). The minimum length is achieved when W = 265 nm, where the L_c^{TE} (min) value is 2.77 µm. This also shows coupling length for the quasi-TE mode is more sensitive compare to the quasi-TM mode.

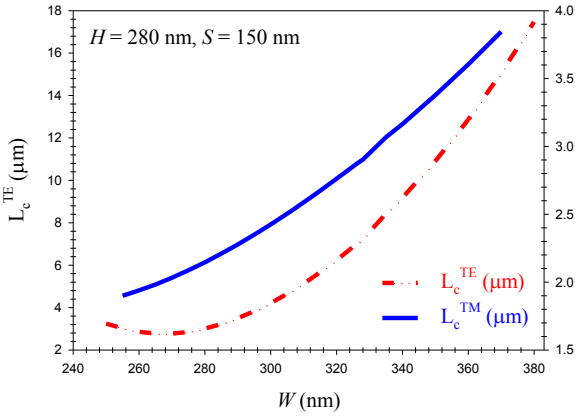

Fig. 5.11 Variation of the coupling lengths with the waveguide width, W.

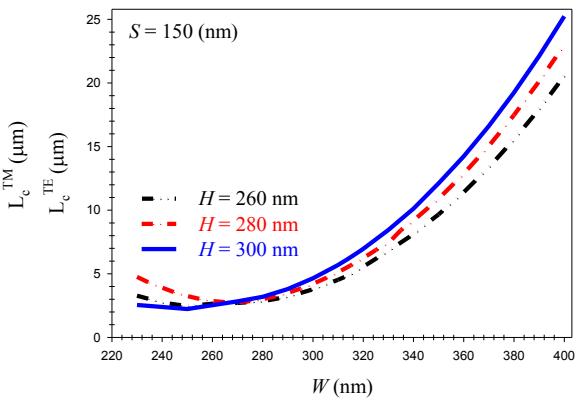

Fig. 5.12 Variations of the quasi-TE (H^y_{11}) coupling length with the waveguide width, for the different heights, H.

Figure 5.12 shows the evolutions of the device lengths with the waveguide width for different height, *H*. It was observed that as *W* decreases, its L_c^{TE} decreases until it reaches its minimum value and then starts to increase as it approaches its cut-off region. In this case when *H* = 260 nm, 280nm and 300 nm, the waveguide width, *W*, to be 265 nm to get the common value of L_c^{TE} = 2.77 µm. It can be clearly seen that for *H* = 300 nm, the device length is higher than that of 260 nm height.

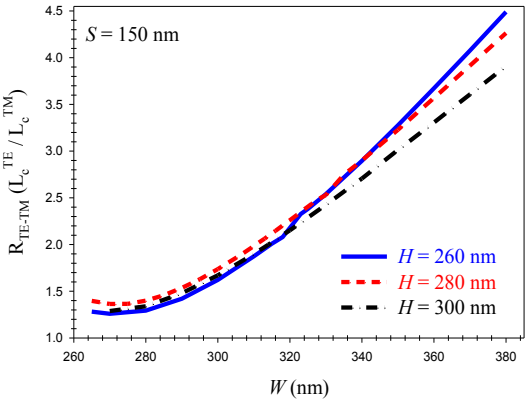

Fig. 5.13 Variations of the coupling length ratios of the quasi-TE (H^y_{11}) and quasi-TM (H^x_{11}) supermodes with the waveguide width for different heights.

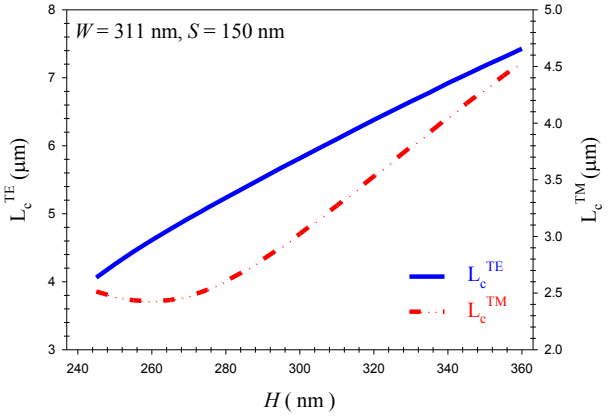

Fig. 5.14 Variations of the coupling lengths with the waveguides heights, *H*.

Variations of the $R_{TE\text{-}TM}$, with the waveguide width for three different heights, 260 nm, 280 nm and 300 nm, are shown in Fig. 5.13 by a solid blue line, a red dashed line and a black dash-dotted line, respectively with the same separation *S* = 150 nm. It can be noticed that as the waveguide width increases, the $R_{TE\text{-}TM}$, also increases. It can be noted that it is possible to obtain an ideal $R_{TE\text{-}TM}$ = 2.00, when quasi-TE (H^y_{11}) and quasi-TM (H^x_{11}) modes can emerge from two different ports. However, care must be taken to make sure that the numerically simulated results are accurate. For *H* = 260 nm, 280 nm and 300 nm, when $R_{TE\text{-}TM}$ = 2.00 is achieved then the corresponding waveguides widths would be 315 nm, 311 nm and 314 nm, respectively and for these three cases the device lengths would be equal to 4.940 µm, 5.235 µm and 6.180 µm, respectively. It can be noted that for *H* =260 nm, there is a small discontinuity in the $R_{TE\text{-}TM}$ curve, which was identified as the point where quasi-(H^x_{11}) and quasi-H^y_{21} modes are degenerate.

Variations of the coupling lengths as a function of the waveguide heights for the quasi-TE (H^y_{11}) and quasi-TM (H^x_{11}) polarizations are shown in Fig. 5.14 by a solid blue line and a red dash-dotted- dotted line, respectively. The quasi-TE and TM coupling lengths are shown with two different scales. The coupling length for quasi-TE, L_c^{TE} polarization shown by using the left-hand *Y*–axis shows a usual near linear variation of the coupling length. This is because, the reduction in height increases evanescent field outside waveguide core and coupling length reduces.

Variation of the quasi-TM coupling length is shown by using its right-hand Y-axis. Here, it can be observed that as the waveguide height is reduced, initially L_c reduces slowly with the

height and then increases slowly. The non-monotonic change of the L_c^{TM} has been identified to the modes approaching its cut-off condition when the Height, *H*, was considerably lower.

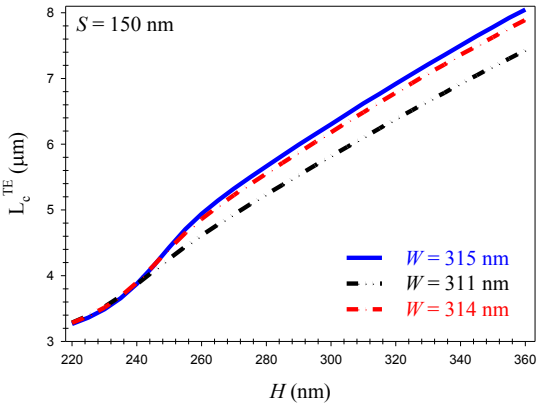

Fig. 5.15 Variations of the coupling length of the quasi-TE (H^y_{11}) supermodes with the waveguide heights, for the different widths.

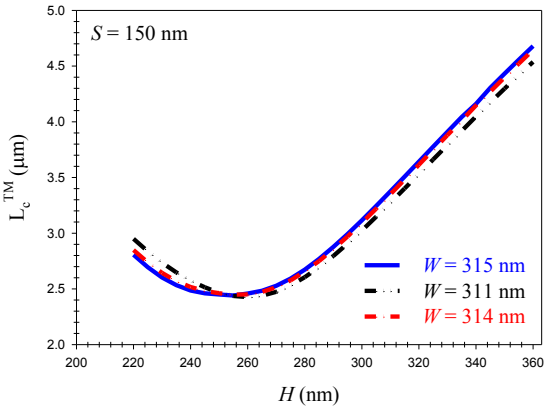

Fig. 5.16 Variations of the quasi-TM (H^x_{11}) coupling length with the waveguide height, for the different widths, *W*.

Variations of the quasi-TE (H^y_{11}) coupling lengths, L_c^{TE}, with the waveguide height for three different waveguide widths, 311 nm, 314 nm, and 315 nm, are shown in Fig. 5.15 by black dashed-dotted-dotted line, red dashed-dotted line, and solid blue line, respectively.

It can be noticed that as the height of waveguides decrease, initially L_c^{TE} decreases with the height and then reach their cut-off points, and near the 250 nm mixed up.

The variations of the quasi-TM (H^y_{11}), L_c^{TM} coupling length with H are shown in Fig. 5.16. It can be observed that as *H* reduces to a minimum value and any further reduction of the height of waveguide, results rise in the L_c^{TM} as the modes approach their cut-off points. It can be noticed that for *W* = 311 nm, its minimum L_c^{TM} is at 2.4256 µm at *H* around 260 nm. It was recorded that for both *W* = 314 nm and 315 nm the minimum coupling length was at *H* = 255 nm at L_c^{TM} = 2.444 µm. It can be noted that all the L_c^{TM} values are very similar when *W* is large but it is only slightly lower for the *W* = 311 nm.

Variations of the $R_{TE\text{-}TM}$ with the waveguide height are shown in Fig. 5.17 by a blue solid line for *W* = 315 nm, a dash-dotted red line for *W* = 314 nm and a dashed black line for *W* = 311 nm (but for the same *S* = 150 nm), respectively.

From Fig. 5.17, a design relationship can also be achieved such that the coupling length for the quasi-TE polarization is exactly twice that of the quasi-TM polarization. The non-monotonic change of the L_c ratio has been identified to the modes approaching their cut-off conditions when the height, *H*, was considerably lower.

Variations of the coupling lengths in quasi-TE (H^y_{11}) mode in terms of the separation between the waveguides are shown in Fig. 5. 18 for three waveguide heights, 260 nm, 280 nm, and 300 nm, with corresponding waveguides widths, 315 nm, 311 nm, and 314 nm, respectively.

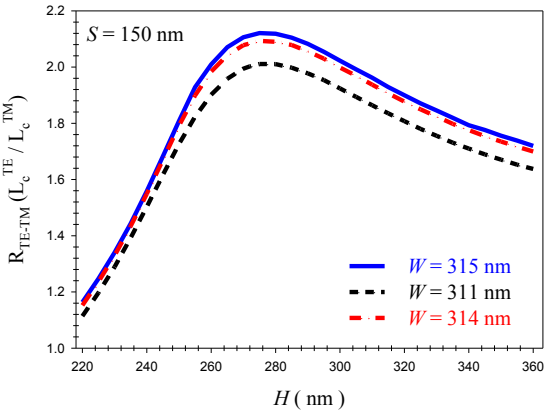

Fig. 5.17 Variations of the coupling length Ratio, R_{TE-TM}, with the waveguide height for the different widths.

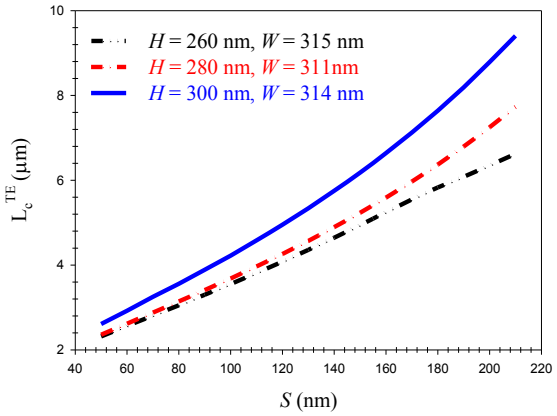

Fig. 5.18 Variations of the coupling length for the quasi-TE (H^{y}_{11}) supermodes with the waveguide separation, for the different widths.

It can be observed that as the separation between the waveguides is increased from 40 nm to 220 nm, the device length increases. For a smaller *S*, the L_c^{TE} of both the H = 260 nm and H = 280 nm can be noticed very close together. The height of the 300 nm, with W = 314 nm was observed to be higher than the other heights (H = 260 nm, and H = 280 nm).

Variations of the quasi-TE (H^{y}_{11}) and quasi-TM (H^{x}_{11}) supermodes of the coupling lengths as a function of the waveguide separation for a couple of identical Si nano-wire waveguides, when, H = 280 nm, and W = 311 nm, are shown in Fig. 5.19, by solid blue and red dash-dotted lines, respectively. The quasi-TE device length and quasi-TM coupling length are shown in this figure, are used vertical axis in right and left hands, respectively, with using the different scales. It can be seen that, for the both coupling lengths increases exponentially with the waveguides separation, *S*, but asymptotically reach their maximum value with the further increases of the separation.

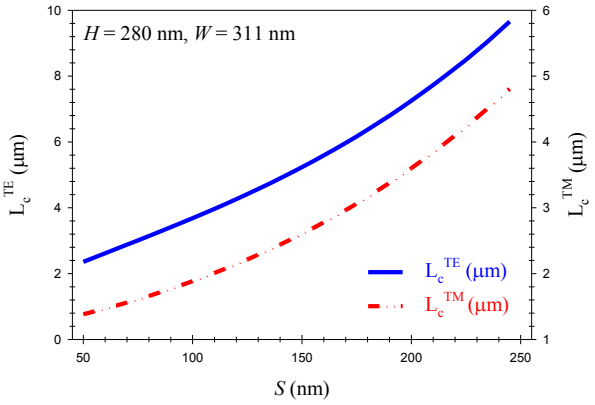

Fig. 5.19 Variations of the quasi-TM (H^{x}_{11}) and quasi-TE (H^{y}_{11}) coupling lengths with the waveguide separation, *S*.

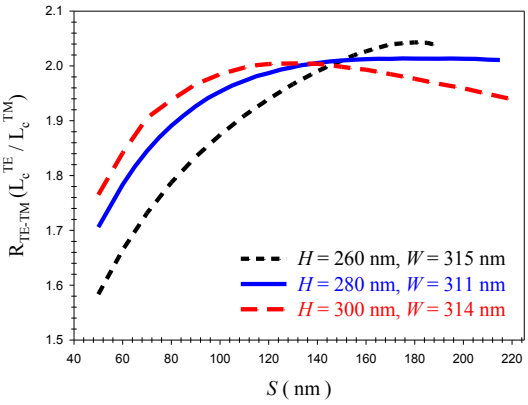

Fig. 5.20 Variations of the coupling length Ratio, R_{TE-TM}, with the waveguide separation, *S*.

At higher separations the guides are isolated and with the waveguides being nonidentical the birefringence does not change with increasing separation. Thus the coupling length remains constant. From Fig. 5.19, a relationship can be derived such that two times the coupling length for the quasi-TM (H^x_{11}) polarization mode equals the coupling length of the quasi-TE (H^y_{11}) polarization mode. In this case, when the separation between the waveguides was 150 nm, the L_c^{TM} was 2.604 μm and that for the quasi-TE polarized mode the device length, L_c^{TE} was 5.235 μm. Therefore by choosing a device section an effective TE/TM polarizer can be designed.

Variations of the coupling lengths ratio, $R_{TE\text{-}TM}$, with the waveguide separation for the quasi-TE and quasi-TM polarizations are shown in Fig. 5.20. The black short dashed, blue solid and long dashed red lines represent the H = 260 nm, 280 nm and 300 nm, with corresponding waveguide widths are 315 nm, 311 nm, and 314 nm, respectively. It can be observed from this figure that, as the separation between the waveguides is increased from 50 nm to 150 nm, the coupling lengths ratio, $R_{TE\text{-}TM}$ increases. At higher separations, as the guides are nearly isolated, the modal birefringence does not change any more with the waveguide separation. From Fig. 5.20, again a design relationship can be achieved such that $R_{TE\text{-}TM}$ = 2.00. It can be noticed from this figure that for the waveguide heights, H = 260 nm, 280 nm and 300 nm, the separation between the guides, S, should be 150 nm to get the ideal value, $R_{TE\text{-}TM}$ = 2.00. In these cases, the polarization splitter length should be equal to 4.940 μm, 5.235 μm and 6.180 μm, respectively.

5.6 Calculation effect of fabrication tolerance on the power transfer:

Although the short device length can yield a compact polarizer, but it is also necessary to study their fabrication tolerances in order to understand their suitability for practical applications. However, like all other photonic devices, its performance will also depend on the accuracy of fabrication. A small change of the width (or its height or their separation) would not only change their TE and TM polarization coupling lengths but also change the L_c ratio ($R_{TE\text{-}TM}$) from its desired value of 2.00.

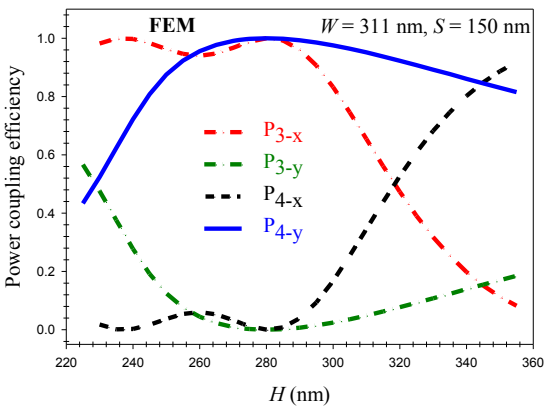

Fig. 5.21 Variations of the power coupling efficiency with the waveguides height, for W = 311 nm, and S = 150 nm.

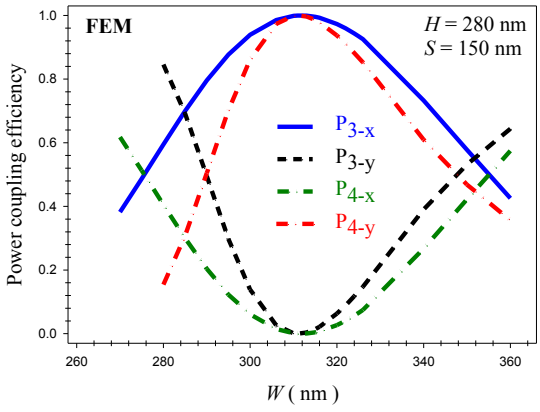

Fig. 5.22 Variation of the power coupling efficiency with the width changes for the H = 280 nm, and S = 150 nm.

In Figure 5.21 the performances of such polarization splitter (PS) have evaluated against the fabrication tolerances related to its height. A possible design was identified, when W = 311 nm, and S = 150 nm, resulting, L_c^{TE} = 5.235 μm and L_c^{TM} = 2.605 μm, giving $R_{TE\text{-}TM}$ =2.00. So, following an accurate fabrication if the device length is equal to 5.235 μm, then, it is expected that quasi-TE (H^y_{11}) mode will emerge from the Cross-port (Port 4) and quasi-TM (H^x_{11}) mode in the Bar-port (Port 3), as a solid blue and red dashed-dotted lines, and zero power remained as a cross-talk (C.T) in short dashed black, and dashed-dotted dark green lines, respectively.

It can be also noticed from the figure that when the waveguide heights is varied from the 270 nm to 360 nm, most of the power coupling efficiency and cross-talk for the quasi-TE (H^y_{11}) polarized mode are collected in Port 4, and Port 3, respectively, due to linear variation of the quasi TE-coupling length with the waveguide height (refer to Fig. 5.18).

On the other hand as a comparison, it is observed that variations of the power coupling efficiency for the quasi-TM (H^x_{11}) mode are very sensitive with the waveguide height. It is shown that, a small change in device height can be deteriorated from the characteristics of the quasi-TM polarized power transfer in Bar- and cross-ports. This circumstance again can be explained from the Fig. 5.18, as a non-monotonic variation of the coupling length L_c^{TM} with the waveguide height, which is explained in details before.

Now, it has tested its performance with the fabrication tolerances in the separation, W. Variation of the TE power output in the Cross-port ($P_{4\text{-}y}$) and TM output in the Bar-port ($P_{3\text{-}x}$) with the waveguide width are shown in Fig.5.22 by using a simple semi-analytical approach by using their changes in the coupling lengths only.

The red dashed-dotted line shows the TE power transfer characteristic in Port 4 ($P_{4\text{-}y}$) and the blue solid line shows the TM power transfer characteristics in Port 3 ($P_{3\text{-}x}$). The dark green dashed-dotted shows the TM power transfer characteristics in Port 4 ($P_{4\text{-}x}$) and the dark dashed line shows the TE power transfer characteristics in Port 3 ($P_{3\text{-}y}$). As can be seen from this figure, when H = 280 nm, and S = 150 nm, as desired, at the end of the device length, $L = L_c^{TE}$ = 5.236 μm, for both the TE and TM polarization, most of the polarized powers emerge from Ports 4 and 3, respectively.

Similarly at the end of the device length, L, for both TE and TM polarizations, almost zero power remained in Ports 3 and 4, respectively. Therefore, by selecting the device parameters suggested, a passive TE/TM polarizer can be designed.

It can be noticed from the Fig. 5.22 that small change in waveguide width can deteriorate the power transfer characteristics as this would destroy the ideal $R_{TE\text{-}TM}$ = 2.00 relationship and hence will contribute to deterioration of the power transfer characteristics. This also shows, as the non-monotonic nature of the quasi-TM coupling length, L_c^{TM}, power output for the quasi-TM mode is more sensitive compare to the quasi-TE polarization power mode.

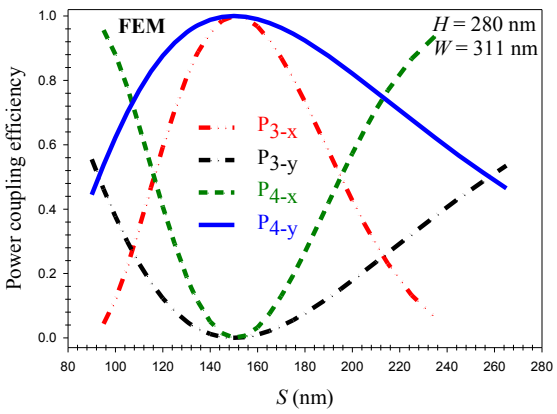

Fig. 5.23 Variations of the power coupling efficiency with the separation.

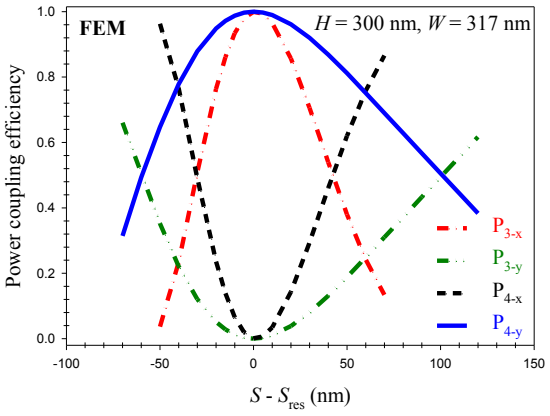

Fig. 5.24 Variations of the power coupling efficiency with the separation.

Figure 5.23 shows the variations of the power transfer as a function of the separation between the waveguides, when H = 280 nm and W = 311 nm, and the device length is kept fixed at L = 5.235 µm, as designed. As can be observed from this figure, when, S = 150 nm, as planned, at device length is equal to $L = L_c^{TE} \approx 2 * L_c^{TM} = 5.235$ µm, for both quasi-TM polarization for quasi-TE polarization, most of the power will emerge from the Bar-port ($P_{3\text{-}x}$) and in the Cross-port ($P_{4\text{-}y}$), shown by red dashed-dotted and blue solid lines, respectively.

Also, the black dashed-dotted and the green dashed lines show the quasi-TE power transfer characteristics in Port 3 ($P_{3\text{-}y}$) and the quasi-TM power transfer characteristics in port 4 ($P_{4\text{-}x}$), respectively. As can be seen from the figure, at the end of the coupling length, for both the quasi-TM (H^x_{11}) and quasi-TE (H^y_{11}) polarized modes, almost zero power remained in Bar-port ($P_{4\text{-}x}$) and Cross-port ($P_{3\text{-}y}$).

Therefore, by careful selection of the device parameters, a desired design for the polarization splitter is obtained. It can be noticed from these curves that a small change in waveguide separation can deteriorate the device performances.

This phenomenon can be explained with the help of Fig. 5.19. It can be noticed that as the waveguides separation is deviated from the design value of the $R_{TE\text{-}TM}$ value of 2.00, not only the ratio will increases, but also the resulting coupling length would not match with the device length and hence deteriorate of the power transfer characteristics. This also shows power output for the quasi-TM mode is more sensitive compare to the quasi-TE polarization power mode, as here n being twice of m, the phase error for quasi-TM mode mismatch would be double that of the quasi-TE mode. It should be noted that for such typical nanowires, as often height is smaller than its width, the effective index of the fundamental quasi-TM (H^x_{11}) mode is much lower than that of the fundamental quasi-TE (H^y_{11}) mode. This had contributed to a smaller coupling length for quasi-TM polarization, but this has also resulted in stronger coupling between the guides.

It is well known that for a strong coupled directional coupler cross-talk increases due to

incomplete cancellation of modal fields in the two waveguides, and similarly in this case power loss for the quasi-TM (H_x^{11}) polarization has been higher. Therefore, it is expected that by reducing the coupling for both quasi-TE and quasi-TM polarized modes, it may be possible to reduce the power loss for both the polarizations. However, coupling lengths for both the quasi-TE and quasi-TM modes will increase which will make the device length a bit longer. Besides that L_c ratio will also change, however, it is still possible to achieve the desired device length, L, by adjusting other waveguide parameters, such as, its width and height. It was identify a possible design, when H = 300 nm, when W = 317 nm and S = 150 nm, when L_c^{TE} = 17.90 µm and L_c^{TM} = 8.90 µm, giving $R_{TE\text{-}TM}$ = 2.00, in Fig.5.24. So if the device length is equal to 17.90 µm, then it is expected that quasi-TE mode will emerge from the Cross-port (Port 4) and quasi-TM mode in the Bar-port (Port 3). In this case, with ± 10 nm, tolerance from the maximum power coupling efficiency for the quasi-TE (H^y_{11}) and quasi-TM (H^x_{11}) modes at the optimum point in the separation, the power are found to be 0.9876, and 0.9465, respectively, which shows that the power coupling only decrease about 1.3 % and 5.5 % for polarized quasi-TE and quasi-TM modes, in a deviation of ± 10 nm from the desired optimum separation.

5.7 The FEM simulation used and results analysing obtained from LSBR:

The power output not only depends on the coupling length or the coupling length ratio, but also on the modal coefficients of the supermodes excited at the start of the directional coupler. To satisfy the continuity of the tangential electric and magnetic fields, E_t and H_t, an incident mode generates two supermodes and may also excite other guided or radiating modes. In this study a rigorous full-vectorial least squares boundary residual method [184] is used to find the modal coefficient of the two supermodes. A rigorous LSBR method is used to calculate the polarized power transfer in both the output ports. In this case, besides the excitation coefficients of the supermodes at the junctions, the effect of coupling length change, and the effects of coupling strength are also considered.

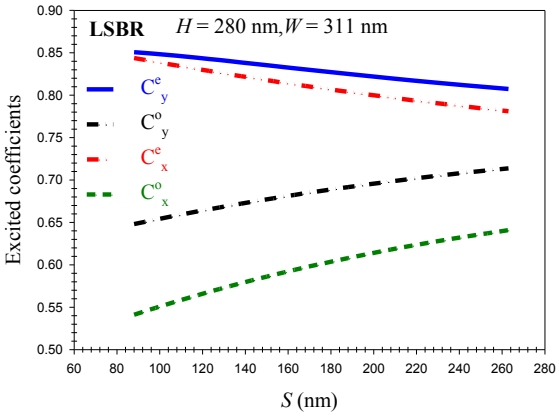

Fig. 5. 25 Variation of the excited quasi-TE (H^y_{11}) and (H^x_{11}) TM coefficients with the changes in the separation, S.

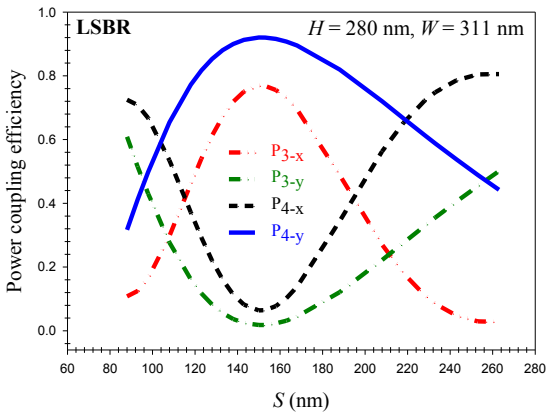

Fig. 5.26 Variation of the power coupling efficiency with the changes in the separation, S.

The variations of the transmitted coefficients from the LSBR results, for both quasi-TE (H^y_{11}) and quasi-TM (H^x_{11}), even and odd supermodes, in terms of the waveguide separation are shown in Fig. 5.25. Transmitted modes of the quasi-TE (H^y_{11}) and quasi-TM (H^x_{11}) in even supermodes are shown in solid blue and dash-dotted red lines, respectively. It is shown here that as the separation between the waveguides increases, the even transmitted coefficient reduces for both quasi-TE (H^y_{11}) and quasi-TM (H^x_{11}) modes, respectively. It can be noticed that, variations of the transmitted coefficients, C^e_y, and C^e_x with the separation are nearly close together, and almost stable.

Variation of the quasi-TE (H^y_{11}) and quasi-TM (H^x_{11}) odd modes, in terms of waveguide separation are shown in black dashed-dotted and dark green short-dashed lines. It can be observed that as the separation increases, the odd transmitted coefficients for both quasi-TE (H^y_{11}) and TM (H^x_{11}) modes. It is also shown that, the odd mode for both polarized modes are significantly lower than its even supermodes transmitted coefficient, and also very much separation between the waveguides dependence. The transmitted coefficients, C^e_y and C^o_y for the quasi-TE (H^y_{11}) even and odd supermodes are calculated as 0.83536 and 0.67721, respectively, and transmitted coefficients of the even and odd quasi-TM (H^x_{11}) supermodes, C^e_x and C^e_o are obtained 0.81770 and 0.58613, respectively, when S = 150 nm.

Figure. 5.26 shows the variation of the power transfer for different separations between the waveguides for H = 280 nm, and W = 311 nm. The solid blue line $P_{4\text{-}y}$ and the red dashed-dotted-dotted line $P_{3\text{-}x}$ show the power transfer characteristics for the quasi-TE (H^y_{11}) and polarized modes in the Cross-port (Port 4) and quasi-TM (H^x_{11}) mode in the Bar-port (Port 3), respectively. The dark short-dashed shows the quai-TM power transfer characteristic in Port 4 ($P_{4\text{-}x}$) and the dark green dashed-dotted line shows the TE power transfer characteristics in port 3 ($P_{3\text{-}y}$). In this case, it can be noticed that transfer of the quasi-TM power ($P_{3\text{-}x}$) in port 3 with the cross talk ($P_{4\text{-}x}$) in port 4 have deteriorated significantly compared to the transfer of quasi-TE power ($P_{4\text{-}y}$) in Port 4, and its cross-talk ($P_{3\text{-}y}$) state in the port 3. For the quasi-TE mode power transfer to Cross-Port ($P_{4\text{-}y}$) was 92 %, represent only 0.40 dB loss, when S = 150 nm, and 77 % power transferred to Bar-Port ($P_{3\text{-}x}$) with a loss value of 1.10 dB. It is shown here that for separation S = 150 nm, $P_{3\text{-}y}$ and $P_{4\text{-}x}$, to the Cross-Port and the Bar-Port, demonstrate those C.T are – 18 dB, and – 12 dB, respectively.

Weak coupling can also make the device sensitive with the fabrication tolerances. Therefore, it may be necessary to control the separation of these waveguides within a few nanometers, and sensitivity of this parameters, must be studied.

Figure 5.27 shows the variation of the waveguide width for both quasi-TE (H^y_{11}) and quasi-TM (H^x_{11}) modes with the separation between the waveguides. The W is clearly increased as the S is increased from 140 nm to 300 nm, giving a 317 nm at the optimum position at S = 300 nm. This is anticipated, since increased simultaneously, the separations and widths is equivalent to the increase in device length.

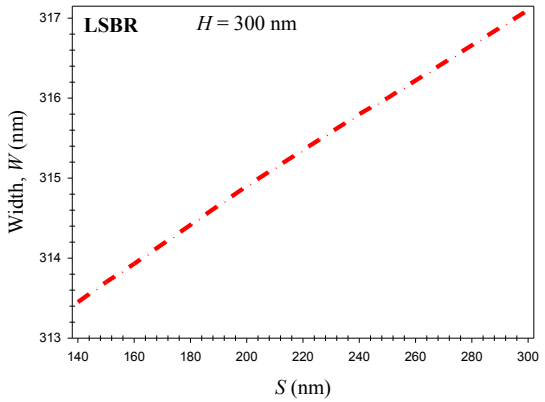

Fig. 5.27 Variation of the waveguides width of the supermodes with the changes in the separation, *S*.

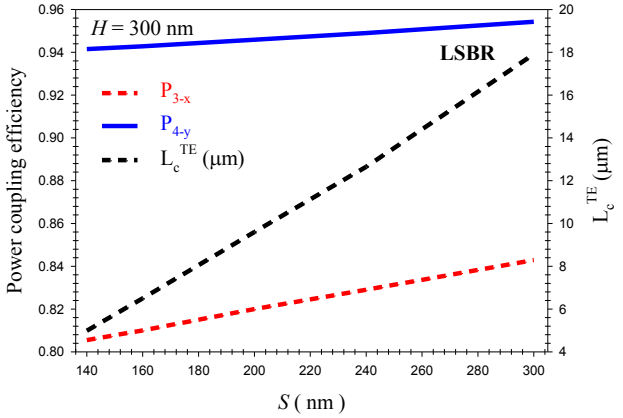

Fig.5.28 Variation of the power transfer for the quasi-TM and quasi-TE modes, and coupling length of the quasi-TE mode with the waveguide separation, *S*.

Figure 5.28 shows the variation of the power transfer for the quasi-TE and quasi-TM polarized modes as a function of the waveguide separation by using the LSBR method. In this case, its height was kept fixed at 300 nm, and width was adjusted to achieve $R_{TE\text{-}TM} = 2.00$ for a given separation. It can be noticed that, by increasing the separation between the waveguides width, transferred power of quasi-TE polarized mode to the Port-4 and quasi-TM polarized mode into the Port-3 are increased. It can be noticed from this figure that when the separation between the guides change from the 140 nm to the 300 nm, the power transfer increased from the 0.9415 to 0.9543 for the quasi-TE input in Port-4 and from 0.8055 to 0.8429 for the quasi-TM polarized modes in Port-3, respectively. At the same time, the cross-talk improved from -18.6 dB to -26 dB for the quasi-TE input and from -13 dB to the -20 dB for the quasi-TM polarized modes, respectively (but not shown here). The black dashed curve in Fig. 5.28 shows the coupling length for the quasi-TE mode (the right-hand Y –axis scale) as a function of the waveguide separation. It can be seen from this figure that, as the separation between the guides is increased from 140 to 300 nm, the coupling length ($L = L_c^{y}$) increases linearly from 5.0 μm to 17.9 μm.

Variation of the power transfer for the different separation between the waveguides for H = 300 nm, W = 317 nm and L = 17.9 μm are studied next, and shown in Fig. 5.29. The solid blue shows the quasi-TE power transfer characteristics in Port 4 ($P_{4\text{-}y}$) by using the LSBR result. The dashed red line shows that the quasi-TM power transfer characteristics in Port 3 ($P_{3\text{-}x}$). In this case most of the quasi-TE polarized power transferred to Cross-Port ($P_{4\text{-}y}$) with only 0.21 dB loss and quasi-TM power into Bar-Port ($P_{3\text{-}x}$) with 0.74 dB loss. It can be noticed that from this curve that the deterioration of the quasi-TM power transfer characteristics ($P_{3\text{-}x}$) is more severe than the quasi-TE case. It can be noted that quasi-TE output power in Cross-Port is better than 50 % of its maximum value, when separation is in the range of 240 nm to 400 nm. On the other hand quasi-TM output in the Bar-Port is better than 50 % of its maximum value, when separation is between 275 nm to 340 nm. This

narrower quasi-TM range is due to *n* being double of *m*. In Fig. 5.29, the green dashed-dotted line shows the cross-talk in the Bar-port ($P_{3\text{-}y}$) for the quasi-TE case and the dashed-dotted black line shows the cross-talk in the Cross-port ($P_{4\text{-}x}$), for the quasi-TM polarization mode, calculated by the LSBR method. It can be noticed that change in separation can deteriorate the cross-talk for the both cases, but this also shows cross-talk for quasi-TM mode is more sensitive compare to the quasi-TE mode. As can be seen from this figure, when $S = 300$ nm, at the end of the device length, for both the quasi-TE and quasi-TM modes, almost zero power remained in Port 3 and Port 4, respectively.

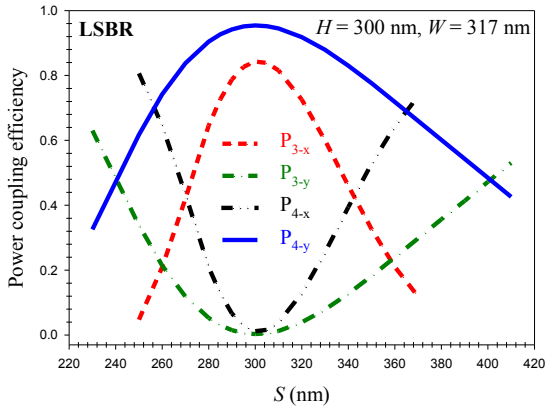

Fig.5. 29 Variation of the power transfer for the different separations between the waveguides, for $H = 300$ nm and $W = 317$ nm.

5.8 Fabrication tolerance analysis of the operating wavelength:

In this section, the effect of the operating wavelength on the polarization splitter behavior is considered and also a study of the fabrication tolerances on the wavelength has been carried out. The operating length, λ is varied from 1460 nm to 1600 nm. This structure has been optimized for the operating wavelength of λ = 1550 nm. Any changes in the operating wavelength will change the coupling length, coupling length ratio and also the supermode coefficients.

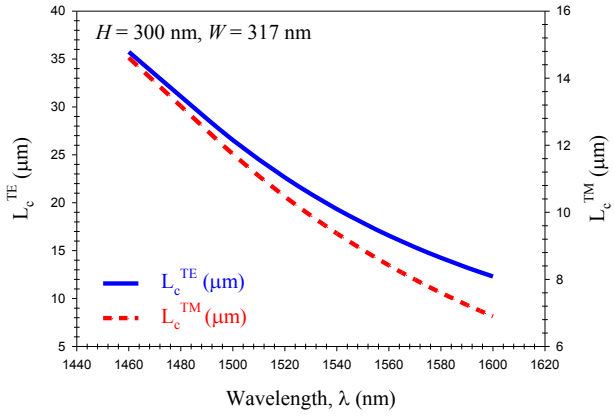

Fig. 5. 30 Variation of the coupling lengths for $H = 300$ nm, $W = 317$ nm, and $S = 150$ nm with the operating wavelength, λ.

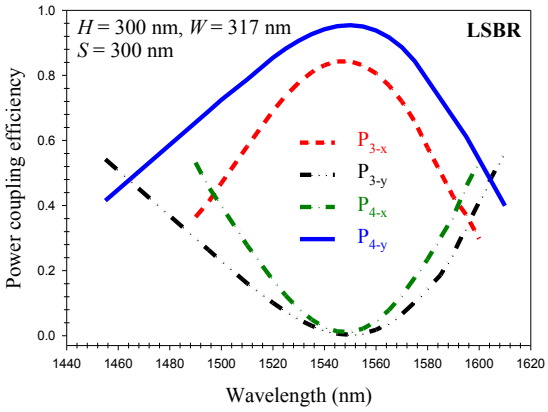

Fig. 5. 31 Variation of the power transfer with the wavelength for $H = 300$ nm, $S = 150$ nm and $W = 317$ nm.

Figure 5.30 shows the variation of the coupling lengths, L_c^{TE} and L_c^{TM} with the operating the wavelength, λ. It is clearly seen that the device lengths are maximum at λ = 1460 nm and reduced as the wavelength, λ is increased. Device length, L_c^{TE} variation is about + 100 % and – 30 % with respect to the corresponding device length value for the optimum operating wavelength of λ = 1550 nm.

We have identified a possible design in Figure 5.31, when H = 300 nm, when W = 317 nm and, S = 300 nm, when L_c^{TE} = 17.90 μm, and L_c^{TM} = 8.877 μm. So if the device length is equal to 17.90 μm, then it is expected that TE mode will emerge from the Cross-port (Port 4) and TM mode in the Bar-port (Port 3).

The structure has been optimized for the operating wavelength of λ = 1550 nm. Any changes in the operating wavelength will change the coupling length, coupling length ratio, R_{TE-TM}, and also the supermode coefficients.

However, like all other photonic devices, its performance will also depend on the accuracy of fabrication. As can be seen from this figure, when S = 300 nm, as desired, at the end of the device length, $L = L_c^{TE}$ = 17.90 μm, for both the quasi-TE and quasi-TM for both the TE and TM polarization, most of the polarized powers emerge from Ports 4 and 3, respectively. It can be noticed that, transfer power are 0.96 and 0.85 for the quasi-TE (H^y_{11}) and the quasi-TM (H^x_{11}) polarized modes, respectively.

Similarly at the end of the device length, L, for both TE and TM polarizations, almost zero power remained in Ports 3 and 4, respectively. This shows power output for TM mode is more sensitive. However, in this design, as the effect of small change in the wavelength on the power coupling is almost negligible.

This indicates that for many practical applications the device will have a larger operating bandwidth. The effect of temperature variation has also been studied for this device but this is not presented here.

It was identified that a small amount of temperature tuning may be possible, which can be used to compensate fabrication tolerances, but the tuning range is rather very limited. Similarly, as Fig.5.21 indicates a small amount of wavelength tuning can also be used to compensate the fabrication tolerances.

5.9 Summary:

The design presented in this work uses two identical silicon nanowires, which would be simpler than the design approaches reported earlier by using slot waveguides [213-216]. As the proposed structure does not consider any bent section or slanted side wall [211], and [226], or trench with different etch depth [190, 198, 192] so, it would be easier to fabricate.

No metal clad has been used which avoids plasmonic modal loss. Two identical waveguides are used which shows better fabrication tolerances. This design approach is optimized by using rigorous numerical approaches. The above results suggest that an appreciable short 17.90 μm long PS can be designed at the 1.55 μm wavelength by adjusting

the coupling lengths ratio of the quasi-TE and quasi-TM polarized modes. Device parameters are optimized in such a way that the PS length is equal to odd and even multiples of the coupling length for two different polarizations.

Important fabrication parameters such as the height, width, separation, birefringence and wavelength sensitivity have been rigorously verified and their operating characteristics are shown. Maximum power transfer of 96 % for the quasi-TE polarized and 85 % for the quasi-TM polarized modes from input TE/TM mode, with crosstalk better than – 26 dB and loss value lower than 0.2 dB.

It is shown here that, it is necessary for all the numerical methods; the stability of the numerical parameters should be established before the design process. Thus this high conversion efficiency, low footprint, simpler design, along with the use of well-matured fabrication technologies for SOI structures, should make the proposed design attractive for making an on-chip polarization splitter for their potential deployment. This design should be relatively easy to implement for fabrication and can be made with a single mask. It is also shown here that operating bandwidth of these PS is considerable wider and suitable for WDM application.

6.0 Conclusions:

The aim of this PhD research concentrated on the design characterisation, and optimization of the polarization diversity based silicon photonic devices. The outline arranged in the starting of the specific field of the research and the study has been successfully completed and its performance analysis of the results through the academic course is presented.

Accurate and rigorous numerical method, with high accuracy for analysing of optical waveguides utilized in optimal silicon photonic devices has been considered in this research. This fundamental strategy was used to study of modal solution in the dimensional range of submicron scale for such diversity polarization dependence devices. Following the literature review, correspondence to the study of system polarization diversity in nano-photonic devices, the basic and important of the numerical methods, which employed in this research was presented in chapter two.

The most important and versatile method, Finite Element Method according to the H-vector field modal solution (VFEM) and the Least Squares Boundary Method (LSBR) are explained in detail. For finding the modal field profile in terms of hybridness and also to obtain the propagation constants for the fundamental and higher order of the quasi-TE and quasi-TM modes as a most accurate and effective numerically approach has been introduced in along the research.

Important section of the second chapter was dedicated to the fundamental mathematical feature for the finite element technique, which employed for the optical waveguide devices. Many practical waveguide photonic devices utilized from the magnetic H-field vector formulation, due to field being naturally continuous across the dielectric interfaces and the natural boundary condition being equivalent to that of an electric wall. In this formulation, basic impression such as domain discretization, element matrices and also the shape functions as a approximate representation of the real fields in order to expand the number of elements to reduce the resulting error. The H-field vectorial formulation may generate spurious solutions, along with real and physical solutions, which cannot be ignored, and to resolve that modified for this non-physical solution, penalty function method by imposing the constraint ($div.H = 0$) was employed in to that. In most of the polarization diversity system, finding the characteristics of the modal field profile, and also propagation constant of the supermodes in the waveguides are seems to be very necessary. The Finite element technique is the one of the most powerful and accurate method which can be applied to obtain the modal birefringence solution in such nano-photonic devices.

On the other hand, it would be considered to calculate the initial modal field profile, and supermodes field distribution data at the discontinuities in the waveguide junctions for the analysis by using the Least Squares Boundary Residual (LSBR) method. It is presented in Chapter 2, by using the transmission and reflection coefficients of all the polarized modes, without ignoring the guided and radiation modes, to calculate the power transfer efficiency

between two waveguides and also the insertion power loss of discontinuities in butt-junction nano-diversity devices.

Monolithic integration an appropriate of optical and electronic potential on unique substrate is the prospective of an integrated nano-photonic system. Employing silicon would be able to develop a platform for a such monolithic integration, for interconnecting of optics and microelectronic devices. Therefore, in order to design of optical system, the cross-section of the waveguide devices must be considered in the submicron dimensions. The small dimensions of the silicon waveguides enable ultra-compact devices to be integrated on-chip. Their high-confinement nature offers the potential of the light enhancing in the small region.

Chapter 3 reported a Si nano-wire waveguide based on the silicon-on-insulator (SOI) platform. Silicon nano-wire waveguide is the fundamental device and very most prominent in several Photonic Integrated Circuit (PIC) fabrication technology. In this chapter, the Si nano-scale waveguide were presented with critical dimension and effect of its specific characterization from the modal solution. The spatial variations of the H-field vectorial formulation were shown for any practical devices. The range of waveguide width for a single and second higher modes of the different heights for a Si core with the air clad has been shown in wavelength of 1550 nm and, also, the important results come out from the modal solution, such as modal hybridness, power confinement, modal birefringence were discussed in detail. It was found from the simulation data generated for the standard and practical nano-wire waveguide, that H = 220 nm, amplitude of the dominant field profile and effective area are 6.13 and 0.186 μm^2, respectively, when waveguide width is 350 nm, and also, the single mode operation occurs when widths around between 280 nm to 360 nm.

A novel compact polarization rotator using with two simple silicon nanowires was shown which unequal waveguide widths. The Si polarization rotator proposed here, illustrates an ultra-compact design without slanted side wall or bent. Optimize design of a Si polarization rotator based on SOI technology was presented which requires less complex fabrication process with single mask only and is compatible with mature CMOS technology, which is backed by a well-established semiconductor industry. Accurate calculation of the magnitudes of the non-dominant field components and their profiles for the fundamental quasi-TE and quasi-TM polarized modes are of great importance when designing a PR. It has been shown that, this modal hybridness becomes more prominent as the index contrast increases, as in silicon nano-wires devices.

In the design process, it is necessary not only to increase the magnitude of the non-dominant field components but also its profile, which also can be optimized to enhance its overlap with the dominant field components to achieve maximum polarization rotation. A full-vectorial finite element method is needed and used here to obtain the modal field profiles of the constituent WGs. A junction analysis approach also can be used, as the proposed PR structure is composed of only two butt-coupled uniform WG sections with only two discrete interfaces between them. Therefore, powerful numerical approach, the least-squares boundary residual (LSBR) method also can be used, which rigorously satisfies the continuity of the tangential electric and magnetic fields at the junction interface in a least-squares sense and

obtains the modal coefficients of the transmitted and reflected fully hybrid modes at the discontinuity interface. It has been shown that, it was important to design a polarization rotator waveguide that can rotate an incoming TE input wave to the converted to TM polarized wave mode. It was found that more than 99% of polarized power conversion obtained with a compact device length of 52.8 μm long. The mentioned polarization rotator can be achieved with a low-loss, wide bandwidth and polarization cross-talk – 20 dB.

In chapter 5, polarization splitter based on silicon-on-insulator (SOI) platform has been presented incorporates with two simply coupled silicon nanowires. This design can be easily fabricated by using standard Complementary Metal-Oxide-semiconductor (CMOS) technology and fully compatible with standard active silicon photonics platform. Polarization splitters generally are increasingly being considered for the realization of integrated-optical circuits for optical sensors and communication applications, where polarization plays an essential role.

In polarization splitter, the input wave to the device, separated to the couple orthogonal TE/TM polarized waveguides, and emerges from the two different ports. Device performance has been achieved by considering these two ports, called Cross-port, and Bar-port. Here, the modal characteristics presented are strongly polarization independent due to the high birefringence in the optical waveguides. The numerical simulation carried out for the device using the versatile and accurate vectorial finite element technique; indicate to the dependence of the quasi-TE, and quasi-TM polarization modes. This two polarized in terms on even and odd modes would be exploited to find the polarization splitting ratio to the design of a compact polarization splitter.

Accuracy of the design parameters obtained will critically depend on the using a given numerical methods. The accuracy of these design parameters are depend on the number of elements used in the FEM method. In this chapter calculation of the critical numerical parameters with the mesh divisions used are studied accurately. A powerful, full-vectroial numerical approach, the Least Squares Boundary Residual (LSBR) can be used to analyse discontinuity along a waveguide devices, which consists of two discrete interfaces. By employing the FEM propagation constant for the even and odd for the quasi-TE and quasi-TM fundamental modes are calculated and employed as the input data to the LSBR method. This method would be more efficient to use to find the exited modal coefficients followed by calculate the power conversion between the two polarization states at the butt-coupled junctions in the device.

The polarization splitter proposed based on silicon-on-insulator (SOI) is very compact design without a metal clad section or bent and less complex fabrication, and compatible with the mature CMOS technology, by using two simple coupled identical nanowires. This design approach is optimized by using rigorous numerical approaches. The above results suggest that an appreciable short 17.90 μm long PS can be designed at the 1.55 μm wavelength by adjusting the coupling lengths ratio of the quasi-TE and quasi-TM polarized modes. Device parameters are optimized in such a way that the PS length is equal to odd and even multiples of the coupling length for two different polarizations.

Important fabrication parameters such as the height, width, separation, birefringence and wavelength sensitivity have been rigorously verified and their operating characteristics are shown. Maximum power transfer of 96 % for the quasi-TE polarized and 85 % for the quasi-TM polarized modes from input TE/TM mode, with crosstalk better than – 26 dB and loss value lower than 0.2 dB.

6.1 Suggestion for future work:

A 2-dimensional Bragg grating can be considered to couple both TE and TM modes. The beam profile generated by Bragg grating coupler is not exactly a Guassian mode therefore it is necessary to improve the beam shape. Apodized grating can be considered to improve the beam profile for better coupling but this requires multiple masking steps in the fabrication process.

Design of a PIC with a polarization diversity system that consists of polarization rotator and polarization splitter can be considered.

The polarization rotator can be presented with Si asymmetric structure, and also use the directional coupler based on Si nanaowires, with using the mask between them.

Design of the polarization rotator, and also polarization splitter with two simple nanowires waveguide, employing the SiO_2 cladding.

Design of polarization rotator with propose the phase-matching condition to the fundamental mode of the quasi-TE (H^y_{11}) with the second mode of the quasi-TM (H^x_{12}) mode, for the different design consist of symmetric and asymmetric cross-section Si NWs, with surrounded with several material such as SiO_2.

Design and study of an active polarization controller can be carried out in silicon nanowirer structure by using twin electrodes with both biasing and controlling signals. The asymmetry is introduced by incorporating a non-symmetric modulating electric field in order to control polarization conversion. In this case both the phase matching and polarization conversion can be achieved simultaneously.

Cascaded polarization rotator and splitter designs using slanted silicon nanowire waveguides.

Functional device operates with only TE or TM polarized optical signals. In a polarization diversity photonic circuit as Figure shown in 1.1, a single polarization is obtained and two sections may work together in parallel with unique structure. This could be a polarization sensitive microring resonator employed for optical signal processing such as modulating, filtering, switching or multiplexing.

Calculation of Element Matrices:

The elements matrices of $[A]_e$ and $[B]_e$ from equations 2.51 and 2.52 are evaluated here:

Equation 2.51 shown that:

$$[\mathbf{A}]=\sum_{e=1}^{n}[\mathbf{A}]_e=\sum_{e=1}^{n}\int_{\Omega}\varepsilon^{-1}[Q]^{*}[Q]\partial\Omega$$

Therefore

$$[\mathbf{A}]_e=\varepsilon^{-1}\int_{\Omega}[Q]^{*}[Q]\partial\Omega$$

$$=\int_{\Omega}\varepsilon^{-1}\begin{bmatrix} -\beta^{2}[N]^{T}[N]+\frac{\partial[N]^{T}}{\partial y}\frac{\partial[N]}{\partial y} & -\frac{\partial[N]^{T}}{\partial y}\frac{\partial[N]}{\partial x} & j\beta[N]^{T}\frac{\partial[N]}{\partial x} \\ \frac{\partial[N]^{T}}{\partial x}\frac{\partial[N]}{\partial y} & -\beta^{2}[N]^{T}[N]+\frac{\partial[N]^{T}}{\partial x}\frac{\partial[N]}{\partial x} & j\beta[N]^{T}\frac{\partial[N]}{\partial y} \\ j\beta\frac{\partial[N]^{T}}{\partial x}[N] & j\beta\frac{\partial[N]^{T}}{\partial y}[N] & \frac{\partial[N]^{T}}{\partial y}\frac{\partial[N]}{\partial y}+\frac{\partial[N]^{T}}{\partial x}\frac{\partial[N]}{\partial x} \end{bmatrix}\partial\Omega \qquad \text{(A1.1)}$$

Equation 2.52 shown that

$$[\mathbf{B}]=\sum_{e=1}^{n}[\mathbf{B}]_e=\sum_{e=1}^{n}\int_{\Omega}\mu[N]^{T}[N]\partial\Omega$$

Therefore

$$[\mathbf{B}]_e=\mu\int_{\Omega}[N]^{T}[N]\partial\Omega$$

$$=\mu\int_{\Omega}\begin{bmatrix} [N]^{T}[N] & [0]^{T}[0] & [0]^{T}[0] \\ [0]^{T}[0] & [N]^{T}[N] & [0]^{T}[0] \\ [0]^{T}[0] & [0]^{T}[0] & [N]^{T}[N] \end{bmatrix}\partial\Omega \qquad \text{(A1.2)}$$

The integration of the shape functions in equations A1.1 and A1.2 can be evaluated for a triangular element using the following relation:

$$\int_{\Omega} N_1^i N_2^j N_3^k \partial\Omega = \frac{i!\,j!k!2!}{(i+j+k+2)!} A_e \tag{A1.3}$$

where A_e is the area of the triangular element.

Hence the following integrals can be obtained:

$$\int_{\Omega} N_1^2 \partial\Omega = \int_{\Omega} N_2^2 \partial\Omega = \int_{\Omega} N_3^2 \partial\Omega = \frac{A_e}{6} \tag{A1.4}$$

$$\int_{\Omega} N_1 N_2 \partial\Omega = \int_{\Omega} N_2 N_3 \partial\Omega = \int_{\Omega} N_1 N_3 \partial\Omega = \frac{A_e}{12} \tag{A1.5}$$

$$\int_{\Omega} \partial\Omega = A_e \tag{A1.6}$$

Therefore from equation A1.1, some of the 9 x 9 $[A]_e$ elements matrix can be given as:

$$[\mathbf{A}]_{e(1,1)} = \frac{1}{\varepsilon}\int_{\Omega} -j\beta N_1^2 + \left(\frac{\partial N_1}{\partial y}\right)^2 \partial\Omega = \frac{1}{\varepsilon}\left[\frac{-\beta^2 A_e}{6} + c_1^2 A_e\right] \tag{A1.7}$$

$$[\mathbf{A}]_{e(1,2)} = \frac{1}{\varepsilon}\int_{\Omega} -j\beta N_1 N_2 + \frac{\partial N_1}{\partial y}\frac{\partial N_2}{\partial y}\partial\Omega = \frac{1}{\varepsilon}\left[\frac{-\beta^2 A_e}{12} + c_1 c_2 A_e\right] \tag{A1.8}$$

$$[\mathbf{A}]_{e(1,4)} = \frac{1}{\varepsilon}\int_{\Omega} \frac{-\partial N_1}{\partial y}\frac{\partial N_1}{\partial x}\partial\Omega = \frac{1}{\varepsilon} c_1 b_1 A_e \tag{A1.9}$$

From equation A1.2, some of the 9 x 9 $[B]_e$ elements matrix can also be given as:

$$[\mathbf{B}]_{e(1,1)} = \mu\int_{\Omega} N_1^2 \partial\Omega = \mu\frac{A_e}{6} \tag{A1.10}$$

$$[\mathbf{B}]_{e(1,2)} = \mu\int_{\Omega} N_1 N_2 \partial\Omega = \mu\frac{A_e}{12} \tag{A1.11}$$

$$[\mathbf{B}]_{e(1,4)} = 0 \tag{A1.12}$$

List of publications by the author:

1. S. Soudi, and B. M. A. Rahman, "Design of compact polarization rotator using simple silicon nanowire," *Appl. Opt*., vol. 53, no. 34, pp. 8071-8077, Dec. 2014.
2. S. Soudi, and B. M. A. Rahman, "Design of compact polarization splitter using simple silicon nanowires*," International Workshop on Optical Wave & Waveguide Theory and Numerical Theory,* pp. 120, Apr. 2015.
3. S. Soudi, and B. M. A. Rahman, "Design of compact polarization splitter using simple silicon nanowires," *Photonic Networks and Devices, Boston, Massachusetts United States,"* Jun. /Jul. 2015.
4. S. Soudi, and B. M. A. Rahman, "Design of a compact polarization splitter by using identical coupled silicon nanowires," Submitted to the Journal of Lightwave Technology (*IEEE JLT*).

References:

1. M. Arumugam, Optical Fibre Communication – An Overview, *J. of Phys*., vol. 57, no. 5 & 6, PP. 849–869, Dec. 2001.
2. K. C. Kao, and G. A. Hockham, "Dielectric-fiber surface waveguides for optical frequencies," *PROC. IEE*, vol. 113, no. 7, Jul. 1966.
3. D. F. Welch, F. Kish, S. Melle, R. Nagarajan, M. Kato, CH, Joyner, JL. Pleumeekers, RP. Schneider, Jr., Back, AG. Dentai, VG. Dominic, PW. Evans, M Kauffman, DJ. H. Lambert, SK. Hurtt, A Mathur, ML. Mitchell, M Missey, S Murthy, AC. Nilsson, RA. Salvatore, MF. Van Leeuwen, J Webjorn, M Ziari, SG. Grubb, D Perkins, M Reffle, and D. G. Mehuys, "Large-scale InP photonic integrated circuits: enabling efficient scaling of optical transport networks," *IEEE J Select Top Quantum Electron*; vol. 13, no. 1, pp. 22–31, Jan. /Feb. 2007.
4. S.C. Nicholes, M.L. Maˇsanovic, B. Jevremovic, E. Lively, L.A. Coldren, and D.J. Blumentha, "An 8*8 InP monolithic tunable optical router (motor) packet forwarding chip. *J. Lightw. Technol*., vol. 28, no. 4: pp. 641–50, Feb.2010.
5. D. Liang, and J. E Bowers, "Photonic integration: Si or InP substrates," *Electron Lett.,* vol. 45, no. 12, pp. 578-581, Jun. 2009.
6. LA. Coldren, SC. Nicholes, L. Johansson, S. Ristic, RS. Guzzon, J. N Erkin, and K. Uppiliappan, "High performance InP-based photonic ICs—a tutorial. *J. Lightw. Technol.,* vol. 29, no. 4, pp. 554–570, Feb. 2011.
7. T. Barwicz, M. R. Watts, M. A. Popović, P. T. Rakich, L. Socci, F. X. Kärtner, E. P. Ippen, and H. I. Smith, "Polarization-transparent microphotonic devices in the strong confinement limit," *Nat. Photonics***1** , pp. 57–60 , Dec. 2007.
8. K. Sasaki, Ohno F, Motegi A, and T. Baba, "Arrayed waveguide grating of 70×50 μm^2 size based on Si photonic wire waveguides," *Electron Lett*; vol. 41, no. 14, pp. 801-802, Jul. 2005.
9. D. Dai, L. Liu, L. Wosinski, and, S .He, "Design and fabrication of ultra-small overlapped AWG demultiplexer based on alpha-Si nanowire waveguides,"*Electron Lett*., vol. 42, no.7, pp. 400–402, Mar. 2006.
10. W. Bogaerts, S. K. Selvaraja, P. Dumon, J. Brouckaert, K. D. Vos, D. V. Thourhout, and R. Baets, "Silicon-on-insulator spectral filters fabricated with CMOS technology," *IEEE J Sel Top Quant Electron*, vol. 16, no. 1, pp. 33–44, Jan. / Feb. 2010.
11. H. Fukuda, K. Yamada, T. Tsuchizawa, T. Watanabe, H. Shinojima, and, S. Itabashi, "Silicon photonic circuit with polarization diversity," *Opt Express,* vol. 16, no. 7, pp. 4872–80, Mar. 2008.
12. Z. Sheng, D. Dai, and S. He, "Comparative study of losses in ultrasharp silicon-on-insulator nanowire bends," *IEEE J Sel Top Quant Electron*, vol. 15, no. 5, pp. 1406-1412, Sep./Oct. 2009.
13. D. Liang, and J. E. Bowers, "Recent progress in laser on silicon," *Nat. Photonics* **4**, pp. 511-517, Aug. 2010.
14. G. Kurczveil, MJ. R. Heck, J. M. Garcia, HN. Poulsen, H. Park, D. J. Blumenthal, and JE. Bowers, "Integrated Recirculating optical hybrid silicon buffers," *SPIE Photonics West*; vol. 7943, 24 Jan. 2011

15. D. Dai, Y. Shi, and, S. He, "Theoretical Investigation for reducing polarization-sensitivity in Sinanowire-based arrayed-waveguide grating (de)multiplexer with polarization-beam splitters and reflectors," *IEEE J Quant. Electron*, vol. 45, no. 6, pp. 654-660, Jun. 2009.
16. T. Pfau , R.Peveling , J. Hauden, N. Grossard, H. Porte, Y. Achiam, S. Hoffmann, S. K. Ibrahim, O. Adamczyk, S. Bhandare, D. Sandel, M. Porrmann, and R. Noe, "Coherent digital polarization diversity receiver for real-time polarization-multiplexed QPSK transmission at 2.8 Gb/s," *IEEE Photon Technol. Lett*; vol. 19, no. 24, pp. 1988–19990, Dec. 2007.
17. A. Sakai, G. Hara, and T. Baba, "Propagation characteristics of ultrahigh- optical waveguide on silicon-on-insulator substrate," *Jpn. J. Appl. Phys*., vol. 40, no. 4B, pp. L383–L385, Apr. 2001.
18. K. K. Lee, D. R. Lim, H.-C. Luan, A. Agarwal, J. Foresi, and L. C. Kimerling, "Effect of size and roughness on light transmission in Si/SiO_2 waveguide experiments and model," *Appl. Phys. Lett*., vol. 17, no. 11, pp. 1617-1619, Sep. 2000.
19. L. C. Kimerling, "Silicon microphotonics," *Appl. Surf. Sci*., vols. 159–160, pp. 8–13, Jun. 2000.
20. M. Khorasaninejad and S. S. Saini, "Bend-waveguides on silicon nanowire optical waveguide (SNOW)," *IEEE Photon. J.*, vol. 3, no.4, pp. 696–702, Aug. 2011.
21. D. Dai and J. E. Bowers, "Novel concept for ultracompact polarization splitter-rotator based on silicon nanowires," *Opt. Express*, vol.19, no. 11, pp.10940-10949, May 2011.
22. K. Shiraishi, T. Daidoji, and H. Yoda, "Vertical-tunneling spot-size converters for silicon-wire waveguides," Group IV Photonics (GFP), *IEEE 9th International Conference*, pp. 252-254, Aug. 2012.
23. Y. A. Vlasov and S. J. McNab, "Losses in single-mode silicon-on-insulator strip waveguides and bends," *Opt. Express*, 12, no. 8 pp. 1622–1631, Apr. 2004.
24. H. Fukuda, K. Yamada, T. Shoji, M. Takahashi, T. Tsuchizawa, T. Watanabe, J. Takahashi, and S. Itabashi, "Four-wave mixing in silicon wire waveguides," *Opt. Express*, vol. 13, no. 12, pp. 4629-4637, Jun. 2005.
25. O. Boyraz, and B. Jalali, "Demonstration of a silicon Raman laser," *Opt. Express,* 12, no. 21, pp. 5269-5273, Oct. 2004.
26. R. L. Espinola, J. I. Dadap, R. M. Osgood, S. J. McNab, and Y. A. Vlasov, "Raman amplification in ultrasmall silicon-on-insulator wire waveguides," *Opt. Express*, 12, no. 6, pp. 3713-3718, Aug. 2004.
27. A. Liu, R. Jones, L. Liao, D. Samara-Rubio, D. Rubin, O. Cohen, R. Nicolaescu, and M. Paniccia, "A high speed silicon optical modulator based on a metal-oxide-semiconductor capacitor," *Nature,* vol. 427, pp. 615-618, Feb. 2004.
28. R. Claps, V. Raghunathan, D. Dimitropoulos, and B. Jalali, "Anti-Stokes Raman conversion in silicon waveguides," *Opt. Express*, 11, no. 22, pp. 2862-2872, Oct. 2003.
29. K. Okamoto, *Fundamental of Optical Waveguides*. New York: Academic Press, 2000.
30. J. H. Jang, W. Zhao, J. W. Bae, D. Selvanathan, S. L. Rommel, I. Adesida, A. Lepore, M. Kwakernaak, and J. H. Abeles,"Direct measurement of nanoscale sidewall roughness of optical waveguides using an atomic force microscope," *Appl. Phys. Lett*., vol. 83, no. 20, pp. 4116 –4118, Nov. 2003.

31. F. Grillot, L. Vivien, S. Laval, D. Pascal, and E. Cassan, "Size influence on the propagation loss induced by sidewall roughness in ultrasmall SOI waveguides," *IEEE Photon. Technol. Lett*., vol. 16, no. 7, pp. 1661–1663, Jul. 2004.
32. G. T. Reed, G. Z. Mashanovich, W. R. Headley, B. Timotijevic, F.Y. Gardes, S. P. Chan, P. Waugh, N. G. Emerson, C. E. Png, M. J. Paniccia, A. Liu, D. Hakd, and V. M. N. Passaroe. "Issues associated with polarization independence in silicon photonics," *IEEE J. on Selected Topics in Quantum Electronics*, vol. 12, no. 6, pp. 1335–1343, Nov./Dec. 2006.
33. K. Yamada, T. Tsuchizawa, T. Watanabe H. Shinojima, H. Nishi, S. Park, Y. Ishikawa, K. Wada, and S. Itabashi, "Silicon photonics based on photonic wire waveguides," *in Proceedings of the 14th Opto Electronics and Communications Conference (OECC '09),* pp. 1–2, Aug. 2009.
34. H. Fukuda, K. Yamada, T. Tsuchizawa, T. Watanabe, H. Shinojima, and S.-I. Itabashi, "Ultrasmall polarization splitter based on silicon wire waveguides," *Opt. Express*, vol. 14, no. 25, pp. 12401–12408, Dec. 2006.
35. G. T. Reed, B. D. Timotijevic, F. Y. Gardes, G. Z. Mashanovich, W. R. Headley, and N. G. Emerson, "Waveguides and devices in silicon photonics: polarisation independence*," in Proceedings of the SPIE, Optoelectronic Integrated Circuits IX*, vol. 6476, pp. (647602-1)–(647602-10), Feb. 2007.
36. J. F. Bauters, M. J. R. Heck, D. Dai, J. S. Barton, D. J. Blumenthal, and J. E. Bowers, "Ultralow-loss planar Si_3N_4 waveguide polarizer," *IEEE Photon. J.*, vol. 5, no. 1, Article ID 6600207, Feb. 2013.
37. M. Huang, "The influence of light propagation direction on the stress-induced polarization dependence of silicon waveguides," *IEEE Photon. Technol. Lett*., vol. 18, no. 12, pp. 1314–1316, Jun. 2006.
38. J. Canning, "Birefringence control in planar waveguides using doped top layers," *Opt Commun.*, vol. 191, no. 3–6, pp. 225–228, May 2001.
39. L. Vivien, F. Grillot, E. Cassan, D. Pascal, S. Lardenois, A. Lupu, S. Laval, M. Heitzmann, and J. Fdli, "Comparison between strip and rib SOI microwaveguides for intra-chip light distribution," *Opt. Mater*. vol. 27, no. 5, pp. 756–762, Feb. 2005.
40. D. Dai, and S. He, "Analysis of the birefringence of a silicon-on-insulator rib waveguide," *Appl. Opt*., vol. 43, no. 5, pp. 1156-1161, Feb. 2004.
41. S. P. Chan, C. E. Png, S. T. Lim, V. M. N. Passaro, and G. T. Reed, "Single mode and polarization independent SOI waveguides with small cross section," *J. Lightw. Technol*., vol. 23, no. 6, pp. 1573–1582, Jun. 2005.
42. G. Z. Mashanovich, M. Milosevic, P. Matavulj, S. Stankovic, B. Timotijevic, P. Y. Yang, E. J. Teo, M. B. H. Breese, A. A. Bettiol, and G. T. Reed, "Silicon photonic waveguides for different wavelength regions," *Semicon. Scien. Technol*., vol. 23, no. 6 pp. 1-12. May 2008.
43. M. M. Milosevic, P. S. Matavulj, B. D. Timotijevic, G. T. Reed, and G. Z. Mashanovich, "Design rules for single-mode and polarization-independent silicon-on-insulator rib waveguides using stress engineering," *J. Lightw. Technol.,* vol. 26, no. 13, pp.1840-1846, Jul. 2008.

44. P. D. Trinh, S. Yegnanarayanan, F. Coppinger and B. Jalali, "Silicon-on-insulator (SOI) phased-array wavelength multi/demultiplexer with extremely low-polarization sensitivity," *IEEE Photon. Technol. Lett*. 9, pp. 940-942, Jul. 1997.
45. W. N. Ye, D.-X. Xu, S. Janz, P. Cheben, M.-Josée Picard, B. Lamontagne, and N. G. T. Tarr, "Birefringence Control using stress engineering in silicon-on-insulator (SOI) Waveguides," *J. Lightw. Technol*. vol. 23, no. 3, pp. 1308-1318, Mar. 2005.
46. D. Dai, Y. Shi, and S. He, "Characteristic analysis of nanosilicon rectangular waveguides for planar light-wave circuits of high integration," *Appl. Opt*. vol. 45, no. 20, pp. 4941-4946, Jul. 2006.
47. Y. Shi, S. Anand, and S. He, Design of a polarization insensitive triplexer using directional couplers based on submicron silicon rib waveguides, *J. Lightw. Technol*. vol. 27, no. 11, pp. 1443-1447, Jun. 2009.
48. Z. Wang, D. Dai, and S. He, "Polarization-insensitive ultrasmall microring resonator design based on optimized Si sandwich nanowires,"*IEEE Photon. Technol. Lett*. vol. 19, no. 20, pp. 1580-1582, Oct. 2007.
49. Y. Shi, S. Anand, and S. He, A Polarization-Insensitive 1310/1550-nm demultiplexer based on sandwiched multimode interference waveguides, *IEEE Photon. Technol. Lett.* vol. 19, no. 22, pp. 1789-1791, Nov. 2007.
50. J. Zhang, H. Zhang, S. Chen, M. Yu, G. Lo, and D. L, Kwong, "A polarization diversity circuits for silicon photonics," OSA/OFC/NFOEC JThA019, 2011.
51. J. Zhang, H. Zhang, S. Chen, M. Yu, G. Q. Lo, and D. L, Kwong, "A tunable polarization diversity silicon photonics filter," *Opt. Express*, vol. 19, no. 14, pp. 13063–13072, Jul. 2011.
52. W. Bogaerts, D. Taillaert, P. Dumon, D. Van Thourhout, R. Baets, and E. Pluk, "A polarization-diversity wavelength duplexer circuit in silicon-on-insulator photonic wires," *Opt. Express*, vol. 15, no. 4, pp. 1567–1578, Feb. 2007.
53. Y. Ding, B. Huang, H. Ou, F. Da Ros, and C. Peucheret, "Polarization diversity DPSK demodulator on the silicon-on-insulator platform with simple fabrication," *Opt. Express*, vol. 21, no. 6, pp. 7828–7834, Mar. 2013.
54. D. Dai, J. Bauters, and J. E. Bowers, "Passive technologies for future large-scale photonic integrated circuits on silicon: polarization handling, light non-reciprocity and loss reduction," *Light: Science & Applications*, vol. 1, no. 3, el, Mar. 2012.
55. B. Troia, F. De Leonardis, M. Lanzafame, T. Muciaccia, G. Grasso, G. Giannoccaro, C. E. Campanella, and V. M. N. Passar, "Design and optimization of polarization splitting and rotating devices in silicon-on-insulator technology," *Advances in OptoElectronics,* vol. 2014. pp. 1-16, Feb. 2014.
56. L. Sansoni, F. Sciarrino,G. Vallone, P. Mataloni, A. Crespi, R. Ramponi, and R. Osellame, "Polarization entangled state measurement on a chip," *Phys. Rev. Lett*. vol. 105, no. 20, pp. 4-5 2, Nov. 2010.
57. D. Dai, Z wang, D. Liang, and J. Bowers, "On-chip polarization handling for silicon photonics," *SPIE* Newsroom, pp. 1-4, Sep. 2012.
58. E. Yamashita and R. Mittra, "Variational method for the analysis of microstrip Lines", *IEEE Trans. Microwave Theory Techniques*, vol. 16, no. 4, pp. 251-256, April 1968.

59. M. M. Ney., "Method of moments as applied to electromagnetic problems," *IEEE Trans. on Microwave Theory Techniques*, vol. 33, no. 10, pp.972-980, Oct. 1985.
60. K. Stamnes, S. C. Tsay, W. Wiscombe, and K. Javaweera, "Numerically stable algorithm for discrete-ordinate-method radiative –transfer in multiple scattering and emitting layered media, " *Appl. Opt.*, vol. 27, no. 12, pp.2502-2509, Jun. 1988.
61. B. M. A. Rahman and J. B. Davies, "Finite-element analysis of optical and microwave waveguide problems," *IEEE Trans. Microwave Theory Techniques*, vol. 32, no.1, pp. 20-28, Jan. 1984.
62. M. Koshiba, "Optical waveguide theory by the finite element method," *KTK Scientific Publishers*," 1992.
63. G. Mur, "Finite difference method for the solution of electromagnetic waveguide discontinuity problem," *IEEE Trans. Microwave Theory Techniques*, vol. MTT-22, pp. 54-57, Jun. 1974.
64. G. R. Hadley, "Transparent boundary-condition for beam propagation," *Opt. Lett*., vol. 16, no. 1, pp. 624-626, May 1991.
65. J. Berenger, "A perfectly matched layer for the absorption of electromagnetic waves," *Journal of Computational Physics* vol. 114, no. 2, pp. 185–200, Oct. 1994.
66. B. Enquist, and A. Majda, "Absorbing boundary-conditions for numerical-simulation of waves," *Applied Mathematical Sciences*, vol. 74, no. 5, pp. 1765-1766, May 1977
67. T. Tamir, "Integrated Optics," Berlin; New York: Spring, 1975.
68. E. A. J. Marcatili, "Dielectric rectangular waveguide and directional couplers for integrated optics," *Bell Syst. Tech. J.*, vol. 48, no.5, pp. 2071-2102, Sep. 1969.
69. A. Kumar, K. Thyagarajan, and A. K. Ghatak, "Analysis of rectangular-core waveguides: An accurate perturbation approach," *Opt. Lett*., vol. 8, no.1, pp. 63-65, Jun. 1983.
70. A. Hardy and W. Streifer, "Coupled mode theory of parallel waveguides," *J. Lightw. Technol*., vol. 3, no. 5, pp. 1135-1146, Oct. 1985.
71. K. S. Chiang.,"Review of numerical and approximate methods for the modal analysis of general optical dielectric waveguides," *Opt. Quantum Electron*. 26(3): pp. S113-S134, 1994.
72. R. M. Knox and P. P. Toulois," Integrated circuits for milimeter through optical wave range," *Proc. MRI symposium submilimeter waves*, 1970.
73. K. S. Chiang, K. M. Lo, and K. S. Kwok, "Effective-index method with built-in perturbation correction for integrated optical waveguide,"*J. Lightw. Technol*. vol. 14, no. 2, pp. 223-228, 1996.
74. K. S. Chiang, "Analysis of optical fibres by the effective-index method." *Appl. Opt*., vol. 25, no. 3, pp. 348-354, Feb. 1986a.
75. K. Van de Velde, H. Thienpont, and R. Van Green, "Extending the effective index method for arbitrarily shaped inhomogeneous optical waveguides," *J. Lightw. Technol*. vol. 6, no. 6, pp.1153-1159, Jun. 1988.
76. K. S. Chiang., "Dual effective-index method for the analysis of rectangular dielectric waveguides." *Appl. Opt.* vol. 25, no. 13, pp. 2169-2174, Jul. 1986b.

77. J. J. G. M. Van Der Tol, and N. H. G. Baken., "Correction to effective index method for rectangular dielectric waveguides," *Electron. Lett*., vol. 24, no. 4, pp.207-208, Feb. 1988.
78. S. Kagami and I. Fukai, "Application of boundary-element method to electromagnetic field problems," *IEEE Trans. Microwave Theory Tech*., vol. 32, no.4, pp.455-461, Apr. 1984.
79. K. Hirayama, and M. Koshiba," Analysis of discontinuities in an open dielectric slab waveguide by combination of finite and boundary elements," *IEEE Trans. Microwave Theory Tech.* vol. MTT-37*,* no. 4, pp. 761-767, Sep. Apr. 1988.
80. J. E. Goell, "A circular-harmonic computer analysis of rectangular dielectric waveguides," *Bell Syst. Tech*., vol. 48, no. 7, pp. 2133-2160, Apr. 1969.
81. A. L. Cullen, O. Ozkan and L. A. Jackson, "Point-matching technique for rectangular-cross-section dielectric rod," *Electron. Lett*. vol. 7, no. 17, pp. 497-499, Aug. 1971.
82. S. T. Peng and A. A. Oliner," Guidance and leakage properties of a class of open dielectric waveguides, part I - mathematical formulations, *" IEEE Trans. Microwave theory Tech*., vol. MTT-29, no. 9, pp. 843-855, Sep. 1981.
83. N. Dagli, and C. G. Fonstad, "Microwave equivalent circuit representation of rectangular dielectric waveguides, *"Appl. Phys. Lett*., vol. 49, no. 6, pp. 308-310, Jun. 1986.
84. M. Koshiba, and M. Suzuki., "Vectorial wave analysis of optical waveguides with rectangular cross-section using equivalent network approach, *"J. Lightw. Technol*., vol. 21, no. 22, pp.1026-1028, Oct. 1985.
85. M. Koshiba and M. Suzuki., "Vectorial wave Analysis of dielectric waveguides for optical-integrated circuits using equivalent network approach, *"J. Lightw. Technol*., vol .4, no.6, pp. 656-664, Jun. 1986b.
86. P. C. Kendall, P. W. A. Mcllroy, and M. S. Stern, "Spectral index method for rib waveguide analysis, *" Electron. Lett.,* vol. 25, no. 2, pp. 107 – 108, Jan. 1989.
87. M.S. Stern, P.C. Kendall and P.W.A. Mcllroy, "Analysis of the spectral index method for vector modes of rib waveguides, *" IEE Proc. Pt. J*., vol. 137, no. 1, pp. 21 – 26, Feb. 1990.
88. V. S. Burke, "Spectral index method applied to coupled rib waveguides, *" Electron. Lett.,* vol. 25, no. 6, pp. 605-606, Apr. 1989.
89. V. S. Burke, "Spectral index method applied to two nonidentical closely separated rib waveguides, *" IEE Proc. Pt. J*., vol. 137, no. 5, pp.289-292, Oct. 1990.
90. V. S. Burke., "Planar waveguide analysis by the spectral index method: II. Multiple layers optical gain and loss," *Opt. Quantum Electron*., vol. 26, no. 2, pp. 63–77, Feb. 1994.
91. J. R. P. Pola, W. Biehlig, and F. Lederer., "A Generalization of the Spectral Index method toward multiple rib waveguides," *J. Lightw.Technol*, vol. 14, no. 3, pp. 454–461, Mar. 1996.
92. M.D, Feit, and J. A. Fleck, "Computation of mode eigenfunctions in graded-index optical fibres by the propagation beam method," *Appl. Opt*., vol. 19, no. 13, pp. 2240-2246, Jul. 1980.

93. Y. Chung, N. Dagli, and, L. Thylen,"Explicit finite difference vectorial beam propagation method," *Electron. Lett*., vol. 27, no. 23, pp. 2119-2121, Nov. 1991.
94. W.P. Huang, C.L. Xu, and S.K. Chaudhuri, "A finite-difference vector beam propagation method for three-dimensional waveguide structures,"*IEEE Photon. Technol. Lett.,* vol. 4, no. 2, pp. 148-151, 1992.
95. W.P. Huang, and, C.L. Xu, "A wide-angle vector beam propagation method," *IEEE Photon. Technol. Lett*., vol. 4, no. 10, pp. 118-1120, Oct. 1992.
96. Y. Tsuji and M. Koshiba, "A finite element beam propagation method for strongly guiding and longitudinally varying optical waveguides," *J. Lightw. Technol*., vol. 14, no. 2, pp. 217–222, Feb. 1996.
97. S. S. A. Obayya, B. M. A. Rahman, and H. A. El-Mikati, "New full vectorial numerically efficient propagation algorithm based on the finite element method," *J. Lightw. Technol*., vol. 18, no. 3, pp. 409–415, Mar. 2000.
98. H. Rao, R. Scarmozzino, and R. M. Osgood., "A bidirectional beam propagation method for multiple dielectric interfaces", *IEEE Photon. Technol. Lett.*, vol. 11, no. 7, pp. 830-832, Jul. 1999.
99. Y. Tsuji, and M. Koshiba., "Guided-mode and leaky-mode analysis by imaginary distance beam propagation method based on finite element scheme,"*J. Lightw. Technol.*, vol. 18, no. 4, pp. 618-623, Apr. 2000.
100. S. S. A. Obayya, B. M. A. Rahman, K. T. V. Grattan, and H. El-Mikati, "Full-vectorial finite-element-based imaginary distance beam propagation solution of complex modes in optical waveguides," *J. Lightw. Technol.*, vol. 20, no. 6, pp.1054-1060, Jun. 2002.
101. J. B. Davies, and C. A. Muilwyk, "Numerical solution of uniform hollow waveguides with boundary of arbitrary shape," *Proc. IEEE*, vol. 113, no. 2, pp. 277-284, Feb. 1966.
102. K. Bierwirth, N. Schulz, and F. Arndt, "Finite-difference analysis of rectangular dielectric waveguide structures," *IEEE Trans. Microwave Theory Tech*. vol. 34, no. 11, pp. 1104-1113, Nov. 1986.
103. B. M. A. Rahman and J. B. Davies, "Finite-element analysis of optical and microwave waveguide problems," *IEEE Trans. Microwave Theory Tech*. vol. 32, no. 1, pp. 20-28, Jan. 1984.
104. M. Koshiba, and K. Inoue, "Simple and efficient finite-element analysis of microwave and optical waveguides," *IEEE Trans. Microwave Theory Tech*. vol. 40, no. 2, pp. 371–377, Feb. 1992.
105. B. M. A. Rahman, and J. B. Davies, "Finite element solution of integrated optical waveguides," *J. Lightw. Technol*., vol. 2, no. 5, pp. 682–688, Oct. 1984.
106. B. M. A. Rahman, and J. B. Davies, "Penalty function improvement of waveguide solution by finite elements," *IEEE Trans. Microwave Theory Tech*., vol. 32**,** no, 8, pp. 922-928, Aug. 1984.
107. A. Bossavit, and I. Mayergozy., "Edge-elements for scattering problems," *IEEE Trans.,* vol. 25, no. 4, pp. 2816-2821, Jul.1989.
108. J. B. Davies, "The finite element method in numerical techniques for microwave and millimetre-wave passive structures," Edited by T. Itoh, *NY, Wiley*, pp. 33-132, 1989.
109. L. Cairo., "Variational techniques in electromagnetism, London: Blackie, 1965.

110. A. B. Finlayson, "Method of weighted residuals and variational principles," New York: *Academic Press*, 1972.
111. N. Mabaya, P. E. Lagasse, and P. Vandenbuleke, "Finite element analysis of optical waveguides," *IEEE Trans. Microwave Theory Tech*. vol. 20, no. 6, pp. 600–609, 1981.
112. A. B. Finlayson, "Method of weighted residual and variational methods," New York: *Academic Press*, 1972.
113. P. Daly, "Finite-element approach to propagation in elliptical and parabolic waveguide," *International Journal for Numerical Methods in Engineering*, vol. 20, no. 4, pp.681-688, Apr. 1984.
114. R. Wu, and C. H. Chen, "A scalar variational conformal mapping technique for weakly guiding dielectric waveguides," *IEEE J. Quantum Electron*., vol. QE. 22, no. 5, pp. 603–609, May 1986.
115. M. Koshiba, K. Hayata, and M. Suzuki, "Approximate scalar finite-element analysis of anisotropic optical waveguides with off-diagonal elements in a permittivity tensor," *IEEE Trans. Microwave Theory Tech*., vol. 32, no. 6, pp. 587–593, Sept. Jun. 1984.
116. N. Mabaya, P.E. Lagasse and P. Vandenbulcke, "Finite element analysis of optical waveguides," *IEEE* Trans. *Microwave Theory Tech*., Vol. MTT-29, no. 6, pp. 600-605, Jun. 1981.
117. W. J. English, "An ***E*** vector variational formulation of the maxwell equations for cylindrical waveguide problems," *IEEE Trans. Microwave Theory Tech*., vol. 19, no. 1, pp.40-46, Jan. 1971.
118. M. Koshiba, and K. Hayata, and M. Suzuki, "Improved finite-element formulation in terms of the magnetic field vector for dielectric waveguides," *IEEE Trans. On Microwave Theory and Tech.* vol. 33, no. 3, pp. 227-233, Mar. 1985.
119. J. A. M Svedin, "A numerically efficient finite-element formulation for the general waveguide problem with spurious modes," *IEEE Trans. On Microwave Theory and Tech.* vol. 37*,* no. 11, pp. 1708-1715, Nov. 1989.
120. A. Konrad, "Vector variational formulation of electromagnetic fields in anisotropic media," *IEEE Trans. Microwave. Theory Tech*., vol. 24, no.9, pp. 553- 559, Sep. 1976.
121. A. Yarvin, "Coupled mode theory for guided-wave optics," *IEEE J. Quantum Electron.,* vol. 9, no. 9, pp. 919-933, Sep. 1973.
122. A. Hardy, and W. Streifer, "Coupled mode solutions for multi-waveguide systems," *IEEE J. Quantum Electron*., vol. 22, no. 4, pp.528-534, Apr. 1986.
123. L. B. Soldano, and E. C. M. Pennings, "Optical multi-mode interference devices based on self-imaging: principles and applications," *J. Lightw. Technol*. vol. 13, no. 4, pp.615–627, Apr. 1995.
124. J. L. Liu, Y. Shi, F. Wang, Y. Lu, S.L. Gu, R. Zhang, and Y. D. Zheng, "Study of dry oxidation of triangle-shaped silicon nanostructure," *Appl. Phys. Lett.*, vol. 69, no. 6, pp. 1761-1763, Sep. 1996.
125. M. Lipson, "Guiding, modulating, and emitting light on silicon challenges and opportunities," *J. Lightw. Technol.*, vol. 23, no. 12, pp. 4222 – 4238, Dec. 2005.
126. B. G. Lee, X. Chen, A. Biberman, X. Liu, I-W. Hsieh; C-Y. Chou, J. I. Dadap, F. Xia, W. M. J. Green, L. Sekaric, Y. A. Vlasov, R. M. Osgood, and K. Bergman, "Ultrahigh-

bandwidth silicon photonic nanowire waveguides for on-chip networks," *IEEE Photon. Technol., Lett.*, vol. 20, pp. 398-400, Mar. 2008.

127. A. V. Yurii, M. O'Boyle, F. H. Hendrik and J. McNab Sharee, "Active control of slow light on a chip with photonic crystal waveguides," *Nature*, pp. 438 65-69, Sep. 2005.
128. F. L. Kein, V. I. Balykin, and K. Hakuta, "Atom trap and waveguide using a two-color evanescent light field around a subwavelength-diameter optical fibre," Phys. Rev. A 70, 063403, Dec. 2004.
129. J. Y. Lou, L. M. Tong, and Z. Z. Ye, "Modelling of silica nanowires for optical sensing," *Opt. Express*, vol. 13, no. 6, pp. 2135-2140, Mar. 2005.
130. C. Turner, C. Manolatou, B. S. Schmidt, M. Lipson, M. A. Foster, J. E. Sharping, and A. L. Gaeta, "Tailored anomalous group-velocity dispersion in silicon channel waveguides," *Opt. Express*, vol. 14, no. 10, pp. 4357–4362, May 2006.
131. ISO 11146, Laser and laser related equipment – Test methods for laser beam widths, divergence and beam propagation ratios, *International Organization for Standardization*, Geneva, Switzerland, 2005.
132. M. Lipson, "Silicon photonics: An exercise in self control," *Nat. Photonics,* vol. 1, pp. 18-19, Jan. 2007.
133. R. Soref, "The past, present, and future of silicon photonics*," IEEE J. Sel. Top. Quantom Electron.,* vol. 12, no. 6, pp. 1678-1687, Nov. 2006.
134. T. Barwicz, M. A. Popovic, M. R. Watts, P. T. Rakich, C. W. Holzwarth, F. X. Kaertner, E. P. Ippen, and H. I. Smith, "Strategies for successful realization of strong confinement microphotonic devices," *Invited*, SPIE Proc. vol. 6898, no. 68980, Dec. 2008.
135. J. Wang, B. Niu, Z. Sheng, A. Wu, W. Li, X, Wang, S. Zou, M. Qi, and F. Gan, "Novel ultra-broadband polarization splitter-rotator based on mode-evolution tapers and a mode-sorting asymmetric Y-junction," *Opt. Express*, vol. 22, no. 11, pp. 13565-13571, Jun. 2014.
136. V. P. Tzolov, and M. Fontaine, "A passive polarization converter free of longitudinally periodic structure," *Opt. Commun*., vol. 127. no. pp. 7-13, Jun. 1996.
137. W. Bogaerts, D. Taillaert, P. Dumon, D. Van Thourhout, R. Baets, and E. Pluk, "A polarization-diversity wavelength duplexer circuit in silicon-on-insulator photonic wires," *Opt. Express,* vol. 15, no. 4, pp. 1567–1578, Feb. 2007.
138. H. Guan, A. Novack, M. Streshinsky, R. Shi, Q. Fang, A. E. Lim, G. Q. Lo, T. Baehr-Jones, and M. Hochberg, "CMOS-compatible highly efficient polarization splitter and rotator based on a double-etched directional coupler," *Opt. Express*, vol. 22, no. 3, pp. 2489–2496, Jan. 2014.
139. R. C. Alferness and L. L. Buhl, "High-speed waveguide electro-optic polarization modulator r," *Opt. Lett*., vol.7, no.10, pp. 500–502, Oct. 1982.
140. M. Schlak, C. M. Weinert, P. Albrecht, and H. P. Nolting, "Tuneable TE/TM-mode converter on (001)-InP-substrate, " *IEEE Photon. Technol. Lett*., vol. 3, no.1, pp. 15–16, Jan. 1991.
141. K. Mertens, B. Scholl, and H. J. Schmitt, "Strong polarization conversion in periodically loaded strip waveguides," *IEEE Photon. Technol. Lett*., vol. 10, no. 8, pp. 1133–1135, Aug. 1998.

142. Y. Shani, R. Alferness, T. Koch, U. Koren, B. I. Miller, and M. G. Young, "Polarization rotation in asymmetric periodic loaded rib waveguides," *Appl. Phys. Lett*., vol. 59, no. 11, pp. 1278-1280, Sep. 1991.
143. S. S. A. Obayya, B. M. A. Rahman, K. T. V. Grattan and H. A. El-Mikati, "Analysis of polarization rotation in cascaded optical waveguide bends," *IEE Proc.-Optoelectron.* Vol. 149, no. 2, pp. 75-80, Apr. 2002.
144. B. E. Little and S. T. Chu, "Theory of polarization rotation and conversion in vertically coupled microresonators," *IEEE Photon Technol. Lett*., vol. 12, no. 4. pp. 401–403, Apr. 2000.
145. H. Deng, D. O. Yevick, C. Brooks, and P. E. Jessop, "Design rules for slanted-angle polarization rotators," *J. Lightw. Technol*., vol. 23, no. 1. pp. 432–445, Jan. 2005.
146. B. M. A. Rahman, S. S. A. Obayya, N. Somasiri, M. Rajarajan, K. T. V. Grattan, and H. A. El-Mikathi, " Design and characterization of compact single-section passive polarization rotator," *J. Lightw. Technol*., vol. 19, no.4, pp. 512–519, Apr. 2001.
147. C. Brooks, P. E. Jessop, H. Deng, D. O. Yevick, and G. Tarr, " Passive silicon-on-insulator polarization-rotating waveguides," *Opt. Eng*., vol. 45, no. 4, pp. (044603-1)-(044603-5), Apr. 2006.
148. D. M. H. Leung, B. M. A. Rahman, and K. T. V. Grattan, "Numerical analysis of asymmetric silicon nanowire waveguide as compact polarization rotator," *IEEE Photon. J*., vol. 3, no. 3, pp. 381-389, Apr. 2011.
149. C. Van Dam, L. H. Spiekman, F. P. G. M. van Ham, F. H. Groen, J. J. G. M. van der Tol, I. Moerman, W. W. Pascher, M. Hamacher, H. Heidrich, C. M. Weinert, and M. K. Smit, "Novel compact polarization converters based on ultra short bends," *IEEE Photon. Technol. Lett*., vol. 8, no. 10, Oct. 1996.
150. T. Cao, S. Chen, Y. Fei, L. Zhang, and Q. Xu," Ultra-compact and fabrication-tolerant polarization rotator on a bend asymmetric- slab waveguide," *Appl. Opt*., vol. 52, no. 5, pp. 990-996, Feb. 2013.
151. J. Z. Huang, R. Scarmozzino, G. Nagy, M.J. Steel, R.M. Osgood, "Realization of a compact and single-mode optical passive polarization converter," *IEEE Photon. Technol. Lett*., vol. 12, no. 3, pp. 317-319, Mar. 2000.
152. D. O. Dzibrou, J. J. G. M. van der Tol, and M. K. Smi, " Tolerant polarization converter for InGaAsP-InP photonic integrated circuits," *Opt. Lett*., vol. 38, no. 18, pp. 3482-3484, Sep. 2013.
153. M. R. Watts, and H.A. Haus, "Integrated mode-evolution-based polarization rotators," *Opt. Lett*., vol. 30, no. 2, pp. 138-140, Jan. 2005.
154. Y. Xiong, D.-X Xu, J. H. Schmid, P. Cheben, S. Janz, and W. N. Ye, "Robust silicon waveguide polarization rotator with an amorphous silicon overlayer," *IEEE Photon. J*., vol.6, no. 2, Apr. 2014.
155. Z. Wang, and D. Dai, "Ultrasmall Si-nanowire-based polarization rotator," *J. Opt. Soc. Am. B: Opt. Phys*., vol. 25, no. 5, pp. 747-753, May 2008.
156. C. Alonso-Ramos, S. Romero-García, A. Ortega-Moñux, I. Molina-Fernández, R. Zhang, H.G. Bach, and M. Schell, "Polarization rotator for InP rib waveguide," *Opt. Lett*., vol. 37, no. 3, pp. 335-337, Feb. 2012.

157. D. Vermeulen, S. Selvaraja, P. Verheyen, P. Absil, W. Bogaerts, D. V. Thourhout, and G. Roelkens, " Silicon-on-insulator polarization rotator based on a symmetry breaking silicon overlay," *IEEE Photon. Technol. Lett*., vol. 24, no. 6, pp. 482-484 Mar. 2012.
158. G. Chen, L. Chen, W. Ding, F. Sun, and R. Feng, " Ultrashort slot polarization rotator with double paralleled nonlinear geometry slot crossing," *Opt. Lett*., vol. 38, no. 11, pp. 1984-1986, Jun. 2013.
159. G. Chen, L. Chen, W. Ding, F. Sun, and R. Feng, "Ultra-short silicon-on-insulator (SOI) polarization rotator between a slot and a strip waveguide based on a nonlinear raised cosine flat-tip taper," *Opt. Express,* vol. 21, no. 12, pp. 14888-14894, Jun. 2013.
160. B. M. Holmes, and D. C. Hutchings, "Realization of novel low-loss monolithically integrated passive waveguide mode converters," *IEEE Photonics Technol. Lett*., vol. 18, no. 1, pp. 43-45, Jan. 2006.
161. S. Kim, R. Takei, Y. Shoji, and T. Mizumoto, "Single-trench waveguide TE-TM mode converter," *Opt. Expres,* vol. 17, no. 14, pp. 11267-11273. Jul. 2009.
162. K. Nakayama, Y. Shoji, and T. Mizumoto, "Single trench SiON waveguide TE-TM mode converter," *IEEE Photonics Technol. Lett*., vol. 24, no. 15, pp. 1310-1312, Aug. 2012.
163. A. V. Velasco, M. L. Calvo, P. Cheben, A. Ortega-Moñux, J. H. Schmid, C. A. Ramos, M. FernandezÍ, J. Lapointe, M. Vachon, S. Janz, and D. -X. Xu, " Ultracompact polarization converter with a dual subwavelength trench built in a silicon-on-insulator waveguide," *Opt. Lett*., vol. 37, no. 3, pp. 365-367, Feb. 2012.
164. J. Pello, J. van der Tol, S. Keyvaninia, R. van Veldhoven, H. Ambrosius, G. Roelkens, and M. Smit, "High-efficiency ultrasmall polarization converter in InP membrane," *Opt. Lett*., vol. 37, no. 17, pp. 3711-3713, Sep. 2012.
165. L. Chen, C.R. Doerr, and Y. Chen, "Compact polarization rotator on silicon for polarization-diversified circuits," *Opt. Lett*., vol. 36, no. 4, pp. 469-471, Feb. 2012.
166. H. Zhang, S. Das, Y. Huang, C. Li, S. Chen, H. Zhou, M. Yu, P. G. Lo, and J. T. L. Thong, "Efficient and broadband rotator using horizontal slot waveguide for silicon photonic," *Appl. Phys. Lett*., vol. 101, no. 2, pp. (021105-1)-(021105-4), Jul. 2012.
167. J. Fan, C. Huang, and L. Zhu, "A compact, broadband slot waveguide polarization rotator," *AIP Adv.* **1**, vol.1, no. 4, pp. (042136-1)-(042136-2), Nov. 2011.
168. D. Dai, and Y. Tang, and J. E. Bowers, "Mode conversion in tapered submicron silicon ridge optical waveguides," *Opt. Express*, vol. 20, no. 12, pp. 13425-13439, Jun. 2012.
169. D. Dai, and J.E. Bowers , "Novel concept for ultracompact polarization splitter-rotator based on silicon nanowires," *Opt. Express*, vol. 19, no. 11, pp. 10940-10949, May 2011.
170. Y. Ding, H. Ou, and C. Peucheret, "Wideband polarization splitter and rotator with large fabrication tolerance and simple fabrication process," *Opt. Lett*., vol. 38, no. 8, pp. 1227-1229, Apr. 2013.
171. V. R. Almeida, Q. Xu, C. A. Barrios, R. R. Panepucci, and M. Lipson, "Guiding and confining light in void nanostructure," *Opt. Lett*., vol. 29, no. 11, pp. 1209-1211, Jun. 2004.
172. Q. Xu, V. R. Almeida, R. R. Panepicci, and M. Lipson, "Experimental demonstration of guiding and confining light in nanometer-size low refractive-index material," *Opt. Lett*., vol. 29, no. 14, pp. 1626-1628, Jul. 2004.

173. N. N. Feng, J. Michel and L. C. Kimerling, "Optical Field Concentration in Low Index Waveguides," *IEEE J. Quantum Electron*., vol. 42, no. 9. pp. 885 – 890, Sep. 2006.
174. N. N. Feng, R. Sun, J. Michel, and L. C. Kimerling, "Low-loss compact-size slotted waveguide polarization rotator and transformer," *Opt. Lett*., vol. 32, no. 15, pp. 2131-2133, Aug. 2007.
175. B. Wohlfeil, L. Zimmermann, and K. Petermann, "Asymmetric codirectional coupler between regular nanowaveguide and slot-waveguide for polarization conversion," *OSA Adv. Photon. Congress*, ITu2B5, 2012.
176. Y. Fei, L. Zhang, Y. Cao, X. Lei, and S. Chen, "A novel polarization rotator based on an asymmetric slot waveguide," *Opt. Commun*., vol. 324, pp. 22-25, Aug. 2014.
177. A. Bahr, B. M. A. Rahman, R. K. Varshney, and B. P. Pal, "Design and performance study of a compact SOI polarization rotator at 1.55 μm," *J. Lightw. Technol*. vol. 31, no. 23, pp. 3687-3693, Dec. 2013.
178. M. Komatsu, K. Saitoh, and M. Koshiba, "Design of miniaturized silicon wire and slot waveguide polarization splitter based on a resonant tunnelling." *Opt. Express,* vol. 17, no.21, pp. 19225-19234, Oct. 2009.
179. X. Zhi-Gang, L. Zhi-Yuan, and Z. Dao-Zhong, "TM-like and TE-like modes coupling in a two dimensional photonic crystal slab composed of truncated cone silicon rods," *Chin. Phys. Lett*., vol. 25, no. 6, pp. 2089-2092, Jun. 2008.
180. T. Baba "Si photonic wire waveguides" *Proc. SPIE*, vol. 5515, pp. 150-157 Oct. 2004.
181. A. A. Obayya, B. M. A. Rahman, K. T. V. Grattan, and H. A. El-Mikati, "Improved design of a polarization converter based on semiconductor optical waveguides bends," *Appl. Optics*, vol. 40, no, 30, pp. 5395-5401,Oct. 2001.
182. B. M. A. Rahman, and J. B. Davies, "Finite element solution of integrated optical waveguides," *J. Lightw. Technol*., vol. 2, no. 5, pp. 682–688, Oct. 1984.
183. S. S. A. Obayya, B. M. A. Rahman, and H. A. El-Mikati, "New full vectorial numerically efficient propagation algorithm based on the finite element method," *J. Lightw. Technol*., vol. 18, no. 3, pp. 409–415, Mar. 2000.
184. B. M. A. Rahman and J. B. Davies, "Analysis of optical waveguide discontinuities," *J. Lightw. Technol*., vol. 6, no. 1, pp. 52–57, Jan. 1988.
185. B. Glance, "Polarization independent coherent optical receivers," *J. Lightw. Technol*., vol. 5, no. 2, pp. 274–276, Feb. 1987.
186. Y. Han, and G. Li, "Coherent optical communication using polarization multiple-input-multiple-output," *Opt. express*, vol. 13, no. 19, pp. 7527-7534, Sep. 2005.
187. H. Nishihara, M. Haruna, and T. Suhara, "Electro-optics, Handbook," Chapter. 26.
188. Q. Wang, and J. Yao, "A high speed 2×2 electro-optics switch using a polarization modulator," *Opt. Express*, vol. 15, no. 25, pp. 16500-16505, Dec. 2007.
189. J. Wang, C. Lee, B. Niu, H. Huang, Y. Li, M. Li, X. Chen, Z. Sheng, A. Wu, W. Li, X. Wang, S. Zou, F. Gan, and M. Qi, " A silicon-on-insulator polarization diversity scheme in the mid-infrared," *Opt. express*, vol. 23, no. 11, pp. 15029-15037, Jun. 2015.
190. I. Kiyat, A. Aydinli, and N. Dagli, "A compact silicon-on-insulator polarization splitter," *IEEE Photon. Technol*. *Lett.*, vol. 17, no. 1, pp. 100–102, Jan. 2005.
191. S. Soudi and B. M. A. Rahman, "Design of compact polarization rotator using simple silicon nanowires," *Appl. optics*, vol. 53, no. 34, pp. 8071-8077, Dec. 2014.

192. D. Dai, L. Liu, S. Gao, D. Xu, and S. He, "Polarization management for silicon photonic integrated circuits," Laser Photon. Rev., vol. 7, no. 3, pp. 303-328, may 2013.
193. B. Troia, F. D. Leonardis, M. Lanzafame, T. Muciaccia, G. Grasso, G. Giannoccaro,C. E. Campanella, and V. M. N. Passaro, "Design and optimization of polarization splitting and rotating devices in silicon-on-insulator technology," *Advance. OptoElectro*., vol. 2014, pp. 1-16, Feb. 2014.
194. K. Okamoto, M. Doi, T. Irita, Y. Nakano, and K. Tada, "Fabrication of TE/TM mode splitter using completely buried GaAs/GaAlAs waveguide," *Jpn. J. Appl. Phys*., vol. 34, no. 1, pp. 114–115, 1990.
195. Y. -P. Liao, R. -C. Lu, C. -H. Yang, and W. -S. Wang, "Passive Ni: $LiNbO_3$ polarization splitter at 1.3 μm wavelegth," *Electron. Lett*., vol. 32, no. 11, pp. 1003–1005, May 1996.
196. M. Masuda, and G. L. Yip, "An optical TE-TM mode splitter using a $LiNbO_3$ branching waveguide*," Appl. Phys. Lett*., vol. 37, no.1, pp. 20-22, Jul. 1980.
197. A. N. Miliou, R. Srivastava, and R. V. Ramaswamy, "A 1.3-μm directional directional coupler polarization splitter by ion exchange,"*J. Lightw. Technol*., vol. 11, no. 2, pp. 220–225, Feb. 1993.
198. L. M. Augustin, R. Hanfoug, J. J. G. M. van der Tol, W. J. M. de Laat, and M. K. Smit, " A Compact Integrated Polarization Splitter/Converter in InGaAsP-InP,"*IEEE Photon. Technol. Lett*., 19, 1286 (2007).
199. L. B. Soldano, A. H. de Vreede, M. K. Smit, B. H. Verbeek, E. G. Metaal, and F. H. Groen, "Mach-Zehnder Interferometer polarization splitter in InGaAsP/InP," *IEEE Photon. Technol. Lett*., vol. 6, no. 3, pp. 402-405, Mar. 1994.
200. M. Rajarajan, and B. M. A. Rahman, and K. T. V. Grattan, "A novel and compact optical polarizer incorporating a layered waveguide core structure," *J. Lightw. Technol*., vol. 21, no. 12, pp. 3463–3470, Dec. 2003
201. P. Wei and W. Wan, "A TE-TM mode splitter on lithium niobate using Ti, Ni, and MgO diffusions,"*IEEE Photon. Technol. Lett*., vol. 6, no. 2, pp. 245-248, Feb. 1994.
202. F. Ghirardi, J. Brandon, M. Carre, A. Bruno, L. Menigaux, and A. Carenco, "Polarization splitter based on modal birefringence in InP/InGaAsP optical waveguides,"*IEEE Photon. Technol. Lett*., vol. 5, no. 9, pp. 1047-1049, Sep. 1993.
203. P. Albrecht, M. Hamacher, H. Heidrich, D. Hoffman, H. P. Nolting, and C. M. Weinert, "TE/TM mode splitters on InGaAsP/Inp," *IEEE Photon. Technol*, *lett.,* vol. 2, no. 2, pp. 114-115, Feb. 1990.
204. M. Rajarajan, C. Themistos, B. M. A. Rahman, and K. T. V. Gratan"Characterization of metal-clad TE/TM mode splitters using the finite element method," *J. Lightw. Technol*., vol. 15, no. 12, pp. 2264-2269 Dec. 1997.
205. T. Yamazaki, H. Aono, J. Yamauchi, and H. Nakano, "Coupled waveguide polarization splitter with slightly different core widths," *J. Lightw. Technol*., vol. 26, no. 21, pp. 3528–3533, Nov. 2008.
206. B. M. A. Rahman, N. Somasiri, C. Themistos, and K. T. V. Grattan, "Design of optical polarization splitter in a single-section deeply etched MMI waveguides," *Appl. Phys. Lett.* vol. 73, no. 5, pp. 613-618, Oct. 2001.

207. J. M. Hong, H. H. Ryu, S. R. Park, J. W. Jeong, S. G. Lee, E. Lee, S. Park, D. Woo, S. Kim, and O. Beom-Hoan, "Design and fabrication of a significantly shortened multimode interference coupler for polarization splitter application," *IEEE Photon. Technol. Lett*., vol. 15, no. 1, pp. 72-74, Jan. 2003.
208. B. K. Yang, S. Y. Shin, and D. Zhang, "Ultrashort polarization splitter using two-mode interference in silicon photonic wires," *IEEE Photon. Technol. Lett*., vol. 21, no. 7, pp. 432-434, Apr. 2009.
209. T. K. Liang and H. K. Tsang., "Integrated polarization beam splitter in high index contrast silicon-on-insulator waveguides," *IEEE Photon. Technol. Lett*., vol. 17, no. 2, pp. 393-395, Feb. 2005.
210. L. M. Augustin, R. Hanfoug, J. J. G. M. van der Tol, W. J. M. de Laat, and and M. K. Smit," A compact integrated polarization splitter/converter in InGaAsP-InP," *IEEE Photon. Technol. Lett*. Lett. vol. 19, no. 17, pp. 1286-1288, Sep. 2007.
211. D. Dai, Y. Shi, and S. He, "Characteristic analysis of nanosilicon rectangular waveguide for planar light-wave circuits of high integration," *Appl. Opt.* vol. 45, no. 20, pp. 4941-4946, Jul. 2006.
212. V. R. Almeida, Q. Xu, C. A. Barrios, and M. Lipson," Guiding and confining light in void nanostructure," *Opt. Lett.*, vol. 29, no. 11, pp. 1209-1211, Jun. 2004.
213. Y. Fei, S. Chen, L. Zhang, and T. Cao, "Design and analysis of polarization splitter based on a horizontal slotted waveguide," *Opt. Eng*., vol. 51, no. 5, pp. (054601-1)-(054601-4), May 2012.
214. J. Xiao, X. Liu, and X. Sun, " Design of a compact polarization splitter in horizontal multiple-slotted structure*," Jpn. J. Appl. Phys.,* vol. 47, no. 5, pp. 3748–3754, May 2008.
215. S. Lin, J. Hu, and K. B. Crozier, "Ultracompact, broadband slot waveguide polarization splitter," *Appl.Phys. Lett.,* vol. 98, no. 15, pp. 151101-151103, Apr. 2011.
216. D. Dai, Z. Wang, and J. E. Bowers, "Ultrashort broadband polarization beam splitter based on an asymmetrical directional coupler," *Opt. Lett*., vol. 36, no. 13, pp. 2590-2592, Jul. 2011.
217. B. Shen, P. Weng, R. Polson, and R. Menon, "An integrated-nanophotonics polarization beamsplitter with 2.4*2.4 μm2 footprint," *Nat. Photon.,* vol. 9, pp. 378-3852, May 2015.
218. J. Chee, S. Zhu, and GQ. Lo, "CMOS compatible polarization splitter using hybrid plasmonic waveguide," *Opt. Epress,* vol. 20, no. 23, pp. 25345–25355, Oct. 2012.
219. F. Lou, Z. Wang, W. Zhechao, D. Dai, L. Thylen, and W. Lech, "Experimental demonstration of ultra-compact directional couplers based on silicon hybrid plasmonic waveguides," *Appl. Phys. Lett.,* vol. 100, no. 24, pp. 241105-241108, Jun. 2012.
220. C.-L. Zou, F.-W. Sun, C.-H. Dong, X.-F. Ren, J.-M. Cui, X.-D. Chen, Z.-F. Han, and G.-C. Guo, "Broadband integrated polarization beam splitter with surface plasmon.,"*Opt. Lett*., vol. 36, No. 18, pp. 3630-3632, Sep. 2011.
221. T. Qilong, H. Xuguang, Z. Wen and Y. Kun, "A plasmonic based ultracompact polarization beam splitter on silicon-on-insulator waveguides," *Appl. phys.*, pp. 1-5, Jul. 2013.

222. C. Van Dam, L. H. Spiekman, F. P. G. M. Van Ham, F. H. Groen, J. J. G. M. Van der Tol, I. Moerman, W. W. Pascher, M. Hamacher, H. Heidrich, C. M. Weinert, and M. K. Smit, "Novel compact polarization converters based on ultra short bends," *IEEE Photon. Technol.,* vol. 8, no. 10, pp. 1346-1348, Oct. 1996.
223. Y. Shi, D. Dai, and S. He, "Proposal for an ultracompact polarization-beam splitter based on a photonic-crystal-assisted multimode interference coupler," *IEEE Photon. Technol. Lett.,* vol. 19, no. 11, pp. 825-827, Jun. 2007.
224. X. Ao, L. Liu, L. Wosinski, and S. He, "Polarization beam splitter based on a two-dimesional photonic crystal of pillar type," *Appl. Phys. Lett*., vol. 89, no.17, p. 171115 Oct. 2006.
225. J. Feng and Z. Zhou, "polarization beam splitter using a binary blazed grating coupler, *opt. Lett*., vol. 32, no. 12, pp. 1662-1664, Jun. 2007.
226. S. S. A. Obayya, B. M. A. Rahman, and H. A. El-Mikati, "New full- vectrorial numerically efficient propagation algorithm based on the finite element method," *J. Lightw. Technol.,* vol. 18, no. 3, pp. 409-415, Mar. 2000.